FERROUS METALLURGY
MONTANUNIVERSITAET

The influence of manganese on the initial solidification of near-peritectic steel

Master's Thesis

by

Christian Legerer, BSc.

handed in at the Montanuniversität Leoben/Chair of Ferrous Metallurgy
for attaining the degree of

Master of Science

In the field of study Metallurgy

MONTAN
UNIVERSITÄT
Chair of Ferrous Metallurgy – Montanuniversität Leoben
Franz-Josef-Straße 18 – 8700 Leoben, Österreich

Abstract

In continuous casting, it's long been understood that peritectic steels are prone to casting defects. There is plenty of evidence that alloying elements such as manganese play a pivotal role in the quality of continuously cast products. However, there is still no general understanding of the fundamental mechanisms underpinning the role of manganese for the peritectic phase transition. The literature describes several approaches that investigate the behaviour of peritectic multi-component alloys, but all of these involve strong interdependencies between alloying elements, and thus do not explain the effect of individual alloy components. The aim of this thesis was to gain further insight on the specific influence of manganese on the δ-ferrite to γ-austenite phase transformation. This was achieved using a combination of high-temperature laser-scanning confocal-microscopy (HTLSCM) and dipping experiments. A series of experiments on alloys containing 0-6 wt.-% manganese were performed utilizing both experimental techniques. Although the HTLSCM experiments did not show a particular effect of manganese on the "massive transformation", the previous research findings that the primary solidified δ-ferrite and the associated undercooling determine the "massive transformation", could be supported. Both HTLSCM and dipping results confirmed that the position relative to the peritectic point is of great importance for the solidification behaviour of peritectic steels. However, the results of the presented dipping setup for steels containing more than 1 wt.-% manganese deviate from this statement and indicate other influencing factors for higher alloyed steels.

Kurzfassung

Beim Stranggießen sind peritektische Stähle bekannt für das vermehrte Auftreten von Gussfehlern. Vieles deutet darauf hin, dass das Legierungselement Mangan einen zentralen Einfluss auf den Erstarrungsprozess kontinuierlich vergossener Stähle hat. Bis heute gibt es jedoch nur wenig fundamentales Verständnis, welchen Effekt Mangan auf die peritekitsche Umwandlung ausübt. In der Literatur werden verschiedene Ansätze zur Untersuchung von Mehrkomponentensystemen beschrieben, wobei es dabei zu Wechselwirkungen zwischen den Legierungselementen kommt und der Effekt einzelner Elemente nicht erklärt wird. Das Ziel dieser Arbeit war es daher, speziell den Einfluss von Mangan auf die δ-Ferrit/γ-Austenit Umwandlung zu untersuchen. Um dies zu erreichen, wurde eine Kombination aus Experimenten in der Hochtemperaturkammer des Laser-Scanning-Konfokal-Mikroskops (HTLSCM) und Eintauchversuchen, sogenannten „dipping tests", von Legierungen mit 0 bis 6 wt.-% Mangan angewandt. Die Ergebnisse der HTLSCM-Experimente zeigten keinen Einfluss von Mangan auf die sogenannte „massive Phasenumwandlung". Es konnten jedoch vorangegangene Forschungsergebnisse bestätigt werden, nach welchen die Geschwindigkeit der massiven Umwandlung vom Anteil an primär erstarrtem δ-Ferrit und der damit verbundenen Unterkühlung bestimmt wird. Sowohl die Ergebnisse der HTLSCM-Experimente als auch jene der Eintauchversuche weisen darauf hin, dass die relative Lage der Legierung zum peritektischen Punkt das Erstarrungsverhalten von peritektischen Stählen maßgeblich beeinflusst. Die mit dem vorgestellten Versuchsaufbau erzielten Ergebnisse der Eintauchversuche für Legierungen mit mehr als 1 wt.-% Mangan scheinen jedoch unabhängig von der Legierungslage zu sein und lassen auf andere Effekte für höher legierte Stähle schließen.

Acknowledgements

First and foremost I would like to thank Prof. Christian Bernhard for his trust to continue the research on this interesting and sophisticated topic. I am truly thankful for all the time he spent on giving me advice and explanations. The success of this thesis is certainly a result of his excellent guidance and outstanding ability to emphasise the positive things. I am also grateful that he has given me the chance to do some of my work in the course of the international collaboration with the University of Wollongong.

Next but not less, I would like to express my sincere gratitude to Prof. Rian Dippenaar for his continuous advise and for letting me join his excellent research community. I will always think back to his encouragement that motivated me for this and future research.

I could not have asked for two better advisors and mentors for my master thesis.

My sincere thanks also goes to Dr. Peter Presoly for sharing his profound knowledge and the most thought-provoking and encouraging discussions. This thesis would have never come to an end without him. As he is the second reader of this thesis I am gratefully indebted for his valuable comments. Especially as he is a young father, I would like to thank him for all his late night work.

I would also like to thank Dr. Suk-Chun Moon for his optimism and the ingenuity to fix the confocal microscope, but also for sharing his professional experience of steel making with me.

Finally, I would like to make a special mention to Stefan Stangl and his team at the melting laboratory of the Chair of Ferrous Metallurgy. The dipping test would have been not possible without their experience, skill and professionalism in melting steel.

Financial support by the Austrian Federal Government (in particular from Bundesministerium für Verkehr, Innovation und Technologie and Bundesministerium für Wissenschaft, Forschung und Wirtschaft) represented by Österreichische Forschungsförderungsgesellschaft mbH and the Styrian and the Tyrolean Provincial Government, represented by Steirische Wirtschaftsförderungsgesellschaft mbH and Standortagentur Tirol, within the framework of the COMET Funding Programme is gratefully acknowledged.

Affidavit

I declare in lieu of oath, that I wrote this thesis and performed the associated research myself, using only literature cited in this volume.

_____

Christian Legerer

Leoben, June 2016

For my family

I dedicate this thesis to my beloved family: to Anita, Helga und Gerhard; for being born and raised in the best imaginable family, for their unconditional love and for giving me the most possible support to be free like a bird.

To Iris and Andreas Filzwieser for encouraging me to study at the Montanuniversität and their professional and personal guidance as well as their contagious enthusiasm for metallurgy.

An dieser Stelle möchte ich auch meinen Großeltern danken, auf deren Grundsteinen all dieses Glück begründet liegt.

He that will not sail unit all dangers are over, will never put to sea.

Thomas Fuller, English clergyman (1608 – 1661)

Life moves its feet forward,
You're the child on the back,
Don't look down, enjoy the ride,
You've got the best view around.

Manon Nyssen (2/2016)

Content

1 Introduction

Perhaps the Greek poet Hesiod (750 and 650 BC) had experience in steel making and was particular troubled with the casting of peritectic steels, when he described the Iron Age as toil and misery for the human existence. Whether or not we live in Hesiods Iron Age shall be left to philosophers and mythologists, but a proud ferrous metallurgist always points out that inconceivable 1.6 billion tonnes of steel that were produced and to a large extend consumed in the year 2015 [1].

Nowadays 93 % of the world steel is produced using the continuous casting process [2]. Peritectic steels account for about 5-10 % of continuously casted slabs at the voestalpine plant in Linz [3]. In continuous casting this group of steels receives particular attention for their negative effect on the casting behaviour in the mould, such as crack formation, heat transfer and temperature fluctuation in the copper plate, mould level fluctuation and oscillation marks formation, and subsequently cause low product quality or even breakouts of the strand shell.

The initial steel solidification inside of the water-cooled and oscillating copper mould is one of the most complex process-steps in steel making and particular continuous casting. In order to guarantee high plant productivity and product quality and minimise cost-intensive downtimes as well as repair-work due to breakouts a fundamental understanding of the peritectic solidification is of great importance. Solidification processes have been extensively researched over more than four decades in order to deeply understand the behaviour of microstructure evolution and how the process parameters influence the solidified structure. Much work has been done on the solidification of peritectic steels to improve their continuous casting behaviour in particular. Largely focused on the iron-carbon system, researchers attempted to gain a better understanding on the fundamental mechanisms underpinning the peritectic phase transition and yet, this interesting phase transition is still not fully

understood. Moreover, there is plenty of industrial evidence that alloying elements such as manganese play a pivotal role in the quality of continuously cast products. Many modern steel grades such as dual phase steels contain high manganese contents. Following the most recent research, the main objective of the present thesis is to investigate the specific influence of manganese on the δ-ferrite to γ-austenite phase transformation.

In the past, the mechanism by which the frequently observed "massive transformation" occurs, has been almost exclusively related to the carbon content and its pronounced diffusion field. The influence of other alloying elements such as manganese and silicon remain controversial and has been subject to little research to date. For this reason, this study aims to explain the effect of manganese on the undercooling below the equilibrium peritectic temperature and the intensity of the massive transformation. Furthermore, the question was raised, if the solidification behaviour of steels within the peritectic range is exclusively influenced by the relative position with respect to peritectic point regardless of the manganese content.

The actual purpose of ferrous metallurgical research can only be the optimisation of the steel making process, which in this case is the prevention of the reported difficulties encountered in steel industry. Therefore I hope that this work will provide some direction to improve the casting of peritectic steels and that the findings are a good scientific basis for future research.

2 Literature Review

2.1 Peritectic Phase Transition

Etymologically the word 'peritectic' consists of two Greek words: peri- 'around' and teko 'melt'. In metallurgy the term peritectic refers to the transition that occurs when a primary solid and remaining liquid phase react to yield a secondary solid phase. For the binary iron-carbon system these peritectic reaction may be written as:

$$\delta\text{-ferrite} + \text{liquid} \rightarrow \gamma\text{-austenite}.$$

Under equilibrium conditions, respectively when all three phases are in equilibrium with each other the transition occurs at the peritectic temperature T_P, represented by a horizontal line at 1495°C in the binary Fe-C system. Figure 2–1 schematically illustrates the peritectic region in the binary Fe-C phase diagram for equilibrium and non-equilibrium conditions. Under non-equilibrium conditions (dashed lines in Figure 2–1), e.g. at increased cooling rates the peritectic region transforms into a three-phase-field and changes its chemical composition and temperature.

Two fundamentally different solidification types can be observed for peritectic alloy compositions. Hence for classification the isothermal line at the peritectic temperature is subdivided into 'hypo-peritectic' and 'hyper-peritectic' alloys. With reference to Figure 2–1 hypo-peritectic refers to the carbon concentration range from C_A to C_B and will contain δ-ferrite and γ-austenite below the peritectic temperature for the iron carbon system. By contrast hyper-peritectic solidification behaviour can be detected for compositions from C_B to C_L. Since in hyper-peritectic alloys liquid will remain below T_P, they have the ability to feed

the contracting shell. It is mainly for this reason that hyper-peritectic steels show better casting behaviour in industrial practice [4].

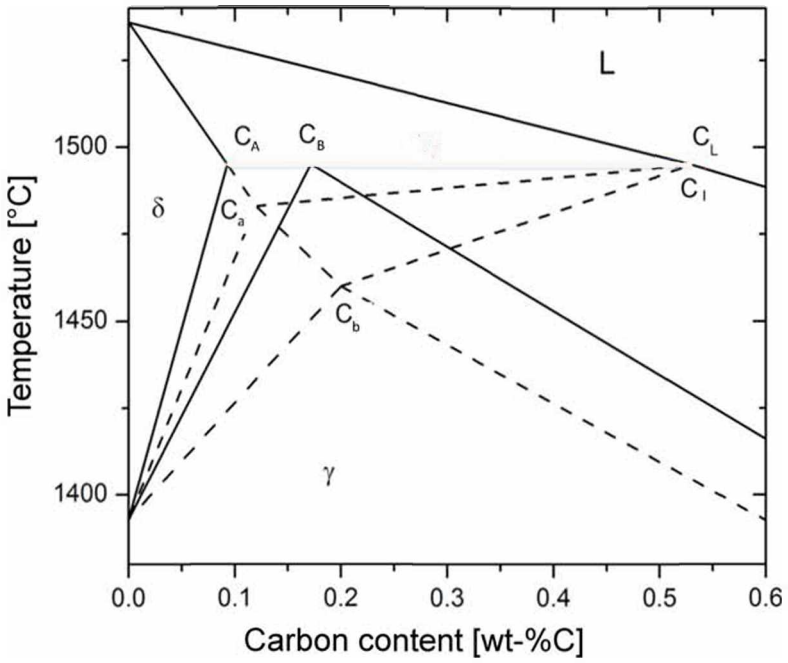

Figure 2–1: Schematic of the peritectic region in the binary Fe-C phase diagram for equilibrium conditions (continued lines) and non-equilibrium conditions with a three-phase-field (dashed lines) [4].

In literature the terms peritectic reaction, transformation and transition are used inconsistently. Therefore Kerr et al. [5] introduced following terminology to distinguish between the different events. They defined that the peritectic transition consists of two separate events, the peritectic reaction and subsequent transformation. The nucleation and growth of γ-austenite along the liquid/δ-ferrite interface, driven by liquid super-saturation, is referred to as peritectic reaction. Once all the liquid/δ-ferrite interface is covered by γ-austenite, i.e. the reaction is completed, the so-called peritectic transformation starts. It is described as the following thickening and growth of γ-austenite into liquid and δ-ferrite (see Figure 2–2) [6].

In recent years, direct evidence of these mechanisms has been provided through in-situ observations of the progress of peritectic reactions and transformation. Shibata et al. [7] were the first to utilise a high-temperature laser-scanning confocal microscope (abbreviated as HTLSCM hereafter) to perform in-situ experiments on peritectic steels. They observed and confirmed that a thin γ-platelet propagates at high-speed along the liquid/δ-ferrite interface – the peritectic reaction. When the interface is covered by the newly formed γ-austenite the transformation begins.

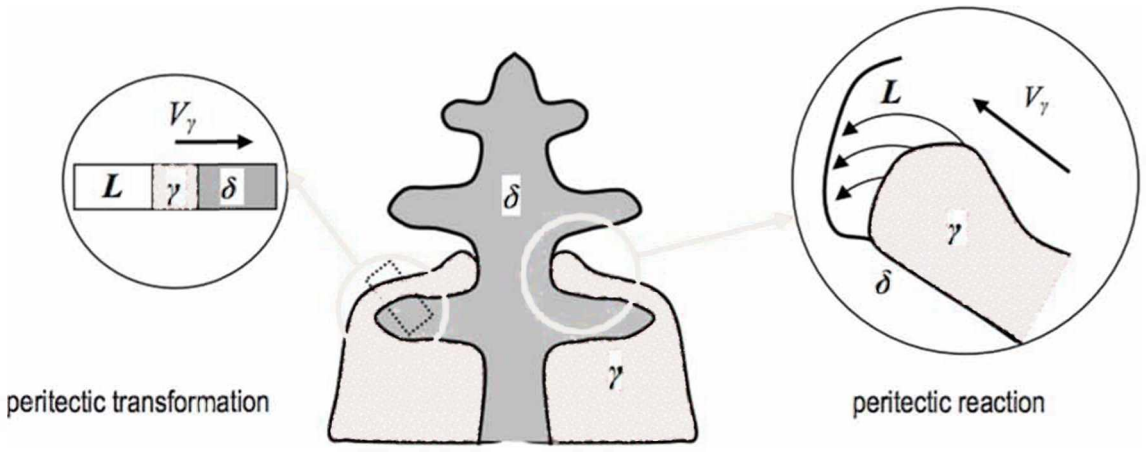

Figure 2–2: Mechanism and terminology of the peritectic phase transition in steel [6].

Stefanescu [6] described the sequence of events more thoroughly stating that the γ-platelet propagation is driven by liquid super-saturation and more importantly that the γ-phase thickens at the same time at the expense of liquid and δ-ferrite. After the γ-austenite film isolates the primary phases, it grows by direct solidification into the liquid and long rang solid-state diffusion into δ-ferrite. As a consequence to local interface equilibrium a concentration gradient is established across the thin γ-platelet, which will be discussed in more detail later on. Additionally, Alves et al. [8] clearly confirmed the two stages of the peritectic transformation, utilising analytical methods, namely 2D simulations of the phase-field method.

However, in earlier works some researchers have treated the distinction between the peritectic reaction and peritectic transformation differently. Griesser [4] and Moon [9] have summarised the topic in greater detail, the following chapter will give a brief round-up of their findings on both stages of the peritectic transition.

2.1.1 Peritectic Reaction

Under equilibrium condition when the temperature reaches the peritectic line, γ-austenite nucleates preferably at δ-ferrite grain boundaries that are in contact with liquid phase. Arai et al. [10] and Griesser [4] experimental investigations show that nucleation can occur at the same site when the temperature is cycled above and below the peritectic temperature. Figure 2–3 shows a nucleation site of γ-austenite. Subsequently to the nucleation γ-austenite grows along the δ-ferrite/liquid interface until it isolates δ-ferrite and liquid entirely from each other. This sequence of events is defined as the peritectic reaction.

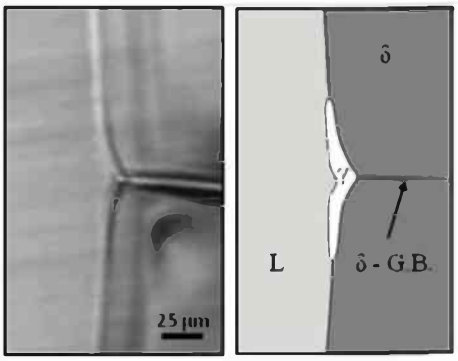

Figure 2–3: Nucleation of γ-austenite at a liquid/ δ-ferrite grain boundary interface [4].

As firstly proposed in 1979 by Hillert [11] the γ-austenite growth is accompanied by the remelting of δ-ferrite ahead of the γ-platelet (see Figure 2–4). He assumed a remelting mechanism controlled by solute diffusion and that the peritectic phase grows along the interface due to the phase diagram requirement that both δ-ferrite and liquid must be available to form γ-austenite.

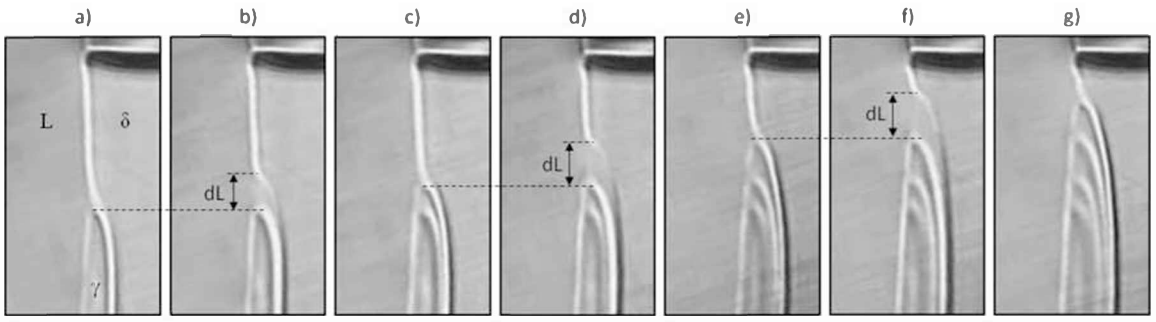

Figure 2–4: Sequence of events during the incremental growth of the γ-austenite platelet [4].

In contrast to the described diffusion model Phelan et al. [12] proposed that the latent heat of fusion liberated by the formation of γ-austenite is absorbed by the δ-ferrite, which is remelted ahead of the γ-platelet. The heat transfer model depicted in Figure 2–5 considers the situation in the immediate vicinity of a growing γ-platelet tip. The authors describe following sequence of events: δ-ferrite remelts as a result of the heat of fusion released by the γ-formation. This remelted δ-ferrite mixes with liquid to form a region of 0.18 wt%C. Hence the γ-platelet propagates into a liquid of exactly the same composition, which does not involve carbon diffusion. Therefore they propose that the reaction is controlled by thermal diffusion. However, Griesser [4] points out that the comparison of experimental observation and the calculations is difficult due to a lack of accurate values for the temperature gradient. Additionally, the proposed model fails to explain the dependency of the reaction velocity on the carbon concentration and the undercooling.

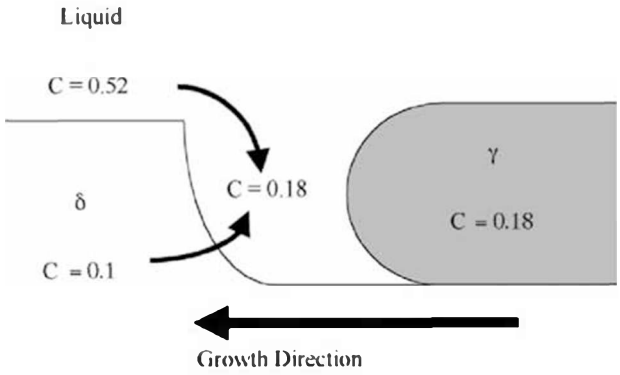

Figure 2–5: Model of peritectic reaction proposed by Phelan et al. [12].

In his own work Griesser [4] argues that the amount of remelted δ-ferrite depends on the temperature and concentration fields around the interfaces. In his experiments depicted in Figure 2–4 the γ-platelet was stabilized at a fixed position at the liquid/δ-ferrite interface, followed by small incremental temperature reductions and the consequential growth. For equilibrium conditions local supersaturation due to rejected solute from γ-austenite leads eventually to a remelting of δ-ferrite in these areas.

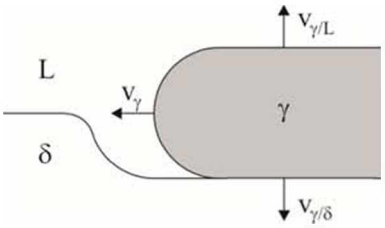

Figure 2–6: Schematic illustration of the peritectic reaction

The amount of remelted δ-ferrite depends largely on the cooling rate, i.e. the progression of the γ-platelet. When the system solidifies under non-equilibrium conditions, the presence of concentration gradients in δ-ferrite lead to a quick transport of the rejected solute away from the interface and therefore no remelting can be observed. Figure 2–7 illustrates that higher cooling rates and, i.e. higher γ-austenite progression rates result in thinner γ-platelets as well as smaller tip radius. Referring to Figure 2–6, the lateral growth along the liquid/ δ-ferrite interface (v_γ) occurs at a higher rate than the thickening of the separating γ-layer ($v_{\gamma/L}$ and $v_{\gamma/\delta}$). Thus, increasing reaction velocities decreases the γ-platelet thickness and tip radius.

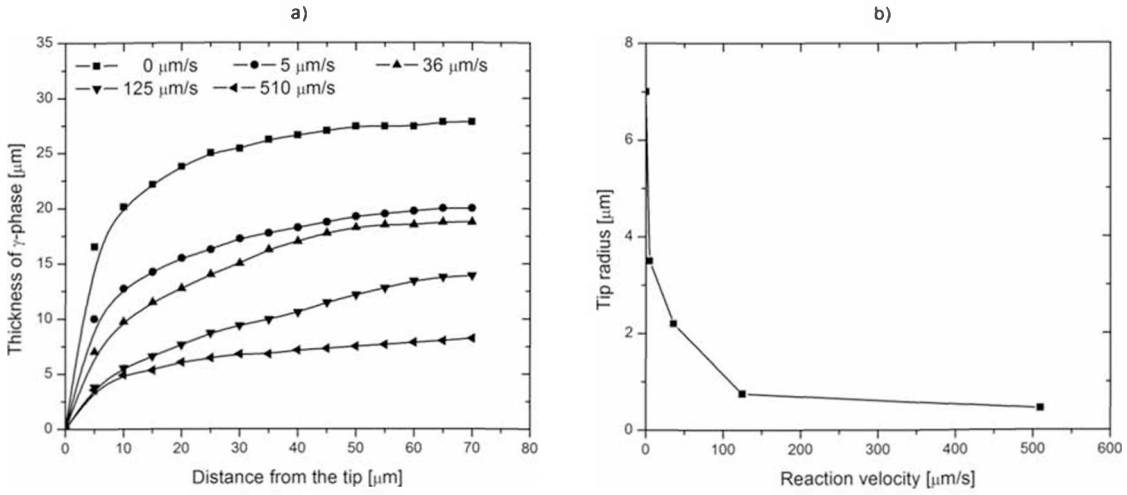

Figure 2–7: (a) γ-platelet thickness at different reaction velocities, (b) dependency of the γ-platelet tip radius on the reaction velocity [4].

Recent in-situ HTLSCM observations of Shibata et al. [7] and Phelan et al. [12] demonstrate that the peritectic reaction in carbon steels is not controlled by the diffusion of carbon. Nassar and Fredriksoon [13] also found that the growth rate of γ-austenite into δ-ferrite at 10°C/min are several millimeters per second and infer therefrom that this high growth rates cannot be explained by diffusion. Hence this fast transition is considered to be a so-called massive transformation, which is further discussed in Chapter 2.2.

As a marked contrast Ohno and Matsuura [14] defend in their work that the peritectic reaction is a diffusion controlled mechanism. The authors base their conclusion on the consistency of their quantitative phase-field model [15] and experimentally measured values shown in Figure 2–8. Furthermore, they argue to have a closer look on the effect of the temperature field on the reaction.

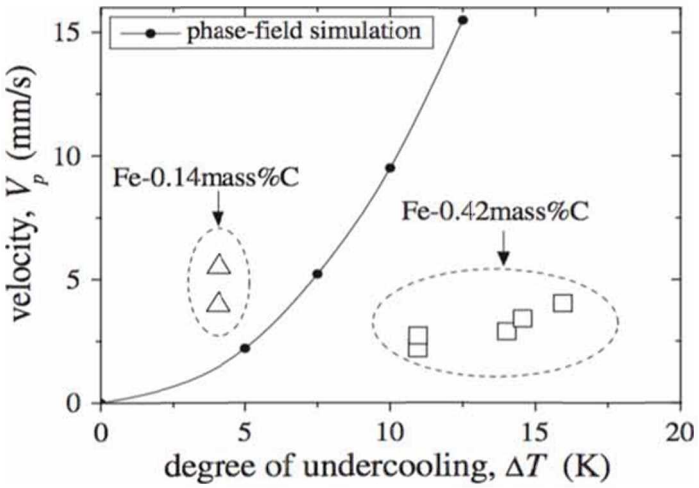

Figure 2–8: Interface velocity versus degree of undercooling of the peritectic reaction, comparison between the experimental observations of Matsuura [16] and the results of the phase-field simulation by Ohno et al. [14].

2.1.2 Peritectic Transformation

The sequence after the local isolation of liquid and δ-ferrite by the growth of the γ-austenite platelet, i.e. peritectic reaction, is defined as peritectic transformation which is comprised of the liquid to γ-austenite and δ-ferrite to γ-austenite phase transformations. The peritectic transformation due to the accompanied volume contraction of about 6 % is agreed to be a root cause of a variety of problems in conventional continuous casting processes of peritectic alloys. The growth of γ-austenite layer into the liquid and δ-ferrite starts immediately for the iron-carbon system. Controversially for the iron-nickel system, due to the reduced diffusivity of nickel, peritectic reaction and transformation are clearly separated [11].

Shibata et al. [7] were the first to quantitatively measure the rate of γ-austenite progression into liquid and δ-ferrite, utilising the newly developed HTLSCM technique. Figure 2–9 depicts a comparison of calculated and observed interface propagations in a 0.42 wt-% C alloy. They found that in the iron-carbon system for a diffusion controlled process the growth rate of γ-austenite into δ-ferrite was higher that of γ-austenite into liquid. Furthermore, a hypo-peritectic 0.14 wt-% C alloy and a hyper-peritectic 0.42 wt-% C alloy were investigated at cooling rates between 1 and 20 K/min. As expected the hyper-peritectic alloy exhibited a growth rate that was proportional to the square root of time, which is hence diffusion-controlled growth. However, the γ-austenite to δ-ferrite transformation in the 0.14 wt-% C alloy occurred only in a fraction of a second. Hence, the authors concluded that this fast transformation cannot be controlled by diffusion but rather by a massive transformation.

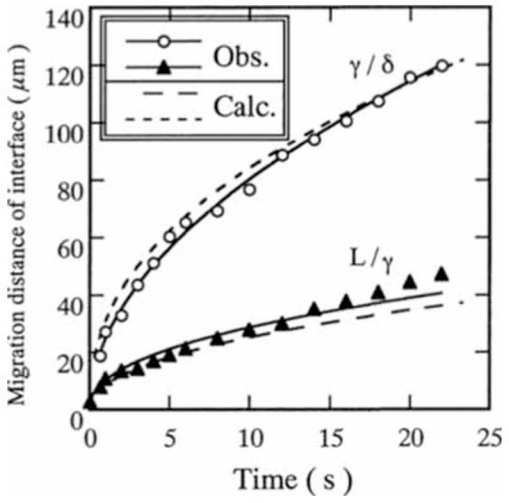

Figure 2–9: Calculated compared with observed migration distances of γ-austenite/δ-ferrite and liquid/γ-austenite boundary during peritectic transformation of Fe-0.42 wt-% C alloy during directional solidification (Cooling rate 1 K/min) [7].

The rate of the peritectic transformation depends strongly on the cooling rate and undercooling below the equilibrium peritectic temperature. Phelan et al. [17] found that for a cooling rate of 10 K/min the solid/solid interface velocity is lower than of the liquid/solid interface. Therefore they concluded, with reference to the shape of the iron-carbon phase diagram, that due to the small compositional gap across the solid/solid interface less solute diffusion is required, subsequently resulting in faster interface propagation. Interestingly they found that for a cooling rate of 100 K/min the liquid/solid interface has a higher growth velocity than the solid/solid interface. An attempt was made to explain the observed interface velocity inversion by assessing the solute profiles for the respective cooling rates. Figure 2–10 shows the simulated solute profiles for both cooling rates at the time of nucleation of γ-austenite and after the peritectic reaction is completed, i.e. a substantial volume of γ-austenite separates liquid and δ-ferrite.

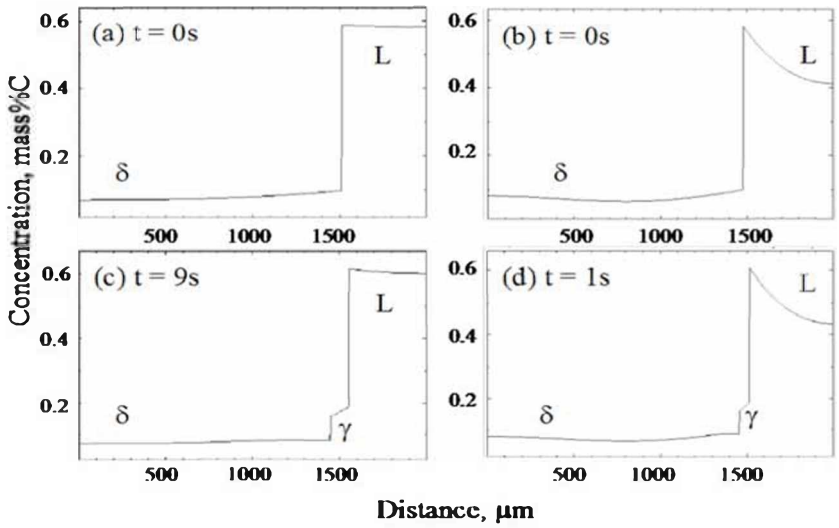

Figure 2–10: Comparison of simulation solute profiles for cooling rates of (a) and (c) 10 K/min and (b) and (d) 100 K/min, in an Fe-0.18wt%C alloy, under a temperature gradient G = 200 °C/cm; t = 0 refers to the initiation of the peritectic phase transition [17].

As can be clearly seen, the solute profile in the liquid under a 100 K/min cooling rate is much steeper than the profile that develops at a cooling rate of 10 K/min. The reason for that is that at higher cooling rates there is less time available for solute diffusion, resulting in a steeper solute concentration profile. According to Fick's Law in addition to the diffusion coefficient of carbon in the liquid, the concentration gradient in the liquid determines the flux of carbon across the liquid/ γ-austenite interface. Phelan et al. [17] verified the phase-field modelling by experimental observations and subsequently concluded that the interface velocity inversion due to increased cooling rates is a result of an enhanced solute flux into the liquid. Additionally, the high cooling rates in the performed HTLSCM experiments lead to the in-situ observation of the so-called massive transformation, which is explained in further detail in the next chapter.

2.2 Massive Transformation

Hillert [18, 19] defined the massive transformation as "the composition-invariant counterpart of diffusional growth of the allotriomorphic form of precipitation" or "the partitionless counterpart of the partitional precipitation of allotriomorphs." Partitionless transformation means the components do not partition between parent and product phase. In this context "allotriomorph" refers to morphologies exhibiting a shape that does not reflect its internal crystalline symmetry and usually nucleates along grain boundaries. It is more commonly used for allotriomorphic ferrite and represents the opposite of "idiomorph". Simply put, massive transformation is a rapid phase transformation in an alloy [20].

Generally there are two well-known partitionless transformations in metallic materials called "martensitic" and "massive". Usually the martensitic transformation is very rapid and comes close to the true diffusionless case, thus creating strong stresses, which require high driving forces. However, the massive transformation is not true diffusionless and is to be clearly distinguished from the martensitic transformation. Even though it is rapid, there may be time for individual atoms to diffuse across the interface and maybe even for a pile-up to form. But no long-range diffusion will be required and the transformation is composition-invariant. Hillert [18] also points out that nucleation will still be concentrated to the grain boundaries, but the growth rate will increase drastically.

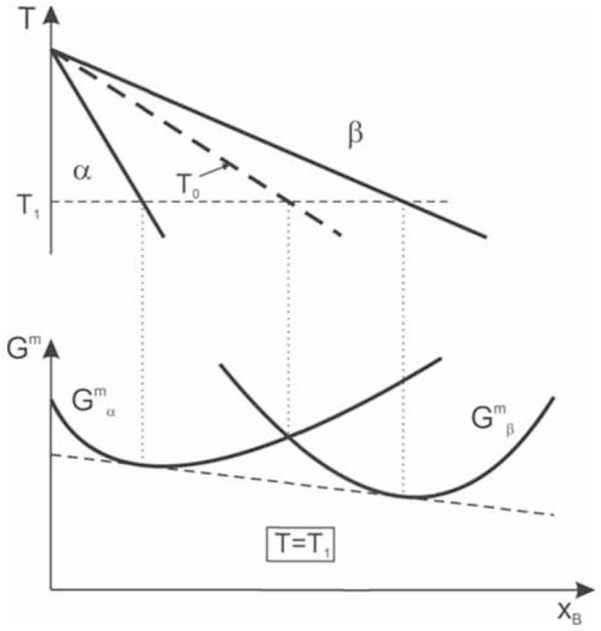

Figure 2–11: Construction of the T_0-line [19].

If only the chemical Gipps energies are considered, the thermodynamic-energy condition for massive transformation must be: the Gipps energy of the product phase is smaller than

that of the parent phase for the same composition. The limit for this condition is the "allotropic phase boundary", which is often denoted as T_0-line. The allotropic phase boundary is a function of temperature and composition, which are found by the points of intersection of the respective Gipps energy curves as shown in Figure 2–11. Here the two phases have the same Gipps energy value if they had the same composition. It is the critical limit for a hypothetical diffusionless phase transformation. The word "allotropy" derives from the property of a substance of being found in two or more forms [18, 19].

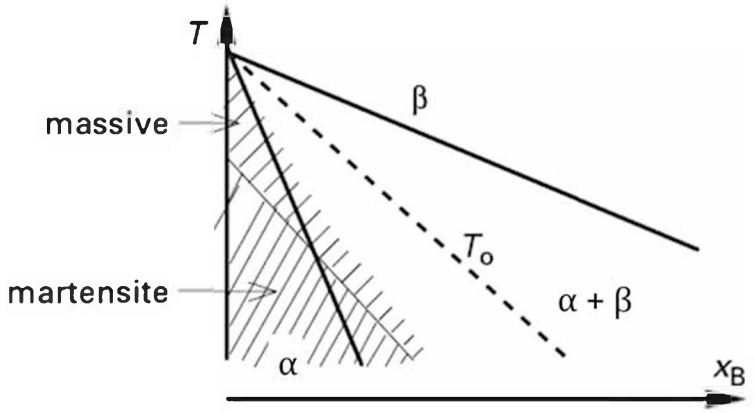

Figure 2–12: Possible regions of massive and martensitic transformation in a generic T, x_B diagram [18].

Figure 2–12 gives a phase diagram in which regions are marked where one could expect the massive and the martensitic transformation. It can be clearly seen that the martensitic transformation can occur far inside the α + β two-phase region but only at a considerable distance below T_o line due to the necessity of a pronounced driving force. In the case of martensitic transformation all atoms cross the interface with some kind of a cooperative mechanism. For a rapid massive transformation the driving force may not be sufficient and the mechanism of transfer of atoms across the interface must be partly cooperative. Hence this transformation may fall well between the two limiting cases, namely diffusion-controlled transformation and martensitic transformation [18].

Figure 2–13 indicates the position of the massive transformation with respect to other transformations in an exemplary CCT diagram. The driving force for massive transformation is large, orders of magnitude larger than for grain coarsening, but pronouncedly smaller than in martensitic transformation [21]. The next chapter aims to explanation the massive transformation in the context of continuous casting.

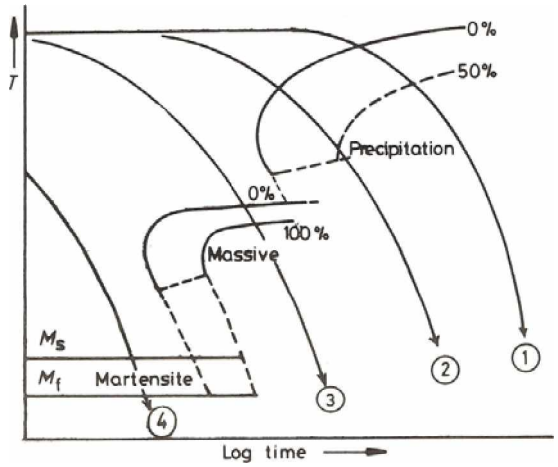

Figure 2–13: Exemplary CCT diagram for systems showing massive transformation [22].

2.2.1 Massive Transformation in the Iron-Carbon System

The mechanism by which massive transformation occurs has never been satisfactorily explained. Nevertheless, Dippenaar et al. [23] point out the fact that this phase transition is the root cause of many quality defects encountered in the continuous casting of steel. Many studies have reported that the occurrence of massive transformation in peritectic systems is linked to significant undercooling [7, 10, 24]. In their recent work Griesser et al. [25] argue that the transformation mechanism is connected to a nucleation constraint. The authors are the first to correlate the nucleation constrain of γ-austenite to the magnitude of diffusion fields developed at the liquid/solid interface prior to γ-austenite. Once nucleation of γ-austenite has occurred at a certain undercooling below the equilibrium peritectic temperature, the thermodynamic driving forces for the transformation of δ-ferrite into γ-austenite lead to increased kinetics of the peritectic reaction and transformation.

Table 2–1: Investigated alloys and their transformation behaviour [25].

Sample	Equilibrium fraction of solid at Tp [%]	Carbon concentration gradient [m^{-1}]	Undercooling (Tp-T) [K]	Transformation Behaviour
Fe-0.43C	23	4	0	Slow reaction and planar transformation
Fe-0.18C	81	36	4	Fast reaction and unstable transformation
Fe-0.10C	98	78	22	No reaction and massive transformation

Griesser et al. [25] conducted experiments with three different carbon-containing alloys that have been solidified with an applied cooling rate of 10 K/min. In Figure 2–14 the average

($\bar{C}_\delta$) and interfacial (C_δ^*) compositions of the alloys are plotted until the peritectic transition occurred. Additionally, the Gipps energy curves for the respective solidification temperatures are illustrated. Table 2–1 gives the carbon concentration gradients at the pertinent peritectic transition temperature of the investigated alloys, which were evaluated using the software package "DICTRA". Evidently with decreasing carbon content the equilibrium fraction of solid at the peritectic temperature increases. This leads to the formation of a steeper carbon concentration gradient. The resulting stronger diffusion field of carbon atoms across the liquid/δ-ferrite interface causes further undercooling below the equilibrium peritectic temperature.

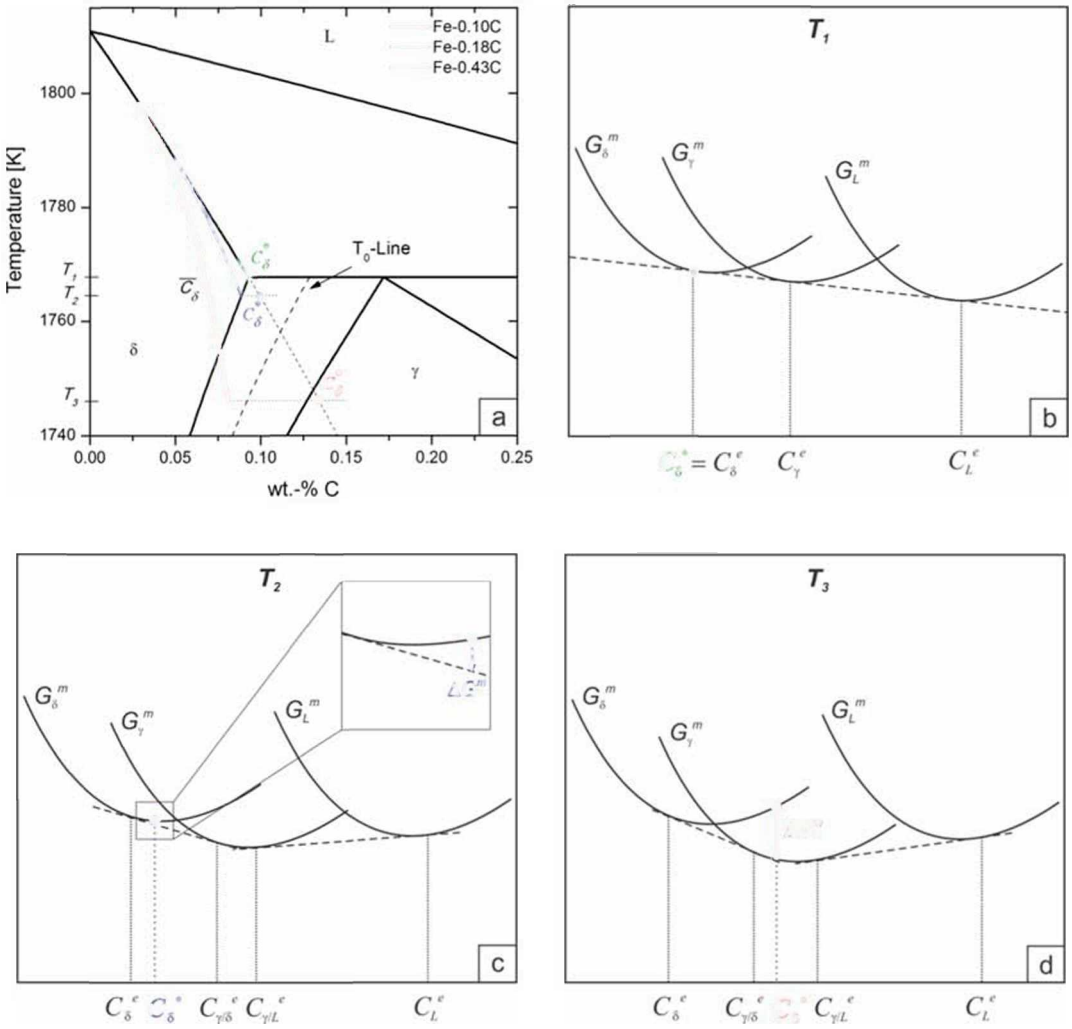

Figure 2–14: Average ($\bar{C}_\delta$) and interfacial (C_δ^*) compositions of three solidifying alloys in the binary iron-carbon phase diagram (a) and the Gibbs energy curves at the respective transition temperature (b-d) [25].

The Gipps energy curves in Figure 2–14 illustrate how the increased undercooling results in a larger thermochemical driving force and the consequential faster reaction speed. Griesser et al. [25] identified three different modes of transition. Figure 2–15 shows the

time-depended progress of the peritectic transition modes based on in-situ HTLSCM observations. The amount of undercooling below the equilibrium peritectic temperature determines the reaction speed and respective γ-austenite propagation velocity. Hence the transition time for the massive transformation is only a fraction of a second, see Figure 2–15.

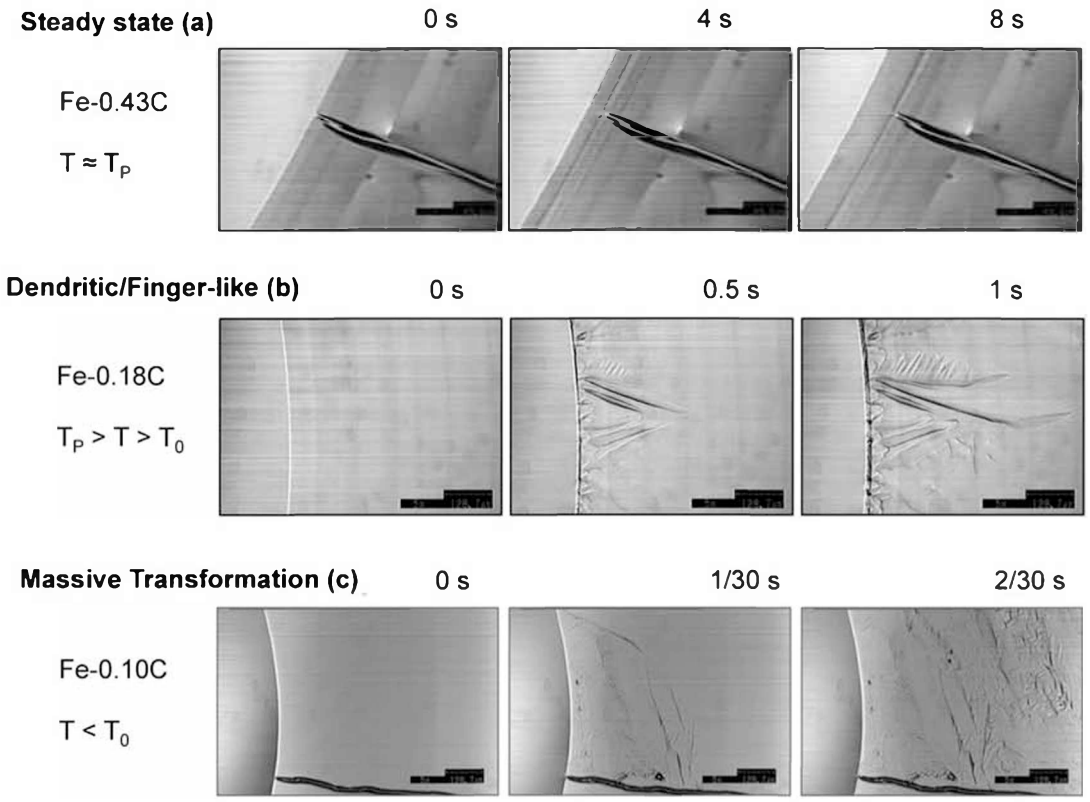

Figure 2–15: Three different modes of the peritectic phase transition [4].

With reference to Figure 2–14 if the temperature of the liquid/δ-ferrite interface drops below the allotropic phase boundary T_o of the corresponding composition (C_δ^* in Figure 2–14), massive transformation of δ-ferrite to γ-austenite occurs, provided that the γ-austenite is sufficiently constrained via diffusive suppression. In their experiments Griesser et al. [25] argued that higher primary δ-ferrite fractions lead to steeper solute concentration gradient due to partioning and insufficient back-diffusion of solute elements during solidification. These concentration gradients result in a diffusion flux of carbon through the liquid/δ-ferrite interface. The authors are of the opinion that the higher the magnitude of this flux, the higher is the undercooling before the initial nucleation. Hence, if nucleation is sufficiently constrained by diffusional suppression, the alloy can be undercooled to a temperature below T_o and a massive transformation can occur. Additionally, they quantified the influence of the cooling rate and addition of silicon [26]. Despite Griesser's [4] efforts to explain the role of manganese on the peritectic transition, it remains unclear. Chapter 2.3 gives further inside

into why the main objective of the present work is to clarify the effect of manganese on peritectic steels.

2.2.2 Transformation Modes in an Operational Continuous Caster

According to Moon et al. [27], in close proximity to the liquid/solid interface in a solidifying steel shell within a continuous casting mould two different conditions are expected. The two conditions as well as the cooling rate at the liquid/solid interface along the solidifying strand are illustrated in Figure 2–16.

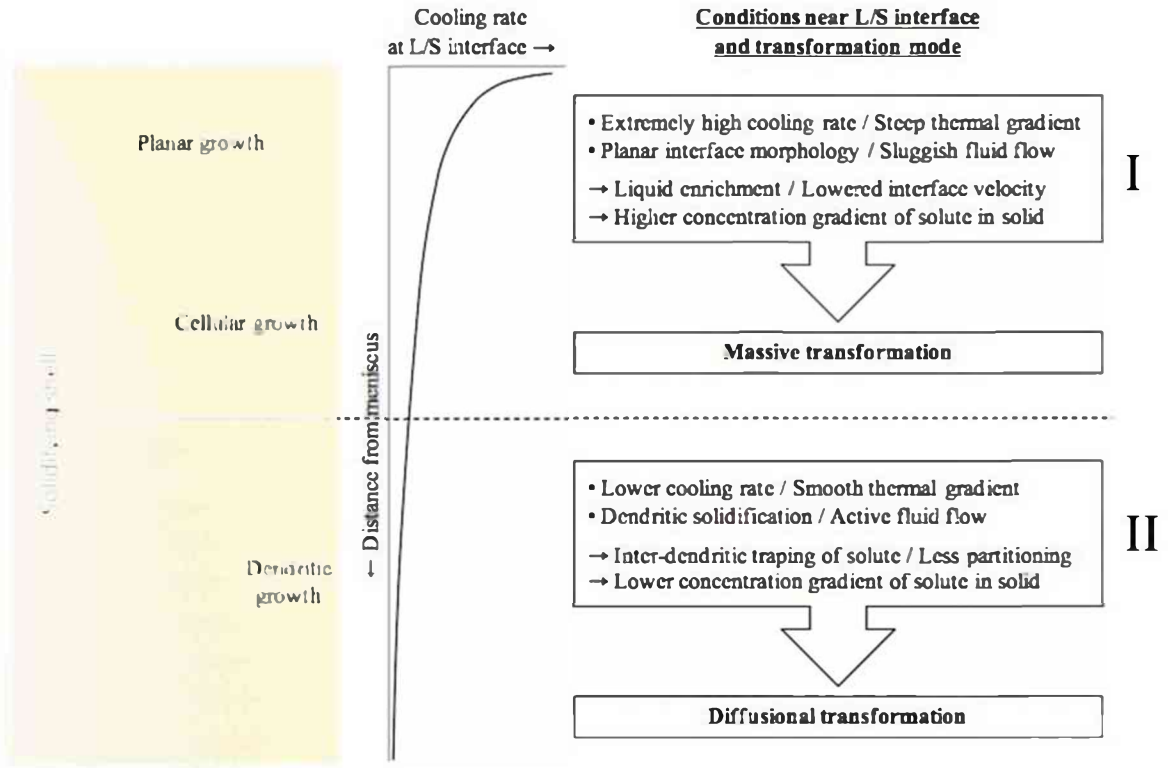

Figure 2–16: Schematic diagram of two distinct conditions in proximity to the liquid/solid interface in a solidifying steel shell within a continuous casting mould and the resulting transformation modes [27].

In close proximity to the meniscus high cooling rates result in a planar liquid/solid interface growth and the concomitant solute element build-up in the liquid ahead of the growing planar interface. The large distance from the submerged entry nozzle leads to unfavourable flow conditions, which prevent the solute-enriched liquid layer from mixing with fresh steel. Consequently, as discussed in Chapter 2.2.1, the high concentration gradient respectively diffusional flux favours the occurrence of massive transformation. Additionally, the presence of a solute enriched liquid layer at the solidification front delays the solidification, which results in an increased distance of planar shell growth below the meniscus. However, the

high stresses imposed by the massive transformation pose a risk of distortion of the thin solidifying shell. Contrary conditions prevail lower down in the mold. The lower cooling rate and increased rate of fluid flow result in the formation of a dendritic structure [27].

In approach to explain the initial solidification Xia [28] carried out a computational simulation of the solidifying shell 100 mm below the meniscus for a slab casting plant. The described solidification model examines the shell thickness, the size of phase regions and position of phase fractions as a function of the distance from the meniscus for representative alloy compositions. The author defines the range of solid phase fraction f_s = 0.8-1 as "brittle-zone", where steel can transmit load but has no toughness. In case that the δ-ferrite to γ-austenite transformation occurs within the "brittle-zone", the early-formed shell is more prone to distortion and defects. Figure 2–17 shows the simulation results for different carbon contents. The four calculated alloys lie within the three regions described in Chapter 2.1. Note that the δ-ferrite to γ-austenite transformation-region is shifted towards the meniscus with increasing carbon content.

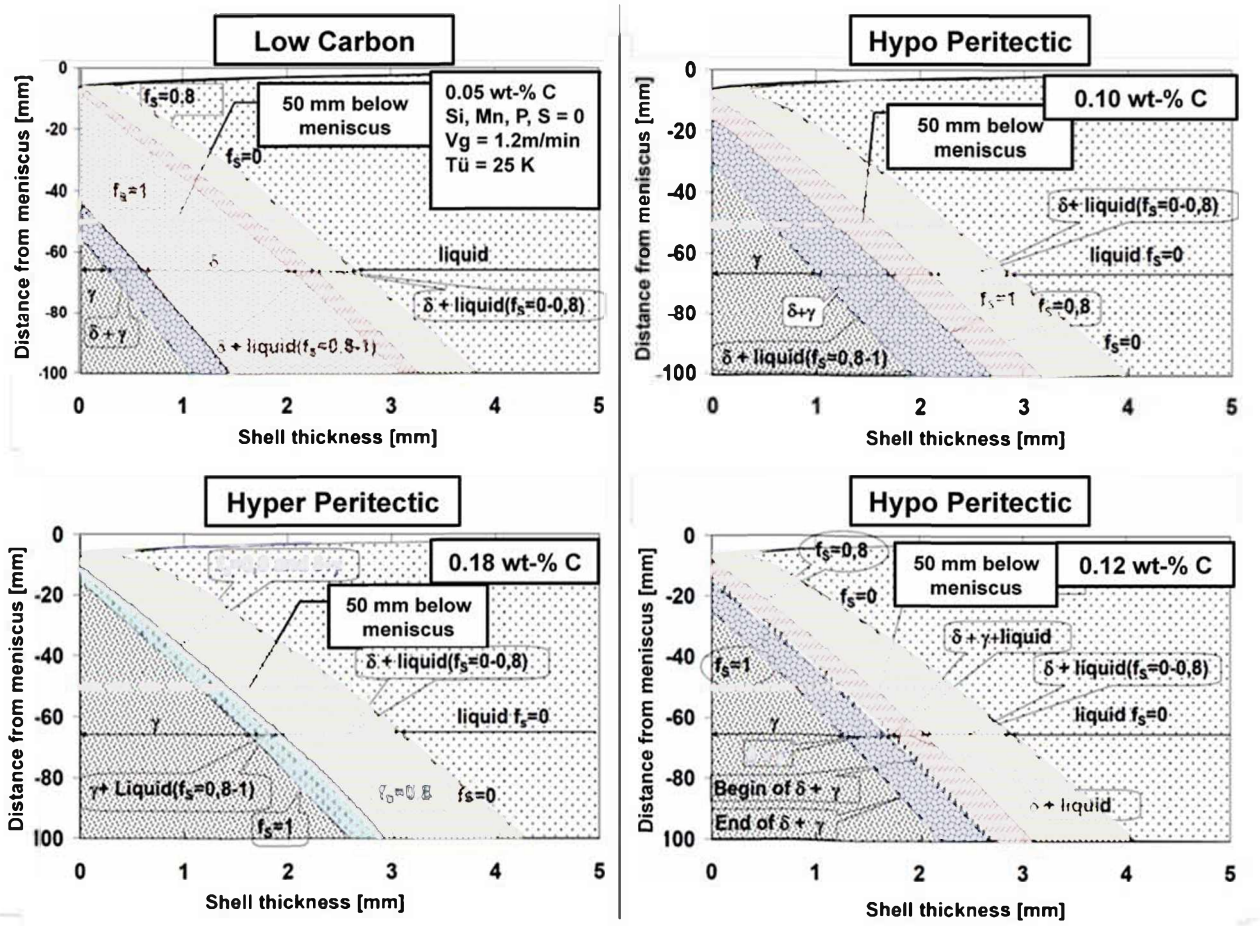

Figure 2–17: Solidification simulation of the meniscus region for different carbon contents [28].

In hypo-peritectic alloys, 0.10 and 0.12 wt.-% C, the δ-ferrite to γ-austenite transformation occurs about 15 mm below the meniscus at a small shell thickness of 0.30 mm and 0.22 mm respectively. In Figure 2–17 the transformation takes place at the boundary of the red and blue marked regions of the hypo-peritectic alloys. The low hydrostatic pressure at this distance from the meniscus is not enough to press the contracting shell flat onto the mould surface. This fact together with the minimal shell thickness is believed to be the cause for the shell distortion and concomitant separation from the mould. The bulging shell can lead to the formation of a coarse grain due to decreased heat removal. Coarse grained combined with reduced ductility increases the crack susceptibility and leads to surface quality issues. In contrast the shell thickness for the low-carbon alloy is 1.6 mm prior to transformation. For the hyper-peritectic alloy the transformation only occurs in a small region at the very start of the "brittle zone", marked as blue line in Figure 2–17. Here the strand-shell has no ability to transfer load and hence causes no shell distortion. Additionally, at 50 mm distance from the meniscus the hypo-peritectic 0.12 wt.-% C alloy displays the widest "brittle zone".

Finally, it could be argued that Xia's [28] considerations based on the computational modelling of diffusion-controlled microsegregation combined with the theory of the massive transformation presented by Moon et al. [27] are the reason for the difficulties encountered in continuous casting of peritectic steels. In a possible approach one could imagine the initial solidification of a hypo-peritectic alloy in the uppermost part of the mould. Here the massive transformation occurs in an extremely thin strand shell at a depth below the meniscus where only a small hydrostatic pressure is prevailing. The contraction due to the phase transformation can cause a deformation of the initial shell, resulting in a loss of contact with the mould, which is a favourable starting point for surface defects.

2.3 Manganese and the Iron Carbon System

Manganese is after carbon one of the most common alloying element in steels. Although to a much lesser extent than carbon, manganese increases the tensile strength of steel, due to solid solution hardening. More importantly manganese decreases the critical cooling rate during hardening, hence improving the steels hardenability. Therefore manganese is used in a wide variety of steel grades from micro-alloyed steels to advanced high-strength steels (AHSS) to TWIP steels. But industrial experience has shown that among other things this hardening effect is associated with increasing difficulties at the continuous casting process. One objective of the presented work is to give further inside on the roll of manganese on the solidification of steels, especially peritectic steel grades. This chapter aims to explain the reasons based on earlier work that leads to the conducted investigation. Figure 2–18 depicts

how the manganese content shifts the peritectic point of the iron-carbon equilibrium phase diagram to the lower carbon concentrations and slightly lower temperatures [9].

Griesser [4] studied the influence of manganese on the peritectic reaction by means of the addition of 0.48 wt-% Mn to an Fe-10 wt-% C alloy. Due to the very small contribution of manganese to the calculated overall diffusion field (see Chapter 2.2.1) and the almost unchanged interface velocity, he reasoned that manganese is not the root cause for constrained nucleation of γ-austenite. However, Griesser's [4] experiments involved only one manganese containing sample with 0.1 wt-% C, which is a hypo-peritectic steel.

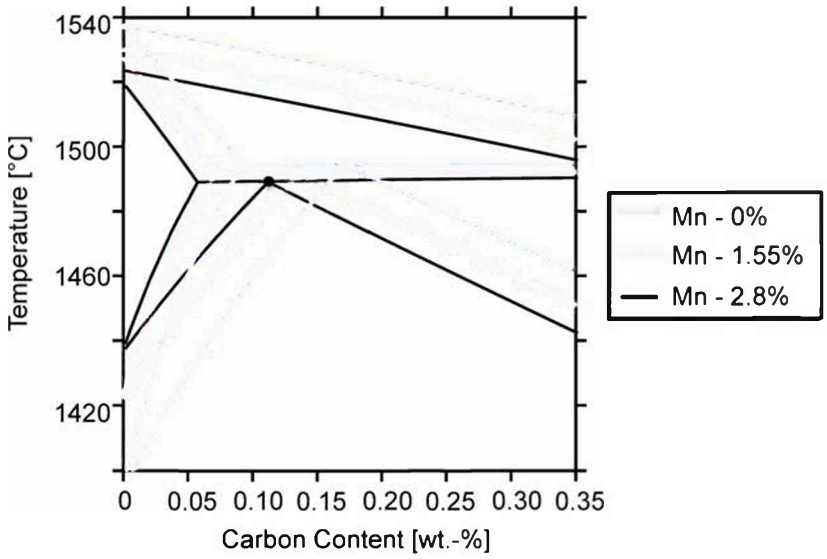

Figure 2–18: Influence of manganese on the binary phase diagram iron-carbon [29].

Bernhard and Xia [30] used the so-called SSCT (submerged split chill tensile) test to measure the contraction forces and the total crack length occurring during steel solidification, which allowed them to draw conclusions on the crack susceptibility. They investigated the role of various alloying elements including manganese. According to their findings manganese behalves relatively neutrally and does not effect the crack susceptibility.

In his recent study Moon [9] investigated different steel grades in a variety of experiments. Looking at his HTLSCM results it can be noted that low manganese steels exhibited stable morphologies whereas manganese contents larger than 1.5 wt-% lead to unstable conditions. Additionally, Moon concludes after conducting SSCC (submerged split chill contraction)-experiments with three industrial alloys, that a higher manganese content seems to increase the maximum contraction force as shown in Figure 2–19. Table 2.1 gives the composition of the investigated alloys.

Table 2.1: Specimen composition used by Moon [9].

Steel	Description	C	Mn	Si	Al	Ti	N	Nb
B	Plain Carbon	0.051	0.305	0.016	0.029	0	0.0109	0
E	TMCP	0.08	1.599	0.278	0.025	0.012	0.0029	0.018
G	Dual Phase	0.085	2.82	1.013	0.027	0.0158	0.0159	0.02
Reference		0.05	1.55	0.3	-	-	-	-

According to the thermodynamic data the steels were characterised due to their solidification mode: steel B and the reference steel – low carbon/non-peritecitc, steel E – hypo-peritectic, and steel G – hyper-peritectic. In addition it has to been pointed out that Moon [9] conducted DCS-measurements for a 2.8 %Mn and 1 %Si alloy, showing that the Thermocalc data was not in good relation to the phase diagram. Therefore Moon [9] concluded that steel G also exhibits a hypo-peritectic solidification behaviour, which can explain the higher contraction force. Looking at the compositional data in Table 2.1 and the respective solidification modes, it can be argued that the increased maximum contraction force is not solely owed to the high manganese content of steel E and G. Instead the hypo-peritectic character or the significant amount of silicon and its interaction with manganese could be the decisive factor.

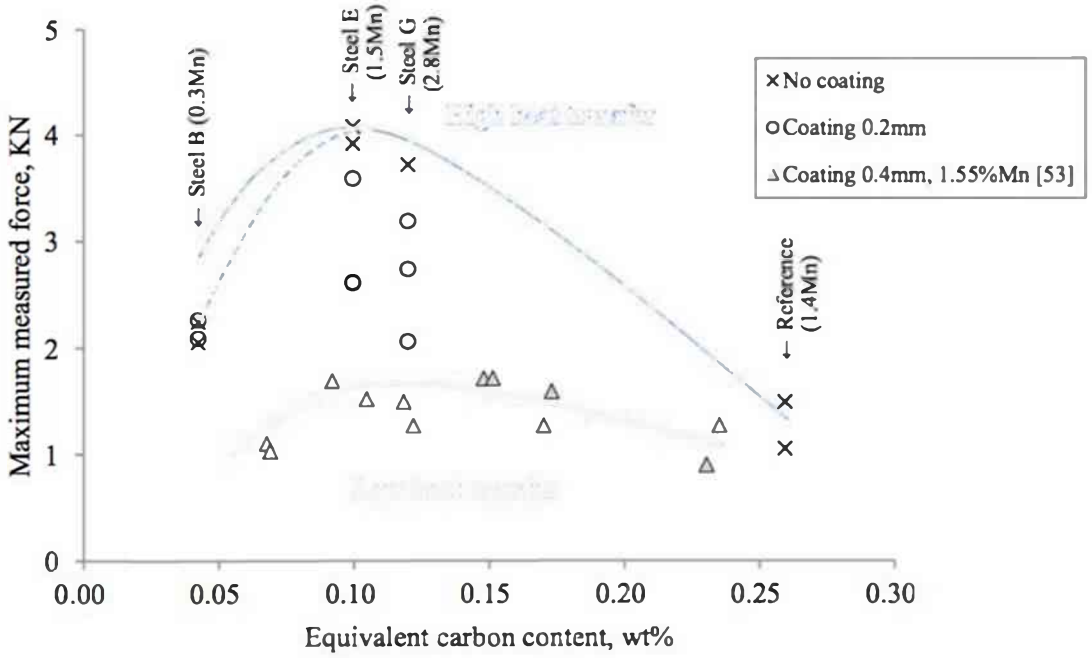

Figure 2–19: Maximum force in SSCC tests over equivalent carbon content (wt% = [%C]+0.04[%Mn]+0.1[%Ni]-0.14[%Si]) by Moon[9]. Reference values by Bernhard and Xia [30].

Considering both the SSCC and the HTLSCM results of the presented studies, the objective of the present study is to give more insight on the role of manganese on the solidification of peritectic steels. In order to do that, this work aims to answer following two questions:

1) Do higher manganese contents increase the undercooling below the equilibrium peritectic temperature and does this intensify the massive transformation of the peritectic transition?
2) Is the solidification behaviour of steels within the peritectic range exclusively influenced by the relative position with respect to C_A / C_B regardless of the manganese content?

3 High-Temperature Laser-Scanning Confocal Microscopy

In the past few decades the development and improvement of experimental techniques capable of capturing images at elevated temperatures enabled in-situ experimental observation of solidification phenomena and high temperature phase transformations of metals. Transmission X-ray observation using a Bridgeman furnace and high-temperature laser-scanning confocal microscopy (HTLSCM) have been utilised to improve the fundamental understanding of the morphology and kinetics of phase transformations during or following solidification.

In 1961 Minski [31] patented conventional laser-scanning confocal microscopy (LSCM). It was not until 1996 when Emi and his colleagues [32] combined LSCM with an infrared image furnace (IIF), allowing the microscopy of metals at melting temperatures. Subsequently a variety of studies conducted with this technique observed and analysed the δ-ferrite to γ-austenite interfaces in low carbon steels [33], inclusion agglomeration [34, 35], inclusion engulfment [36], the crystallization of slags and dissolution of alumina inclusions in slag [37].

Important milestones leading to the present work: In 2000 Shibata at al. [7] were first to utilize HTLSCM to study the peritectic reaction of iron-carbon alloys employing a rectangular crucible. McDonald and Sridhar [38] examined the reaction rate of iron-nickle alloys, by means of LSCM combined with IIF but using a cylindrical crucible.

Reid et al. [39] introduced the concentric solidification technique in 2004, which will be described in more detail in this chapter. This observation enhancement allowed a more thoroughly investigation of the peritectic transition in closer relation to continuous casting conditions. Arai et al. [10] were first to observe and determine the characteristics and rates of

the peritectic transition. Following this, Phelan et al. [12, 17] studied the kinetics of the peritectic reaction.

Recently, Griesser [4] depicted a model for nucleation in a diffusion field validated by experimental data investigating Fe-C and Fe-Ni alloys, which attempts to give an explanation for massive transformation (see Chapter 2.2.1). Furthermore, Moon [9] summarized the effect of the peritectic reaction on crack formation regarding the practical continuous casting process. Following this developments the next chapters aim to give closer insight on the applied experimental technique.

3.1 Confocal Microscopy

The name "confocal" derives from the fact that the focus of the objective lens is the same as the focus of the detector. In the microscope this is achieved by using laser light for point illumination and a confocal pinhole in an optical conjugated plane in front of the photo detector. With this setup, illustrated in Figure 3–1, Minski [31] provided a solution to overcome some limitations of conventional light microscopy. The out-of-focus light is blocked by the pinhole, enabling to obtain high resolution and contrast of a thin optical section close to the focal plane. To reduce long exposure times and increase signal intensity, due to the large quantity of blocked photons at the pinhole, a high intensity laser beam is used.

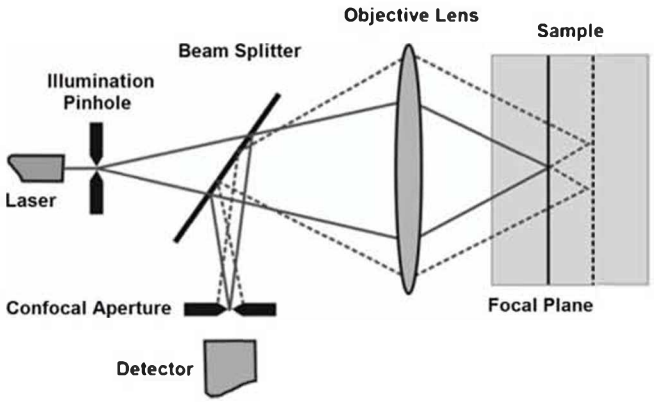

Figure 3–1: Schematic representation of the confocal microscope [4].

Additionally, beneficial for the application in HTLSCM is the fact that thermal radiation is blocked by the confocal pinhole, providing sharp images produced only by the reflection of the laser beam. As the name "scanning" confocal microscopy indicates, respectively in consequence of point illumination, the image is built up by scanning over a rectangular raster of the specimen, which is then stored in an imaging system for subsequent display.

3.2 Experimental Setup

The presented study was conducted using the experimental setup illustrated in Figure 3–2. Present chapter gives further details on the utilised HTLSCM manufactured by Lasertec Corp. and the image furnace ULVAC PRC-MR-500. The microscope can obtain magnifications from 5 to 1350 times at a resolution of 0.25 µm, using a He-Ne laser of 632.8 nm and a beam diameter of 0.5 µm. The scanning rate for the reflected beam is 15.7 kHz in horizontal and 60 Hz in vertical direction.

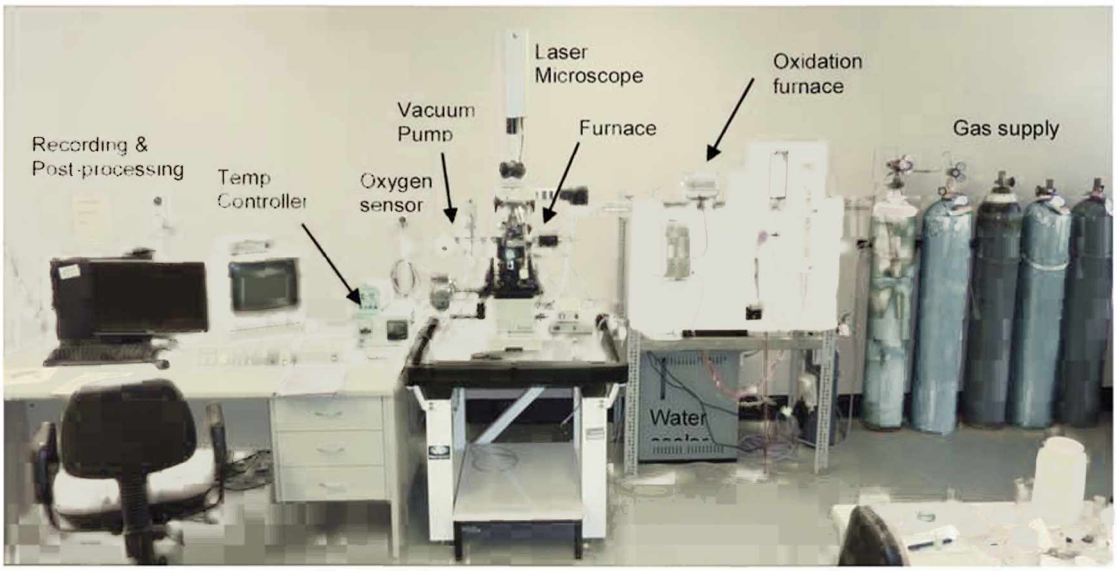

Figure 3–2: Experimental setup of the HTLSCM at the University of Wollongong.

Figure 3–3 shows a schematic cross-section through the IIF, which is a spot-focused gold image furnace with a rotational ellipsoidal reflective surface. It is capable of a temperature increase up to 1800°C by focusing infrared light. Additionally Figure 3–3 shows the specimen position at the upper focal point opposing a 1.5 kW halogen lamp located at the bottom focal point. An OMRON ES100P digital PID-controller regulates the power input by reference to the difference of adjusted and measured temperature. Water-cooling both IIF half shells and the air-cooled lamp chamber minimize the thermal load.

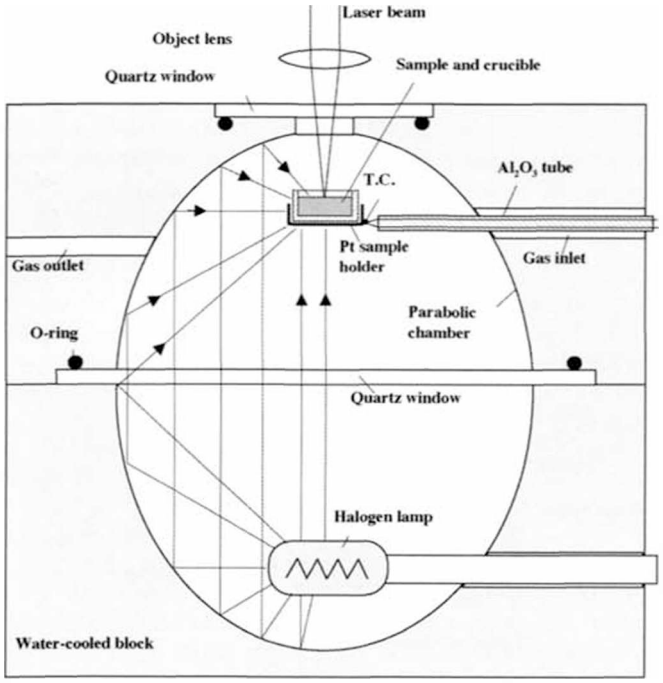

Figure 3–3: Schematic cross-section of an infrared image furnace [40].

3.2.1 Sample geometry

As briefly stated before three different sample geometries (see Figure 3–4) have been used in the HTLSCM throughout a variety of studies. Phelan [41] gives a more detailed description on the use of rectangular crucibles. His results highlight the ability of the rectangular setup to conduct directional solidification experiments, on the other hand it shows limitations in the regulation of the temperature gradient.

The most common crucible for HTLSCM studies is the cylindrical geometry with 5 mm diameter and 3 mm height, which has been developed by the manufacturer. Beneficial for this geometry is the small radial temperature gradient that can be established resulting in a more uniform temperature distribution throughout the specimen. The third geometry is designed for the so-called concentric solidification developed by Reid et al. [39], which will be described in the next chapter.

Figure 3–4: Crucible geometries for rectangular (left), cylindrical (middle) and concentric (right) samples.

Griesser [4] carried out a benchmark between this three sample geometries for the study of the peritectic phases transition. For the rectangular and the cylindrical geometry he found that a strong meniscus formation of the liquid melt prohibits the direct observation of the triple point liquid/γ-austenite/δ-ferrite. He states that the shallow depth of the focus in confocal microscopy is one of its unique features, but in correlation to the meniscus formation it can also be its Achilles heel. Moreover, the three-dimensional temperature distribution in the specimens makes it difficult to describe the actual temperature at the liquid/solid interface. Therefore, to overcome the prevailing problems Griesser [4] as well as the present work used the so-called concentric solidification technique, which will be described in more detail in the following section.

3.2.2 Concentric Solidification Technique

Reid et al. [39] designed this advanced experimental technique for HTLSCM. The concentric solidification technique is described as the formation of a centralized pool of liquid metal contained by a rim of solid of the same material under a radial thermal gradient.

The sample thickness is critical for the creation of a stable melt pool. In order to generate a beneficial thermal distribution a maximum sample thickness of < 250 µm has been established for Fe-C alloys. Additionally, a thin sample is beneficial for the formation of a vertical solid/liquid interface as shown in Figure 3–5, due to the fact that the thermal gradient approaches zero. Consequently, observations of the free surface can be attributed to events occurring in the bulk. Another benefit of the concentric geometries vertical liquid/solid interface is that the phase fractions can be accurately measured throughout the experiment.

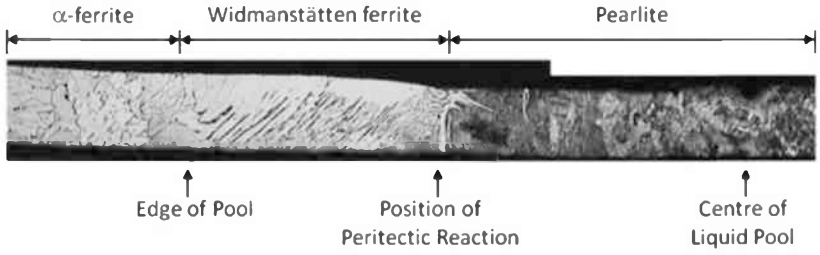

Figure 3–5: Cross-section of a solidified specimen where carbon segregation has lead to various microstructural phases along the radial solidification direction in a Fe-0.17 C alloy [39].

As stated earlier the presence of a distinct meniscus for rectangular as well as cylindrical crucibles makes it difficult to observe the peritectic transition. The surface tension energy balance between melt, solid rim, alumina crucible and gas atmosphere at concentric solidification leads to a less pronounced meniscus, resulting in a larger area that is in sharp focus. Therefore it allows an accurate measurement of the phase fractions of liquid and solid

throughout the experiment. The fraction of liquid and solid can be calculated as following, where R_P is the liquid pool radius and R_S the sample radius [39].

$$f_l = \frac{{R_P}^2}{{R_S}^2}$$

For this particular experimental setup the specimens are prepared to 9.8 mm diameter and 250 µm thickness. The structure of the specimen holder is shown in Figure 3–6. The alumina crucibles were placed in a platinum holder which was welded to a B-type thermocouple wire, guided by an alumina 2-bore tube with an outer silica support tube and a polymeric end piece.

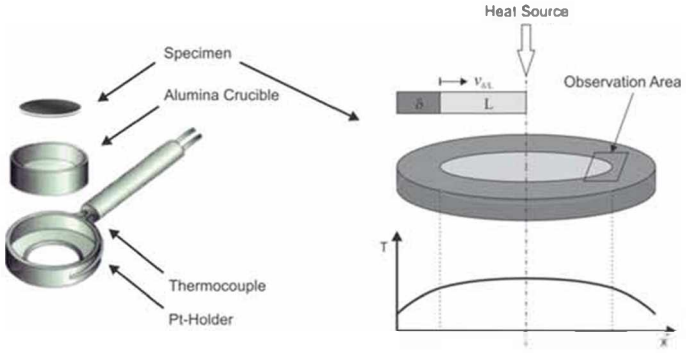

Figure 3–6: Structure of specimen holder (left) and scheme of the concentric solidification technique (right).

3.2.3 Crucible with Suspension Points

In the course of the present experiments an addition to the existing setup - the crucible with suspension points - was developed. With the conventional crucible it was not possible to investigate alloys with high manganese contents due to the large number of melting pool ruptures and consequential experiment terminations. It is supposed that this melting pool ruptures are linked to the wetting of the alumina surface and the accompanied surface distortions.

Therefore the new design aims to lift the sample of the alumina surface to avoid direct contact of the liquid pool and the crucible bottom. To achieve this three knobs of ceramic glue, which are symmetrically arranged on the bottom of the inner crucible edge, form the points of support for the specimen (see Figure 3–7). In this setup the crucible support points touch only the solid rim of the specimen. The surface tension balance for the liquid pool is reduced by the alumina and depends on the contribution of melt, solid rim and the gas phase. It might be expected that the liquid pool would start to sag because of its own weight. But the video recordings show a focused image of the melting pool and the solid rim at the same microscope elevation. As previously described the confocal microscope can only give

a fully focused image of an even surface, thus the difficulties when a meniscus is formed, which is not happing for the supported specimen. As can be seen in Figure 3–7 the subsequent visual examination confirmed the evenness of the solidified sample.

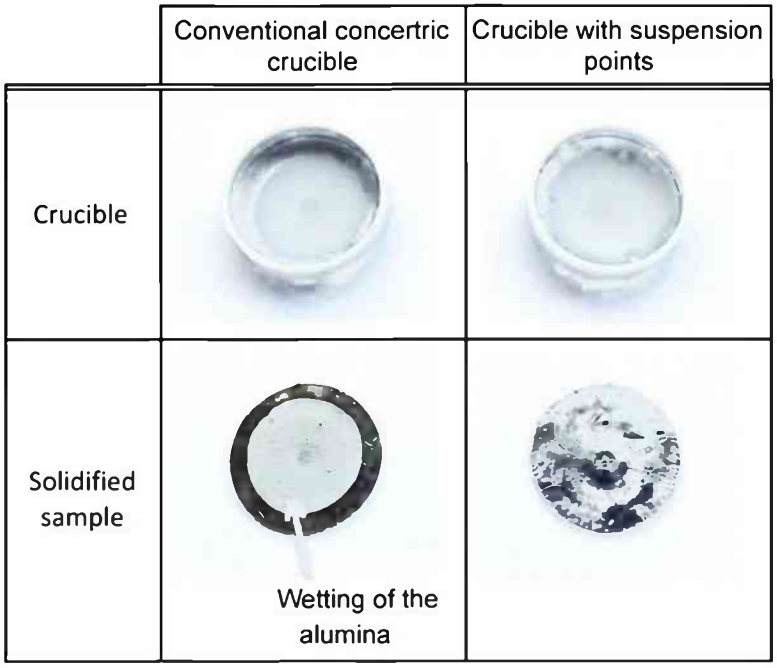

Figure 3–7: Comparision of the conventional crucible and the newly developed crucible with suspension points.

Beside the fact that the newly developed technique makes it possible to achieve a stable concentric liquid pool of alloys with more than one per cent manganese, it allows a faster melting of these alloys, which in turn reduce the amount of evaporating manganese and decarburisation.

During the development of the presented technique special care had to be taken to ensure that the size of the ceramic supporting points did not exceed the solid rim. Figure 3–8 shows how a large supporting point decentres the formation of the concentric melting pool. Additionally, the supporting points effect the heat conduction of the crucible and hence the measured temperature difference between sample and crucible holder. To guarantee constant conditions it was made sure that the position of the supporting points remained the same for all experiments.

Figure 3–8: Unevenly distributed supporting points and decentralisend melting pool .

3.2.4 Focal Point Diameter

The radiation beam of the infrared furnace largely influences the temperature profile within the sample. Therefore, Griesser [4] visualised the focal point diameter by heating a thermographic paper in the crucible. As shown in Figure 3–9 an intensity plateau with a diameter of approximately 2 mm was found in the centre of the crucible. Additionally, the interface velocity for the solidification of a Fe-0.0036 C alloy was investigated. The results showed that for liquid pool diameters smaller than 2 mm the interface velocity decreases significantly due to the increased radiation intensity and should therefore not be considered.

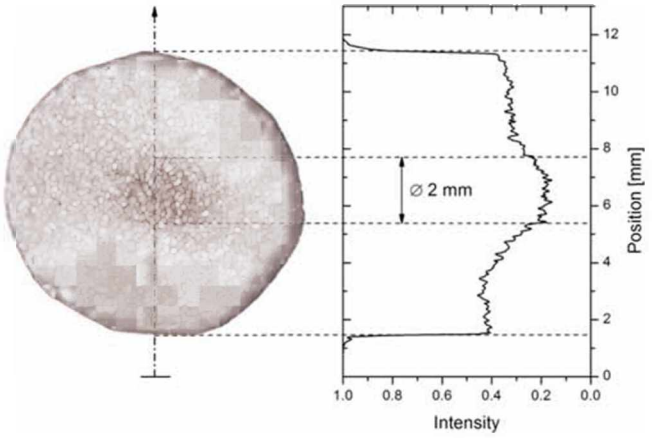

Figure 3–9: Focal point diameter measured on thermographic paper [4].

In comparison to other radiation furnaces of HTLSCM-setups the relatively small focal point diameter of the infrared furnace at the University of Wollongong leads to the formation of a steep temperature gradient, which in turn yields ideal conditions for concentric solidification and the observation of the solid/liquid interface progression.

3.2.5 Temperature Measurement

In the presented experimental design the thermocouple was spot welded to the outer edge of the sample holder, shown in Figure 3–6. The temperature response of the thermocouple was fed into the PID-controller where it regulated the power input according to the set temperature profile (see Chapter 3.3). Subsequently the data was stored on the computer for further processing. It was necessary to establish a relationship between the measured thermocouple temperature and the actual sample temperature. For experiments without the formation of a melting pool it would be possible to solder a thermocouple directly to the rim of a standardised specimen. Since the conducted concentric solidification experiments were targeted to establish a melting pool and to observe the behaviour at the or close to the liquid/solid interface, it is necessary to elaborate a relationship between the measured temperature and the prevailing interface temperature. Following section is aimed to describe the applied temperature calibration.

Due to the fact that every sample holder is slightly different, with every replacement the temperature calibration had to be repeated. For a first assessment of the temperature difference between the centre of the solid specimen and the thermocouple, the measured liquidus temperatures were compared with the theoretical liquidus temperature of the respective alloys. As can be seen in Figure 3–10 the average temperature difference for heating was 196 K. One reason for the pronounced deviations may be the influence of increased manganese contents on the thermal conductivity of the samples. A more comprehensive discussion on these findings will be given in Chapter 3.6.

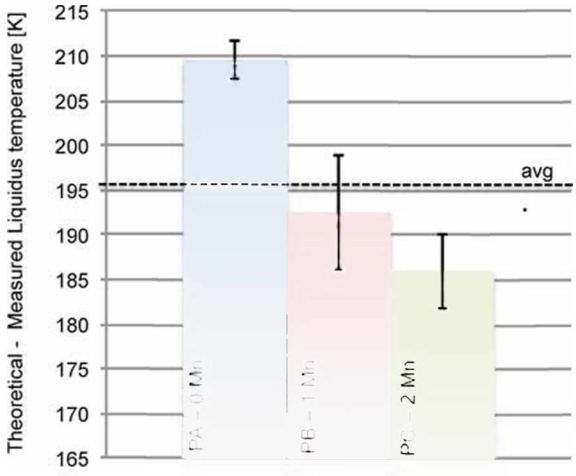

Figure 3–10: Temperature difference between the theoretical and measured liquidus temperature during heating for three different alloys.

As a result of the different thermal conductivities of liquid and solid the temperature distribution changes with the liquid pool size. Figure 3–11 shows how the temperature gradient is steeper for a smaller liquid pool due to the lower thermal conductivity and heat capacity of the solid. In the case of a large liquid pool respectively only a small remaining solid rim the temperature difference between centre and edge of the sample reaches small values, as can be seen on the left in Figure 3–11. The changing temperature gradient within the sample makes it impossible to use a temperature constant for the thermocouple calibration. Instead the Lever-rule is applied to take the changing pool size into account.

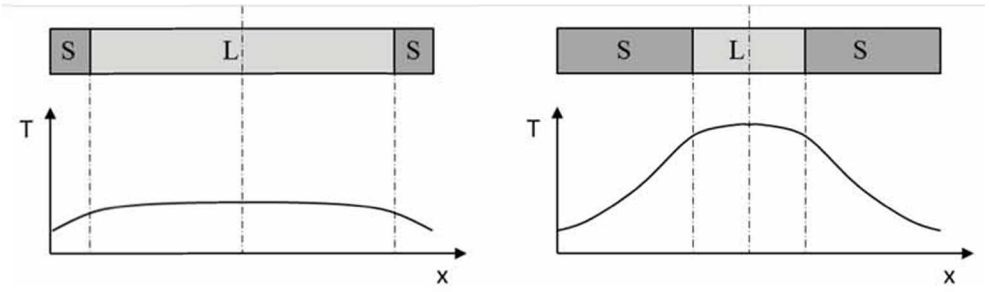

Figure 3–11: Temperature distribution for different liquid pool sizes [4].

Generally the so-called lever rule is used in a phase diagram to calculate the phase fractions for a given temperature and alloy composition. To elaborate a temperature relation for the concentric solidification method the lever rule is inverted to give the temperature. The HTLSCM expanded with the image processing software (see Chapter 3.4) provides the possibility to measure the liquid pool size over time throughout the entire experiment. Figure 3–12 illustrates how the measured liquid pool size and the consequential phase fractions together with the given alloy composition can be used to determine the prevailing interface temperature, T_{Lever}.

This method is only applicable for melting and solidification under equilibrium conditions. During initial solidification the interaction between the solute rejection due to partitioning and the solute diffusion in the solid and liquid is such that the conditions are close to equilibrium. The width of the solid rim is small enough to enable sufficient back-diffusion of carbon, so that an accurate measurement of the phase fractions can be achieved. Throughout solidification the system moves further away from equilibrium. The higher the fraction of solid the more time is required for back-diffusion, which leads to the formation of a solute concentration gradient in the solid and enrichment in the liquid phase (see Figure 2–10) [4].

$$Lever-rule: \qquad f_L = \frac{c_A - c_\delta}{c_L - c_\delta} = \frac{\emptyset_L^2}{\emptyset_S^2}$$

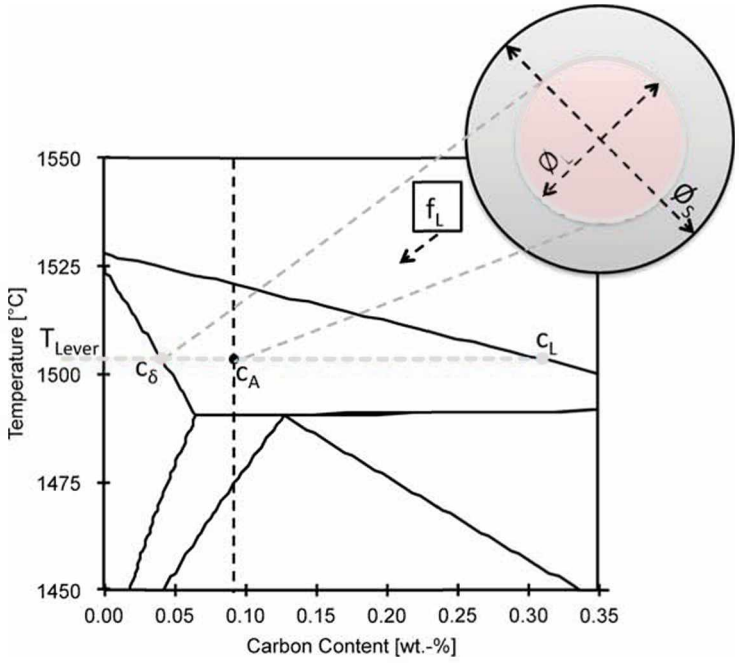

Figure 3–12: Lever rule for temperature determination

During solidification the system shifts more towards non-equilibrium conditions due to insufficient back-diffusion. The enriched liquid has a lower liquidus temperature which in turn leads to a larger liquid pool size compared to equilibrium conditions. The turning point of the temperature-time diagram is mirrored to calculate the real interface temperature. A more comprehensive explanation on the non-equilibrium temperature calibration is given in Griesser [4]. Additionally, to apply the described temperature determination it is necessary to have an accurate radius measurement system. Even small radius divergences lead to an incorrect temperature measurement (see Chapter 3.4.1). For steels with increasing alloy content it is also essential to apply the correct phase diagram data.

In the present work a cooling rates of 10 K/min was used in most of the experiments. Inevitable these experiments occurred under non-equilibrium conditions. A formation of pronounced interface perturbations made the procedure described above unfeasible. Therefore the temperatures and undercooling of the presented experiments are expressed in relation to each other. For experiments under the same thermal conditions it seems acceptable to compare the measured values and indicate them as relative figures. This is further discussed in Chapter 3.6.

The current experimental setup does not allow the variation of the absolute temperature independently from the temperature gradient. As a consequence it is not possible to apply

linear external temperature gradients and it would be vitally important to know the exact temperature distribution across the specimen. In Figure 3–13 Griesser [4] additionally clarifies that the effective cooling rate at the liquid/δ-ferrite interface differs from the applied cooling rate at the thermocouple, depending on the size of the liquid pool. The higher the fraction of solid, the more heat has to be transferred from the heat source in the center of the specimen through the solid rim in order to provide the applied cooling rate at the thermocouple near the edge of the specimen. As a result, the effective cooling rate at the liquid/δ-ferrite interface increases during solidification until the focal point radius (1 mm) is reached. An applied cooling rate of 10 K/min resulted in an effective cooling rate of 7±1.5 K/min. The variation depends on the shape of the phase diagram and therefore on the alloy composition, resulting in slightly different effective cooling rates for different alloys.

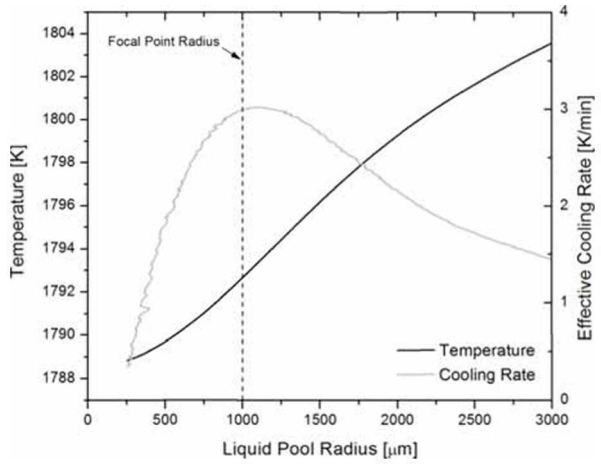

Figure 3–13: Interface temperature and effective cooling rate as a function of the liquid pool radius during solidification of a Fe-0.05C alloy with an applied cooling rate of 2 K/min [4].

In order to overcome this problem Griesser [4] proposes to locate the thermocouple in the sample holder center to measure a constant temperature difference. Furthermore, to increase the measurement accuracy a second thermocouple could be added to the existing sample holder.

3.2.6 Specimen Chamber Atmosphere

It is of great importance to maintain a neutral atmosphere inside the specimen chamber to prevent the sample from oxidation and ensure a constant alloy composition. Therefore the furnace chamber was purged with ultra-high purity argon (>99.999% Ar).

Impurities	C_xH_y	CO	CO_2	O_2	H_2	N_2
[ppm]	<0.2	<0.2	<0.5	<1	<2	<5

Table 3–1: Ultra high purity argon composition

Although the gas was of ultra high purity (composition listed in Table 3–1), a minimum quantity of impurities such as oxygen and residual moisture had to be guaranteed. For further purification the gas was directed through a titanium furnace, which worked as an oxygen getter. A resistance-heated furnace heated up a steel cylinder filled with titanium turnings to 850 °C. At this temperature titanium absorbs high quantities of oxygen and is an effective getter. The gas train consists of stainless steel tubing and Swagelok connectors. At the furnace chamber gas outlet the oxygen content was constantly measured with a Cambridge Sensotec Rapidox 2100 oxygen sensor. The titanium furnace made it possible to reach oxygen levels of 10^{-14} -10^{-18} ppm O_2. Ahead of the current experimental series to overcome existing oxidation at higher temperatures the O-ring sealing of the sample holder connection was enhanced by springs. The purpose of the springs is to compensate the thermal expansion and guarantee leakproofness over temperature changes.

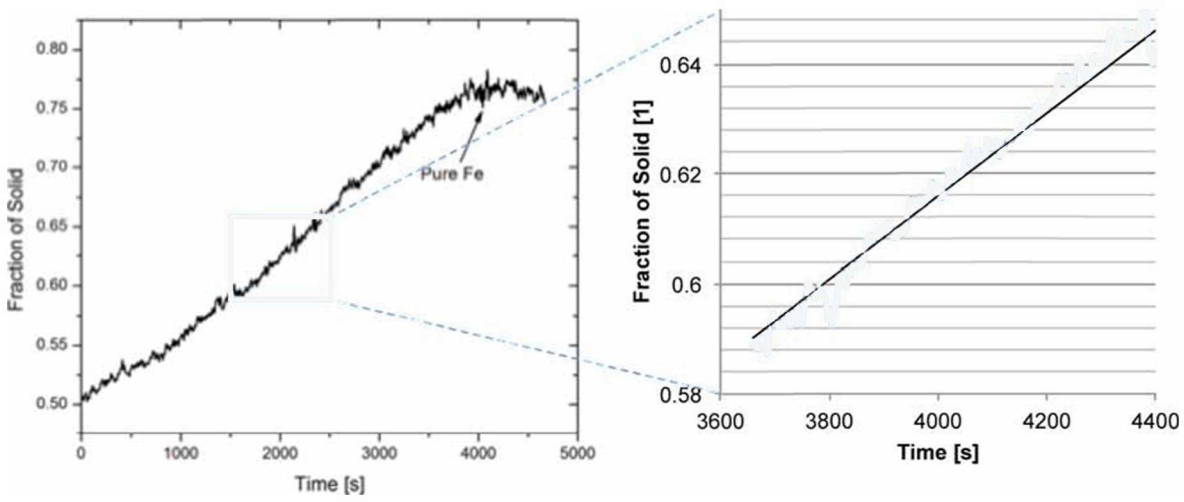

Figure 3–14: Holding experiment at constant temperature – Griesser's [4] results of fraction of solid over time (left) and present study (right).

In order to ensure comparable results with previous studies the average carbon loss at high temperatures was determined and compared with the results presented in Griesser [4]. In both studies a Fe-0.10C alloy was heated up to form a stable liquid pool with a diameter of 6 mm. The stable pool was held at a constant temperature. The remaining oxygen in the gas stream as well as evaporation at elevated temperatures resulted in a carbon loss of the liquid pool. Consequently the interface progressed slightly and the fraction of solid increased over time, as can be seen in Figure 3–14. When the entire carbon content was oxidised, the progressing of the fraction of solid halted and a stable liquid pool of pure iron remained. The average carbon loss for the Fe-0.10C was calculated to be 10^{-3} wt.-% C per minute for oxygen contents in the gas stream below 10^{-14} ppm O_2. The indicated values are only valid for the specified alloy. Since most of the experiments have been conducted with higher alloy contents the actual carbon loss is

estimated to be higher. Due to the increased rupture susceptibility of higher alloyed samples, it was necessary to increase the liquid pool size manually and slow, which resulted in total experimental time of up to 50 minutes.

3.3 Experimental Procedure

The first step for every experiment was the sample preparation. Round sample rods with a diameter of 9.8 mm were sliced to a thickness of about 250 µm utilising a Accutom-10 high-precision cut-off machine. In order to indicate the initial liquid pool diameter a calliper was used to draw a concentric circle with 6 mm diameter on one side of the sample surface. After the sample was thoroughly cleaned it was placed in the crucible and onto the sample holder. Subsequently the furnace was sealed and a Pfeiffer MVP 015-4 vacuum pump was used to generate a vacuum in the furnace chamber of 1.2 mbar. The chamber was flushed with the ultra-high purity argon purified by the titanium furnace. Alternating the application of vacuum and gas flushing for seven times lead to a neutral atmosphere in the furnace chamber with a final partial pressure of about 10^{-14}-10^{-18} ppm O_2. The oxygen content was constantly tracked with the software package supplied by rapidox.

The intended heating-curve was manually programmed in the PID-controller. At first a preheating step at 150 °C for several minutes guaranteed that remaining moisture or hydrocarbons associated with the cleaning of the infrared heating furnace were removed. In the next step the sample was heated to a temperature of 20-30 °C below the melting point at a rate of 100 K/min. Then a heating rate of 5 K/min was applied to ensure a controlled melting pool formation in the centre of the specimen. At the desired liquid pool radius the temperature was held for several minutes to form an equilibrium concentration profile across the specimen. Next the specimen was solidified at a predefined cooling rate. After the peritectic transition occurred the sample was cooled down to room temperature at a rate of 100 K/min.

During every experiment the thermocouple temperature, the oxygen content as well as the recorded video data was stored on the measuring computer. Following section describes in more detail the analysis of the obtained data.

3.4 Data Analysis

During each performed experiment a video at a rate of 30 frames per second was recoded using the software "Video Debugging". Employing a super-imposing unit the measured thermocouple temperature was displayed on the video stream. Additionally, the video image included a micrometre scale bar matching the respective magnification and the proceeding experimental time. Simultaneously the atmospheres oxygen content was logged employing the software "Rapidox Data Logger". In order to guaranty traceability and replicabilty the sample diameter and thickness as well as the respective crucible were documented.

To reduce the time and resources associated with the manual investigation of video files with thousands of frames Griesser et al. [42] has developed "SolTrack" an automatic video processing software. SolTrack is aimed to measure the growth velocities of propagating interfaces in in-situ high-temperature laser-scanning confocal microscopy. The software is using the commercial software package "MATLAB". To reduce computer performance and to not overcharge the workspace SolTrack is designed as a frame-by-frame analysis of a video file. The interface tracking technique detects the first change in the pixel colour intensity along a user defined tacking path (Figure 3–15), by tracing the peak in the gradient intensity profile. Additionally, SolTrack features the possibility to determine the liquid pool radius. Finally the results of this analysis are the interface position and radius over time and measured temperature, which can be used to calculate the phase fraction of solid and liquid. Further details to SolTrack's functionality are given in [42].

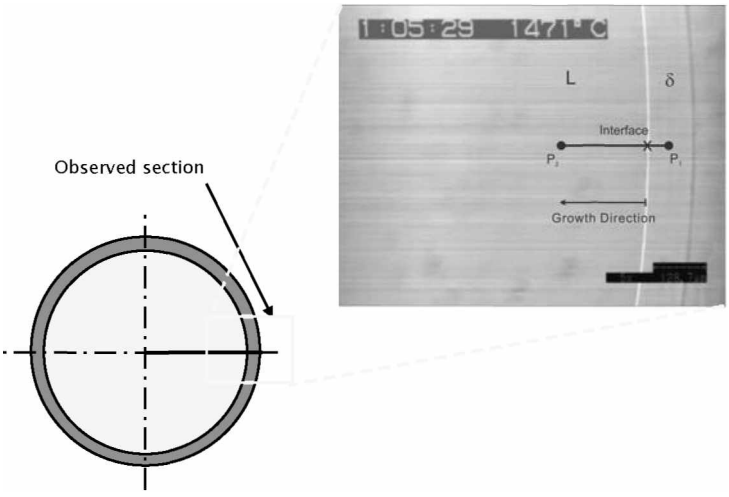

Figure 3–15: Interface detection along a user-defined tracking path on a concentric solidification experiment.

3.4.1 Interface Tracking and Radius Detection – Manual vs. SolTrack

In his paper Griesser et al. [42] has clearly shown the functionality of SolTrack with its ability to analyse different shapes and features in various materials. However, in the course of this analysis the radius detection and interface tracking tool of SolTrack failed to give accurate results and had to be verified manually in following cases:

- Very uneven interface propagation
- Video section not in the right sample corner
- Slightly oval liquid pool

The stated cases do not occur for low-carbon low-alloyed steels but can appear especially for alloys with increased manganese contents. In order to validate the radius determination methods a comprehensive comparison was undertaken.

Whenever the radius detection tool could not give sufficient results, the initial and final radius had to be evaluated manually. Therefore a number of frames along the melting pool axis were stitched together utilising the commercial software "Microsoft PowerPoint". Figure 3–16 depicts the final puzzle of stitched pictures of the sample surface after solidification. After the specimen centre was marked with a circle the initial and final respectively massive diameter were measured with the scale bar. By adding a large number of pictures this procedure was also used to track the interface movement over time. This procedure was used to verify the accuracy of the automatic tracking tool of SolTrack. Figure 3–17 compares the manually and automatically measured interface progression of a 2 wt-% Mn alloy. It can be clearly seen that as soon as the smooth interface gets distorted, the manual and automatic measurements begin to diverge from each other. This results in a final variance of eight per cent based on the interface movement, which leads to a divergence of 1.5 % for the fraction of liquid.

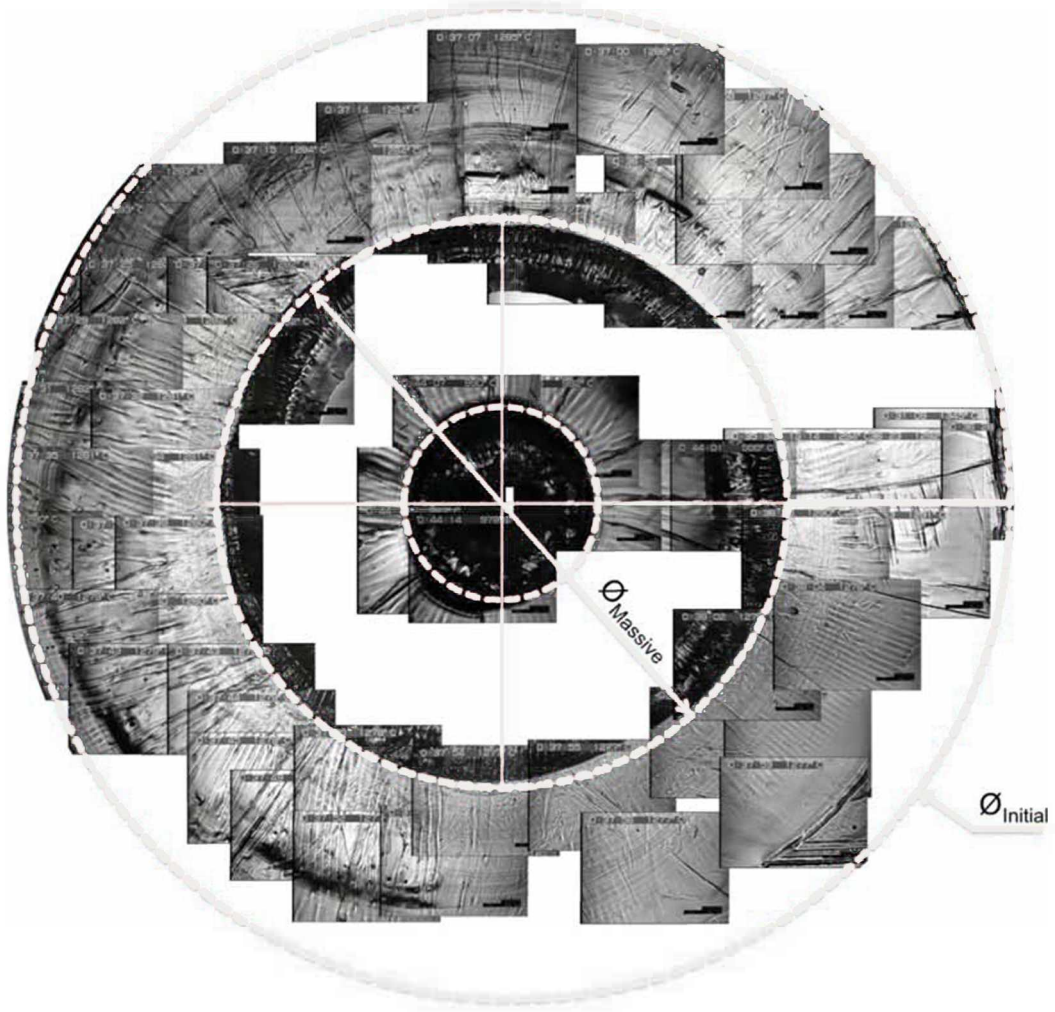

Figure 3–16: Stitched picture of the sample surface after solidification.

Arguably the systematic error of the manual technique largely depends on the operator's accuracy. To minimise this error a second operator repeated the stitching. In conclusion, the automated video processing software represents a improvement over the manual interface tracking in terms of efficiency. However, the presented considerations regarding Figure 3–17 show the necessity to validate the automatic tracking tool for above-mentioned cases.

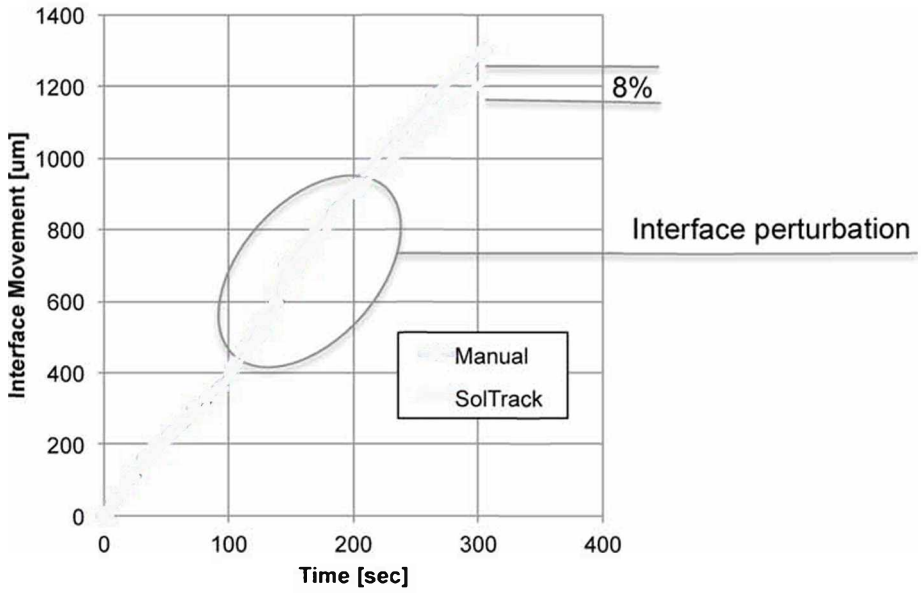

Figure 3–17: Comparison of the manual and automatic tracking methods on the basis of the interface progression of a 2 wt-% Mn alloy.

3.4.2 Reproducibility

In order to acquire sound investigational results it is most important to ensure reproducibility of experimental observations. This is only possible by maintaining constant experimental conditions. The present chapter describes the influence of the experimental parameters and the validating investigations that have been undertaken throughout the experiments.

Experimental experience has shown that larger initial pool radii result in a state closer to equilibrium but increase the decarburisation and evaporation of alloy components, additionally the rupture susceptibility increases. The same applies for extended experimental times, especially the heating-up time and the initial oxygen contents. The flow rate of the argon gas stream affects the thermal conditions in the furnace chamber and was hence held constant. For the newly developed crucible design with ceramic points of support, the spatial orientation of these points influences the heat transport within the crucible.

Figure 3–19 shows how the diversion of one experimental parameter in this case the extended time to form the initial liquid pool, can crucially influence the result. The diagram illustrates an increased interface progression for the extended pool formation time due to carbon and alloy element loss. This clearly shows that constant conditions have to be sustained through an entire experimental series.

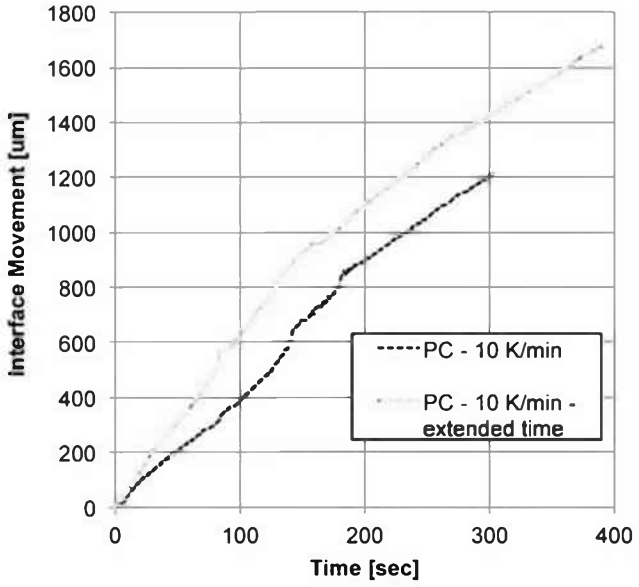

Figure 3–18: Interface propagation over time for different experimental conditions.

Only by maintaining the above-mentioned conditions the experiments give reproducible results, which can be compared with other experimental results. Figure 3–19 depicts the interface progression of three identical experiments of a Fe-1 wt.-% Mn alloy cooled with an applied cooling rate of 10 K/min. The consistent results presented in Figure 3–19 are the counterpart to Figure 3–18. All of the presented experiments were carefully repeated to ensure accuracy.

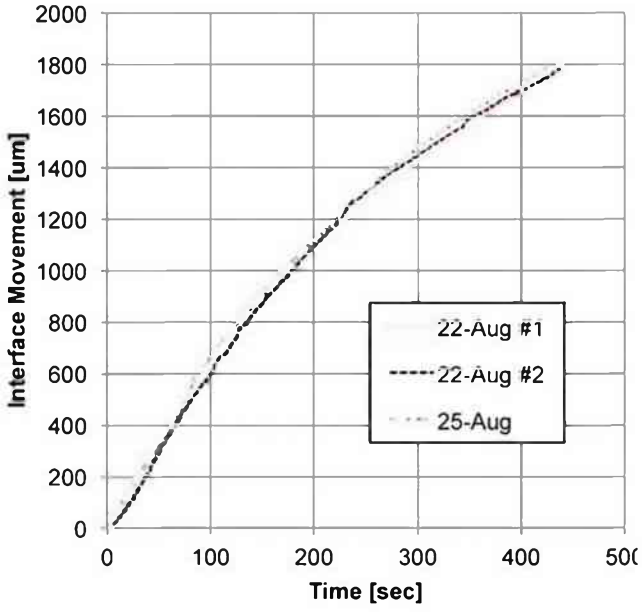

Figure 3–19: Reproducibility experiments of a Fe-1% Mn alloy.

3.5 HTLSCM - Experiments

A detailed understanding of the microscopic events is of great interest to master the industrial continuous casting process. The development of high-temperature laser-scanning confocal microscopy, as described in the previous chapters, laid the foundation for in-situ observations of the solidifying shell. Observing the progression of the liquid/δ-ferrite interface enables to draw conclusions on the thickness and morphology of the solidifying shell in the meniscus region of a continuous caster. As already described in Chapter 2.3 the experiments have been designed to clarify the influence of manganese on the peritectic transition. Specifically the solidification behaviour regarding the relative position to C_A and C_B along the peritectic line and the intensity of the massive transformation were focus of the performed investigations. The following chapter presents the observations of the HTLSCM experiments conducted at the University of Wollongong.

In order to maintain constant conditions the initial setup was prepared as described in Chapter 3.3. The specimen was heated up to a temperature within the liquid/ δ-ferrite two-phase region to form a liquid pool with a 6 mm diameter. Note that the amount of primary solidified δ-ferrite varies due to the differently shaped phase diagrams. However, the described approach is reasonable because it ensures similar diffusional conditions due to areal similarity within the samples. To enable a stable liquid pool formation of rupture-susceptible alloys, e.g. alloys containing high Mn-contents, the heating rate and holding periods were individually adjusted. Unless specified differently a cooling rate of 10 K/min was applied.

To compare the obtained results with other researchers results and to resemble industrial conditions most of the experiments were performed under non-equilibrium conditions. The interface propagation results in the development of more or less steep solute concentration gradients in the phases during primary solidification. When the peritectic temperature is reached, γ-austenite nucleation is hampered in the direct vicinity of these gradients. The temperature drops below the equilibrium peritectic temperature, to increase the thermodynamic driving force (see Chapter 2.2) and the transition occurs therefore under non-equilibrium conditions.

3.5.1 Investigations of Different Alloy Compositions

Three iron-carbon-manganese alloys with different alloy contents were investigated to clarify how the relative position along the peritectic line of the alloy compositions influences the kinetics and morphology of the peritectic phase transition. Table 3–2 summarizes the

chemical compositions of the investigated alloys. As can be seen in Figure 3–20, PA-0% Mn and PC-2% Mn are hyper-peritectic alloys whereas PB-1% Mn is a hypo-peritectic alloy.

Table 3–2: Chemical Composition of investigated alloys (all values in wt.-%).

Alloy	C	Mn	Si	P	S	Ti	Cr	V
PA-0% Mn	**0.18**	**<0.01**	0.005	0.002	0.002	0.003	0.002	0.003
PB-1% Mn	**0.14**	**0.94**	0.025	0.003	0.006	0.003	0.003	0.003
PC-2% Mn	**0.16**	**1.93**	0.01	0.003	0.006	0.003	0.004	0.003

The left side of Figure 3–20 illustrates the peritectic region of the respective iron-carbon phase diagram of the investigated alloys. The thermodynamic data were computed with the software Thermo-Calc [29] based on the database TCFe6 steels/felloys. According to Presoly [43] this data is in good agreement with his CALPAD validation. The diagrams were calculated considering the alloying elements stated in Table 3–2. Manganese and sulphur show the biggest influence on the shifting equilibrium. Due to the fact that manganese is an austenite-stabilising element, the peritectic region is reduced in size and simultaneously shifts the peritectic point to lower temperatures and concentrations. In addition the initial fraction of liquid for 6 mm pool diameter is marked with a dot for each alloy respectively.

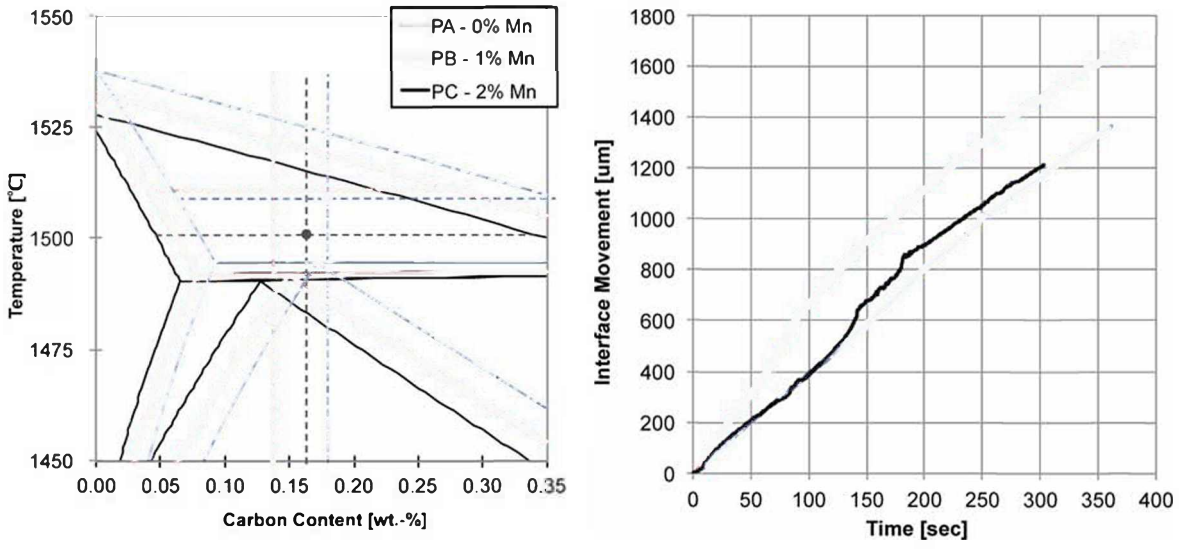

Figure 3–20: Binary iron-carbon phase diagram (left) and the interface progression over time (right) of the investigated alloys.

On the right of Figure 3–20 the migration distance of the liquid/δ-ferrite interface is plotted over time until the peritectic transition occurred. The interface of PB-1% Mn migrated 1700 µm and showed the fastest initial velocity. PA-0% Mn and PC-2% Mn exhibited a

similar initial progression. After about 600 µm the liquid/δ-ferrite interface of PC-2% Mn formed perturbations presumably due to manganese segregation. Consequently the interface migration graph of PC-2% Mn diverged from PB-1% Mn and the peritectic transition occurred earlier. Table 3–3 lists the relative position according to C_B to the particular equilibrium phase diagram of the different alloys, as can be seen in Figure 3–20. Additionally, the relative undercooling below the particular equilibrium peritectic temperature with reference to PC-2% Mn are given. The relative undercooling is calculated using the difference of initial and peritectic temperature according to the equilibrium phase diagramm as well as the difference of initial and transformation temperature according to the thermocouple. The received values are summed and expressed with respect to the lowest undercooling i.e. PC-2% Mn. Note that the undercooling was less pronounced for alloy compositions to the right of C_B. Also PB-1% Mn showed the longest migration distance and had hence the largest fraction of primary δ-ferrite prior to the transformation.

Table 3–3: Relative alloy position according to C_B in the particular binary phase diagram and relative undercooling with reference to PC – 2% Mn.

Sample	Position relative according to C_B [%C]	Relative Undercooling
PC – 2% Mn	+0.35	-
PA – 0% Mn	+ 0.1	6
PB – 1% Mn	-0.2	11

Figure 3–21 depicts a sequence of the massive peritectic transformation for PB-1% Mn and PC-2% Mn alloys. The initial separation of primary δ-ferrite and liquid, known as the peritectic reaction occurred in less than 1/30 of second and can hence not be illustrated step-by-step with the available frame rate. During the massive transformation the γ-austenite propagated rapidly into the primary formed δ-ferrite. With reference to the relative undercooling (see Table 3–3), as might be expected the alloy PB-1% Mn transformed faster. After 3/30 of a second almost the entire observation area was transformed for the PB-1% Mn alloy. Note that both alloys exhibited massive transformation and that the transition of PB-1% Mn is regarded as more massive. The transformation speed of PA-0% Mn was somewhere in between PC-2% Mn and PB-1% Mn.

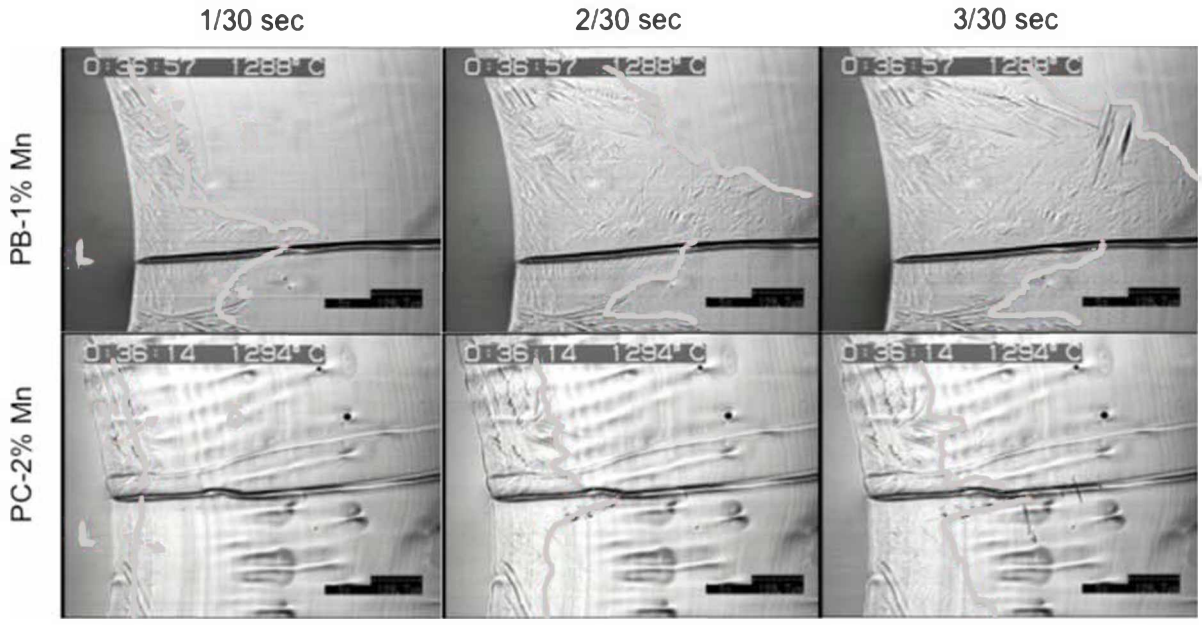

Figure 3–21: Sequence of the massive transformation for the alloys PB-1% Mn and PC-2% Mn.

3.5.2 Influence of the Cooling Rate

In order to verify the influence of the cooling rate on the peritectic transition for alloys with increased manganese contents, the alloy PC-2% Mn was solidified with applied cooling rates of 2 K/min and 10 K/min. Higher cooling rates than 10 K/min cause a higher undercooling below the equilibrium peritectic temperature, which in turn increase the progression of the massive transition to the extent that it exceeds the frame rate of the recording video software.

In Figure 3–22 the interface migration is plotted as a function of time of the alloy PC-2% Mn for the applied cooling rates respectively. Both curves are drawn until the peritectic transition occurred. In similar manner to the other investigations both experiments were started with the same initial pool size of 6 mm to guarantee equilibrium concentration profiles prior to solidification. The two alloys exhibited almost identical migration distances but as expected for a cooling rate of 2 K/min the interface propagation occurred at a slower velocity. Both experiments showed interface perturbations due to manganese segregation.

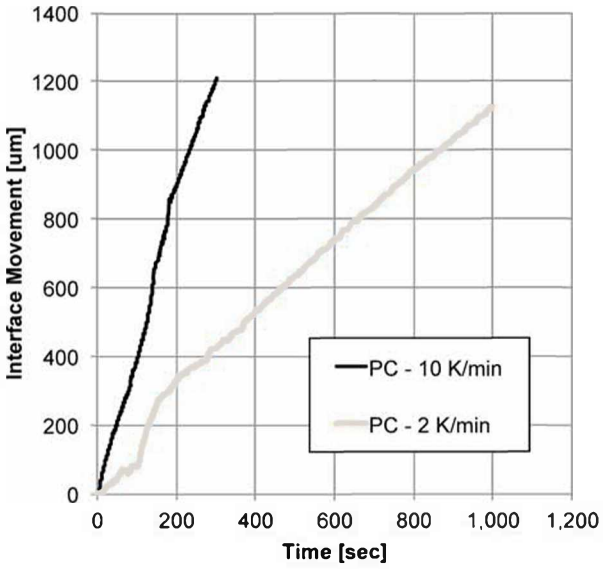

Figure 3–22: Interface migration over time for different cooling rates of the alloy PC-2% Mn.

A faster cooling rate resulted in a steeper concentration gradient ahead of the solidifying interface, which in turn hampered the γ-austenite nucleation and lead to an increased relative undercooling of 18 K. Figure 3–23 depicts the peritectic transformation of the alloy PC-2% Mn for a cooling rate of 2 K/min at one second after the beginning of the peritectic transition and for 10 K/min after 1/10 of a second. The fast cooling rate results in the expected massive transformation with the associated fast γ-austenite progression, whereas the lower cooling rate exhibited a planar-type of transformation. Even for the lower cooling rate 2 K/min the progression of the peritectic reaction took place in less than 1/30 of a second and could not be captured with the recording software. The presented experimental results are discussed in the following chapter.

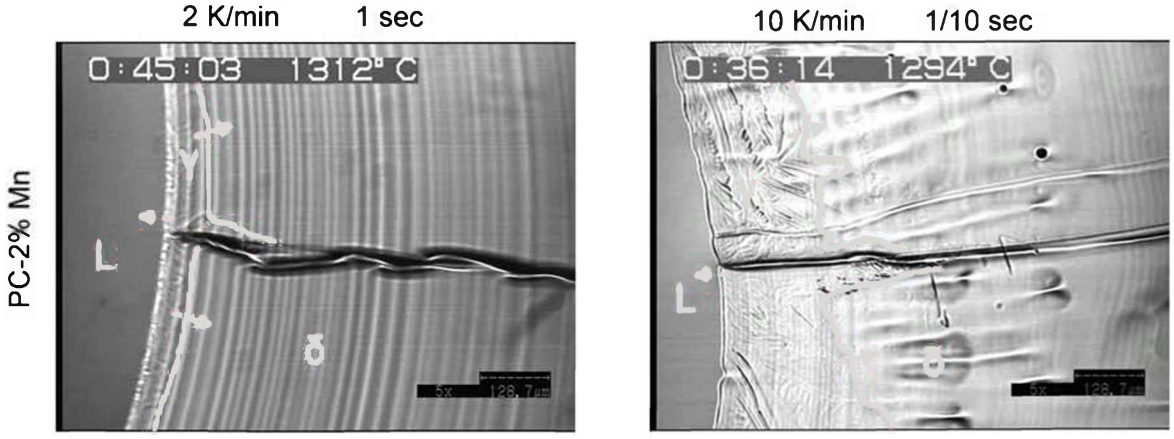

Figure 3–23: Peritectic transformation of the alloy PC-2% Mn with an applied cooling rate of 2 K/min and 10 K/min.

3.6 Discussion

This section discusses the observations presented in the previous chapters and examines the applied experimental procedure. The HTLSCM-investigations comprised alloys with a manganese content of up to 2 wt.-% manganese. The experiments aimed to clarify the influence of higher manganese contents on the undercooling below the equilibrium peritectic temperature and the intensity of the massive transformation of the peritectic transition.

The results presented in Chapter 3.5.1 point out the fact that the relative position regarding the point C_B is of great importance for the solidification behaviour of peritectic steels. The composition of the alloy PB-1% Mn was left of C_B, which involved a larger amount of primary δ-ferrite. Therefore PB-1% Mn showed a longer migration distance, an increased undercooling and a more massive transformation compared to PA-0% Mn and PC-2% Mn. The results seem to confirm Griesser's experimental observations [4] of a strong relation between the primary solidified δ-ferrite, the consequential steep concentration gradient and the resulting undercooling. Another important observation was that the increased manganese content did not significantly influence the kinetics and morphology of the massive transformation. Additionally, the in-situ observations of alloys with increased manganese contents, namely alloy PB-1% Mn and PC-2% Mn, displayed the development of a distorted solid/liquid interface due to segregation.

In similar vein, Chapter 3.5.2 confirmed the experience that lower cooling rates lead to a planar-like transformation morphology. It was shown that pronounced segregation even occured for a cooling rate of 2 K/min leading to similar perturbations than for a faster cooling rate. Nevertheless, the selected model alloys failed to give a clear answer on the first question (see Chapter 2.3) about the influence of manganese on the peritectic transition. However the results added impetus to conduct further experiments, namely dipping tests.

The temperature calibration for non-equilibrium conditions presented in Chapter 3.2.5 respectively in Griesser [4] is based on the determination of the turning point in the temperature-time diagram. In order to calculate the real interface temperature the measured values are mirrored along the tangent through the turning point. However, a temperature-time diagram only shows a distinct turning point for experiments with large enough initial pool sizes. Figure 3–24 illustrates the calibration method for two exemplary alloys. Note that the depicted turning point of PA-0% Mn is calculated utilising a polymeric approximation and results in a 2.5 K lower temperature for the peritectic transition. The graph of PC-2% Mn shows a pronounced coarseness due to interface perturbations during solidification. Therefore the determination of a discrete function and consequential a turning point is not possible. Additionally, the perturbations hampered the exact phase fraction

measurement. The presented experiments were conducted with an initial pool diameter of 6 mm, which corresponds to a solid fraction of 62.5 %. A liquid pool diameter of more than 7 mm would favour the formation of an initial equilibrium and result in a more distinct turning point. Samples with increased alloy compositions were prone to liquid pool ruptures and it was not possible to establish larger pools than 6 mm diameter. Therefore the temperatures and undercooling of in the present study are expressed as relative values with reference to each other.

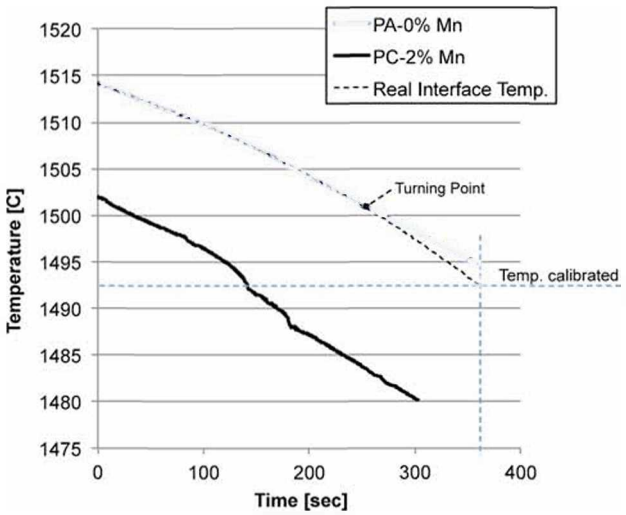

Figure 3–24: Temperature calibration for non-equilibrium conditions.

Although the oxygen content of the argon atmosphere is relatively low (10^{-14}-10^{18} ppm O_2), the decarburisation throughout an experiment is considerably to high and has to be taken into account. As shown in Chapter 3.2.6 the carbon loss was calculated to be 10^3 wt.-% C per minute for a Fe-0.10C alloy. In the case of higher alloy concentrations this rate was much higher, presumably caused by the additional evaporation of alloying elements. Not quantifiable evidence presented the increased furnace chamber pollution of alloys with higher alloy compositions. In most cases the concentration loss was not substantial enough to cause a changed solidification mode. But it resulted in considerable deviation of the phase fractions, which in consequence lead to the false interfacial temperatures respectively an inaccurate calculation of the undercooling.

For future experiment of steels with higher alloying composition the presented experimental technique needs to be improved considering the following parameters: the evaporation of alloying elements, the insufficient temperature measurement and the rupture susceptibility of the liquid pool.

4 Dipping Test

Much work has been done to explain the carbon content dependence of the uneven solidification in steels within the peritectic range. In an attempt to analyse the solidification behaviour on an experimental scale with close relation to the industrial process, many researchers have performed a variety of so-called "dipping tests", where differently shaped specimens are dipped into liquid steel to consequently examine the solidified shell.

In contrast to the microscopic events observed with confocal microscopy, dipping tests are aimed to investigate the macroscopic solidification behaviour of steel. In the present study the objective of the dipping experiments was to clarify the preceding HTLSCM findings. For this matter the dipping tests were used not only to investigate the influence of carbon but also other alloying elements such as manganese and silicon. The dipping test setup provides a simple and at the same time statistically meaningful method to analyse the solidification behaviour of steels. Following chapters cover the various steps of the development of the dipping technique up to the data analysis of the performed experiments.

4.1 Dipping Techniques

Murakami et al. [44], Suzuki et al. [45] as well as Yamaguchi et al. [46] used the same experimental apparatus where a water-cooled cooper plate immerses into molten steel as shown in Figure 4–1 (a). Subsequently the shell unevenness was quantified under various aspects including the dipping time and heat transfer rates. The shell deformations are linked to stresses caused by solidification shrinkage and δ-ferrite to γ-austenite transformation. The authors investigated the characteristics of these depressions as a function of the carbon

content as shown in Figure 4–1 (b). Their results emphasis the tendency of uneven shell growth for hypo-peritectic steels. Additionally, Suzuki et al. [45] calculated the stress index and linked it to their experimental observations.

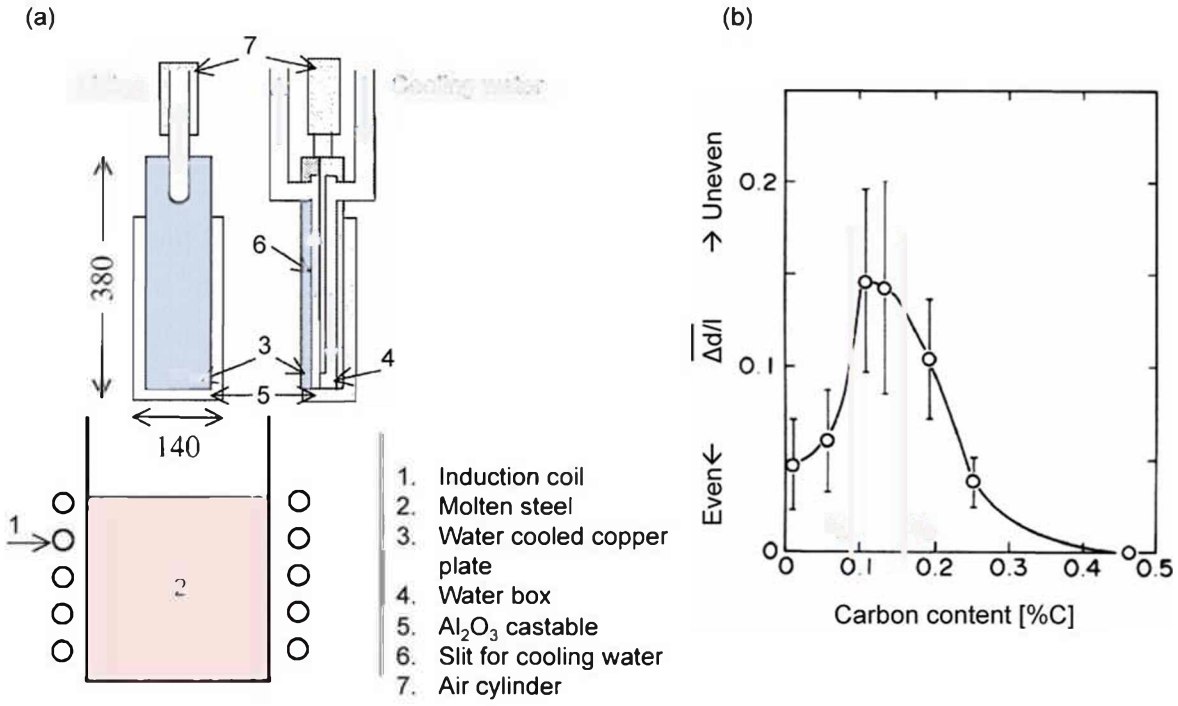

Figure 4–1: Schematic view of experimental apparatus for dipping tests (a) and influence of carbon content on the unevenness index (b) [45].

The presented experiments follow a variety of dipping tests performed at the Institute of Ferrous Metallurgy, University of Leoben, headed by Professor Bernhard. Among these Fuchs [47] examined in her bachelor thesis the influence of different casting powders on the solidification behaviour of the steel shell and initially solidified casting powder layer. Additionally, Moon [9] studied selected industrial alloys classified as low-carbon, hypo- and hyper-peritectic steels and had a closer look on different surface textures of the dipping specimen.

Based on the considerations made in literature, this work presents a dipping test method using uncooled steel rods to investigate the influence of manganese and silicon on the solidification behaviour of peritectic steels and the associated unevenness. The presented experimental setup avoids the use of water in close proximity to molten steel and is hence a safe dipping method. In contrast to Moon's setup [9] where the specimen were dipped manually, the present experiment used the SSCT-apparatus [30] with a hydraulic control to guarantee constant dipping conditions. Especially due to the application of three redundant

submerged specimens the technique gives results with a high statistical accuracy. Following sections describe the experimental setup in more detail.

4.2 Experimental Setup and Procedure

The dipping tests of the present study were performed in the laboratory of the Institute of Ferrous Metallurgy, University of Leoben. In Figure 4–2 the experimental setup of the performed dipping tests is illustrated. A Inductotherm induction furnace with an approximate melting volume of 20 kg was used to prepare the liquid steel with the respective alloy. In order to minimise the random error and to increase the statistical accuracy, three specimens evenly arranged in a circle were dipped at the same time into the liquid bath with the reutilised SSCT-apparatus [30]. Additionally, the SSCT-apparatus provided controlled dipping conditions in terms of dipping speed and specimen positioning. As shown in Figure 4–2, following the formation of a thin shell the specimens were cooled in air. Subsequently the specimen were sectioned and analysed, which is discussed in Chapter 4.3.

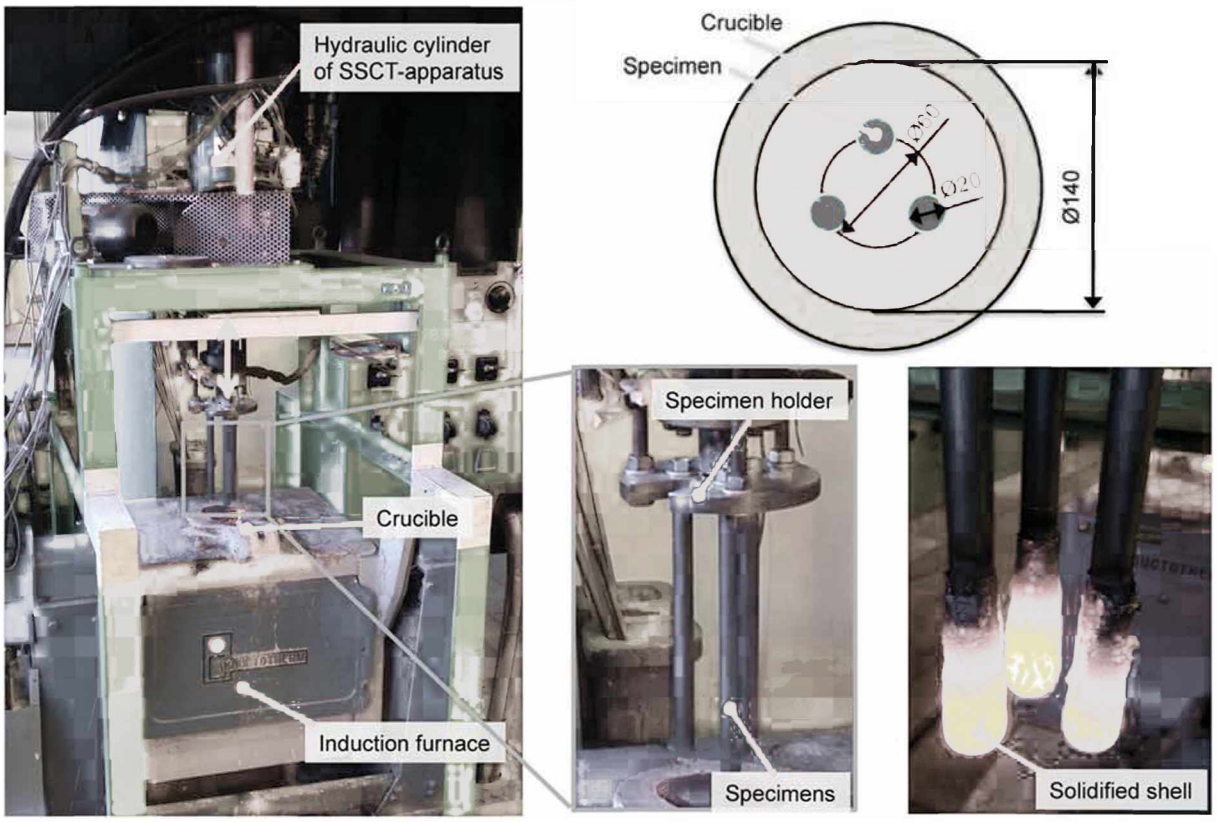

Figure 4–2: Experimental dipping test setup including a schematic cross section through the melting crucible and exemplary solidified shells.

4.2.1 Specimen Preparation

The dipping specimens were prepared of S355JR non-alloy steel. Raw material rods with a diameter of 20 mm were cut into specimens with a fixed length of 300 mm using a FORTE band saw. A conventional lathe was used to thread cut the specimens on one end for subsequent mounting on the holder, as can be seen in Figure 4–2.

Preliminary tests showed that a sand blasted specimen surface had no effect on the solidification. Thus the present experiments were performed with untreated, blank specimens depicted in Figure 4–4. The burr on the specimen tip had to be removed. In order to clean off manufacturing contaminants the specimen surface was thoroughly scrubbed with ethanol. The dipping depth of 100 mm was marked on the specimen and they were mounted on the SSCT-apparatus, where the base-plate was converted to receive the screw thread.

4.2.2 Alloy Adjustment

The task of the furnace operator was to establish liquid steel with the respective composition according to the targeted alloy specification. Pure iron bars (initial weight approx. 20 kg) were preheated and then melted, forming a liquid pool in the induction furnace. Different alloy surcharges, such as pure manganese ferrosilicon and carbon granules, were then added to adjust the respective chemical composition. In order to deoxidize the molten steel aluminum was added, maintaining an aluminum composition of about 300 ppm in the melt.

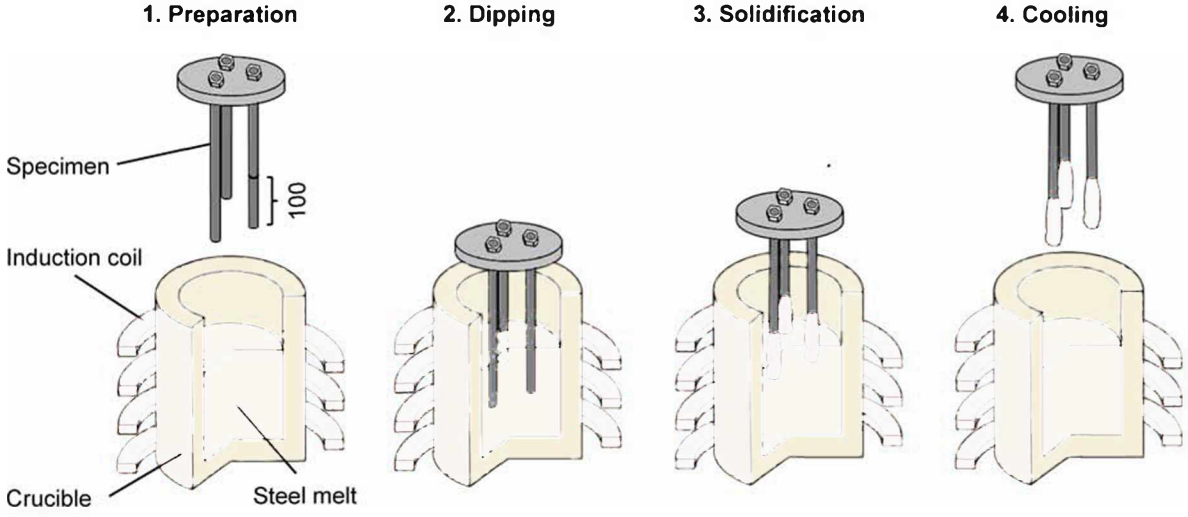

Figure 4–3: Schematic dipping test procedure.

Ahead of the dipping several so-called "lollypop" samples were taken and analysed using a spark spectrometer to measure the prevailing alloy composition. After the specified alloy composition was set, the surface of the melt was cleaned with a steel scoop and the

temperature was measured twice with a disposable thermocouple. In order to maintain low oxygen levels during the dipping a small extra amount of aluminum was added. The surface slag had to be removed again. Manoeuvring the SSCT-apparatus over the induction furnace completed the preparation. Figure 4–3 schematically illustrates the experimental procedure of the dipping test.

Next, the specimens were dipped into the melt at a constant speed of 20 mm per second. As soon as a depth of 100 mm was reached the specimens where pulled out with the same speed resulting in a total dipping time of 10 seconds. A thin shell of the particular alloy solidified on the specimen. Hence the shell growth can be calculated using the formula in Chapter 4.3.1. Instantly after the dipping another lollypop-sample was taken to verify the actual melt composition at the moment of dipping. The dipped specimens were cooled in air on the SSCT-apparatus. After 2-3 dipping cycles a 3 kg pure iron block was added to account for melt loss.

Figure 4–4: Band saw and specimen fixation to cut the solidified shell.

In order to analyse the surface unevenness of the solidified shell the specimen were cut along the cylinder axis using a band-saw, as shown in Figure 4–4. Cutting the sample along two lines into four quarters increased the statistic accuracy. Since three specimen were dipped at the same time, ideally each alloy composition is represented by twelve contours. Especially for alloy compositions with low silicon contents the formation of a crumbly slag lead to deposits on the outer specimen shell. The first attempt to avoid the analysis of these slag deposits was to cut along slag-free contours. In the case that a final contour was

contaminated with slag, the respective data had to be removed manually (see Chapter 4.3.3).

In alloys with low silicon contents and more than 3 wt.-% manganese the formation of a crumbly slag not only lead to specimen slag-contamination but also involved slag incrustation of the melting pool surface. Figure 4–5 displays severe slag incrustation for a 3.5 wt.-% Mn alloy. In this situation the experiment had to be stopped. The incrusted crucible had to be cleaned before new experiments could be performed. With a view to avoid such situations, a synthetic calcium-aluminate-slag (ISOMAG AKS02) was used for experiments with more than 3 wt.-% Mn. In the following chapter a detailed description of the data analysis is given.

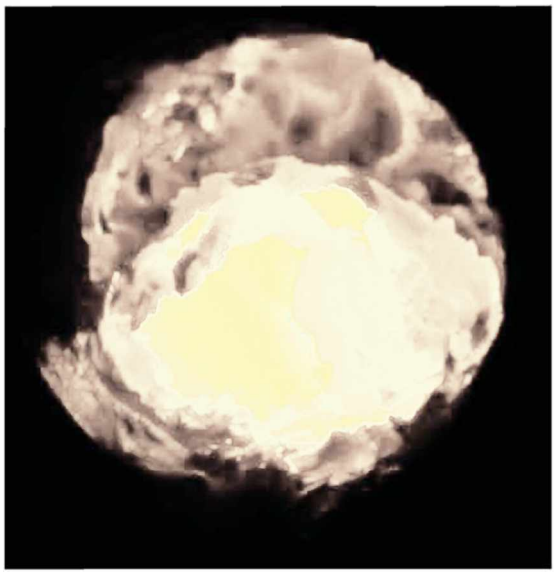

Figure 4–5: Slag incrustation of the crucible for 3.5 wt.-% manganese.

4.3 Data Analysis and Methodology

The first step to quantify the experimental obtained result was to scan the specimen quarters utilizing a conventional photocopier with a resolution of 600 dpi. In a preceding visual examination specimen contours with severe slag contamination were excluded. The commercial microscopy software CLEMEX Vision 3.5 was used to convert the contour images into numeric values. The software returns a numeric thickness with a spacing of about 0.1 mm in between two data points. Figure 4–6 depicts the scanned image of the cut specimen shell of alloy A3-0.08%C 1%Mn and the corresponding thickness values along the analysed specimen length. In order to take account for the influence of the specimen edge, such as varying flow conditions and slag entrapment, a section of 1 cm from the tip was not analysed. From there 8 cm were taken into account, excluding the last centimeter from the analysis. The obtained numeric values were further processed in the commercial software Microsoft Excel to mathematically determine the unevenness of the solidified shell.

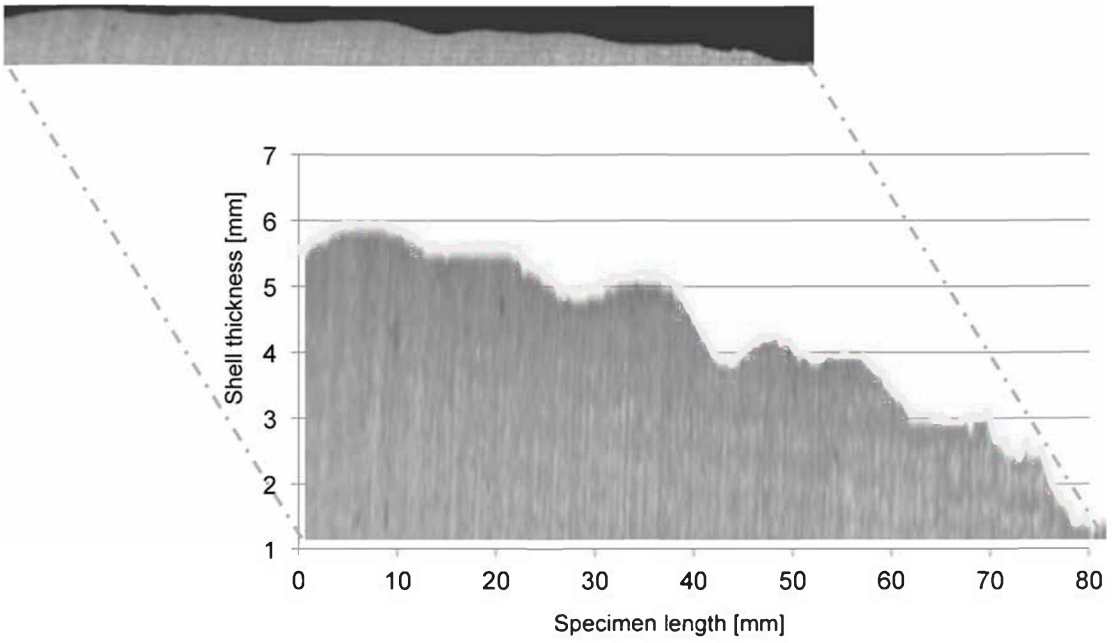

Figure 4–6: Scanned solidified shell quarter and the corresponding contour thickness data exemplary for alloy A3-0.08%C 1%Mn.

In order to quantify the average surface roughness of the solidified shell a so-called "unevenness-parameter" had to be defined. In literature a variety of different parameter definitions exist. The subsequent chapter describe the verification of the different calculation methods for the present experiments.

4.3.1 Verification and Selection of the Unevenness Parameter

This section compares two different approaches to calculate the unevenness parameter, firstly *the mean slope of profile* and secondly *the variation coefficient*. Both parameters are used in literature and their use for the present experiments is verified in the following. Furthermore, the preceding experimental data processing for each method is addressed in detail.

As indicated above Murakami et al. [44, 48] and Suzuki et al. [45] used similar experimental procedures and both applied the same evaluation method. They calculated the *mean slope* of the uneven solidified shell profile, as shown in Figure 4–7. Following formula was used to determine unevenness parameter:

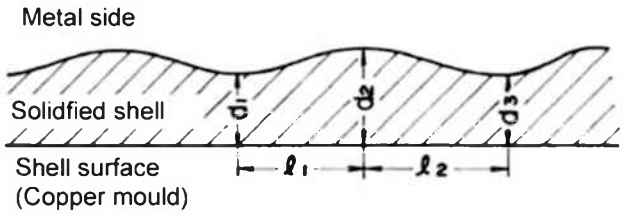

$$\frac{\overline{\Delta d}}{l} = \frac{\sum_i^n \frac{|d_i - d_{i+1}|}{l_i}}{n}$$

Figure 4–7: Unevenness parameter according to [48] – mean slope of the shell profile.

In a more general approach Gadelmawla et al. [49] summarize 59 surface roughness parameters for many fundamental problems such as friction, contact deformation, heat and electric current conduction to name but a few. The different parameters are specifically designed for different manufacturing processes and respective surface characteristics. Generally they are categorised into amplitude, spacing and hybrid parameters. The applied parameters for continuous casting respectively dipping tests are hybrid parameters, which are a combination of amplitude and spacing parameters. In Figure 4–8 Gadelmawla et al. present a detailed illustration of the mean slope of profile calculation. This is exactly the method used by Suzuki et al. [45] and Murakami et al. [44] [48], who calculated the mean slope of the profile according to the illustrated formulas. Determining all slopes between each two successive points of the surface profile and taking the average of these slopes calculates the presented parameter.

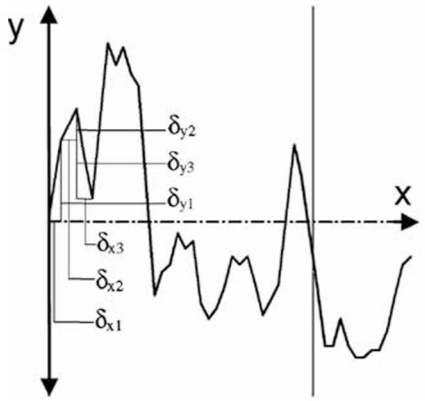

$$\Delta_a = \frac{1}{L}\int_0^L \left|\frac{dy}{dx}\right| dx$$

$$\Delta_a = \frac{1}{n-1}\sum_{i=1}^{n-1} \frac{\delta_{y_i}}{\delta_{x_i}}$$

Figure 4–8: Detailed calculation of the mean slope of the profile [49].

The second unevenness parameter was used by Yamaguchi et al. [46]. Although Yamaguchi et al. used the same experimental procedure than Murakami and Suzuki to study the solidification of stainless steels, the authors used a differently defined unevenness parameter to evaluate their findings. In their work they use the *variation coefficient* to quantify the solidification unevenness. The variation coefficient is defined as the ratio of the standard

deviation σ to the mean X. As can be seen in Figure 4–9 the distance between two consecutive measuring points was chosen to be 5 mm.

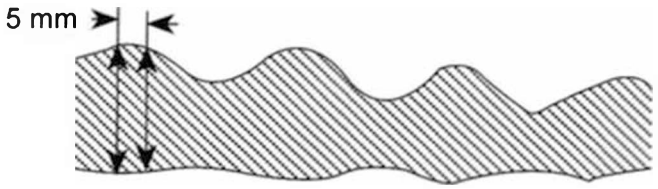

$$C_V = \frac{\sigma}{X}$$

c_V: Variation coefficient
σ: Standard deviation of shell thickness
X: Average of shell thickness

Figure 4–9: Unevenness parameter according to [46] – variation coefficient.

Both presented methods to calculate the unevenness parameter have their place for the respective situation and are verified for the present experiments in the following. In order to calculate the unevenness parameters the numeric data of the profile contour had to be processed. The applied procedure for the determination of the variation coefficient is described using the example alloy A1-0.04%C 1%Mn.

In the present experimental procedure the specimen was dipped into the melt at a constant speed until it reached a depth of 100 mm and pulled out instantly afterwards at the same constant speed. The specimen-tip was surrounded by melt for 10 seconds, whereas at a distance of 100 mm form the tip the specimen touched the melt only for an instant. This resulted in a gradually increasing shell thickness towards the specimen tip, as can be seen in Figure 4–10 (a) for the alloy A1-0.04%C 1%Mn. In order to use the unevenness parameter calculation described by Yamaguchi et al. [46] the increased tip shell growth had to be compensated. Therefore a law of growth was fitted utilising following formula:

$$y = K * \sqrt{t}$$

Here, y is the shell growth, K the solidification rate coefficient determined by linear regression and t the dipping time. Miłkowska-Piszczek et al. [50] describe the growth law more comprehensively and state average values of solidification rate coefficients for carbon steels of 22 mm/min^{-1}. The red line in Figure 4–10 (a) represents the fitted law of growth for the four illustrated specimen contours. The fitted solidification rate coefficient was 15.4 mm/min^{-1}. A possible reason for the resulting difference of solidification coefficients may be the increased superheating (about 30 K) above the equilibrium liquidus temperature. However, the order of magnitude of the fitted coefficient corresponds to literature values. In conclusion the results of the simple dipping test can be used to describe the solidification behaviour in the mould of an operational continuous caster.

In Figure 4–10 (b) the difference of the measured specimen contours and the law of growth is plotted over the specimen length for the alloy A1-0.04%C 1%Mn. The difference contours were used to evaluate the specimen unevenness according to Yamaguchi et al. [46]. Since the variation coefficient can only be computed for non-negative values, a constant factor of 2 was added to each alloy contour. In comparison to Figure 4–9 there was no separation of the solidified shell and the specimen. Thus the abscissa represents the inner shell surface and was used to calculate the shell thickness respectively the variation coefficient.

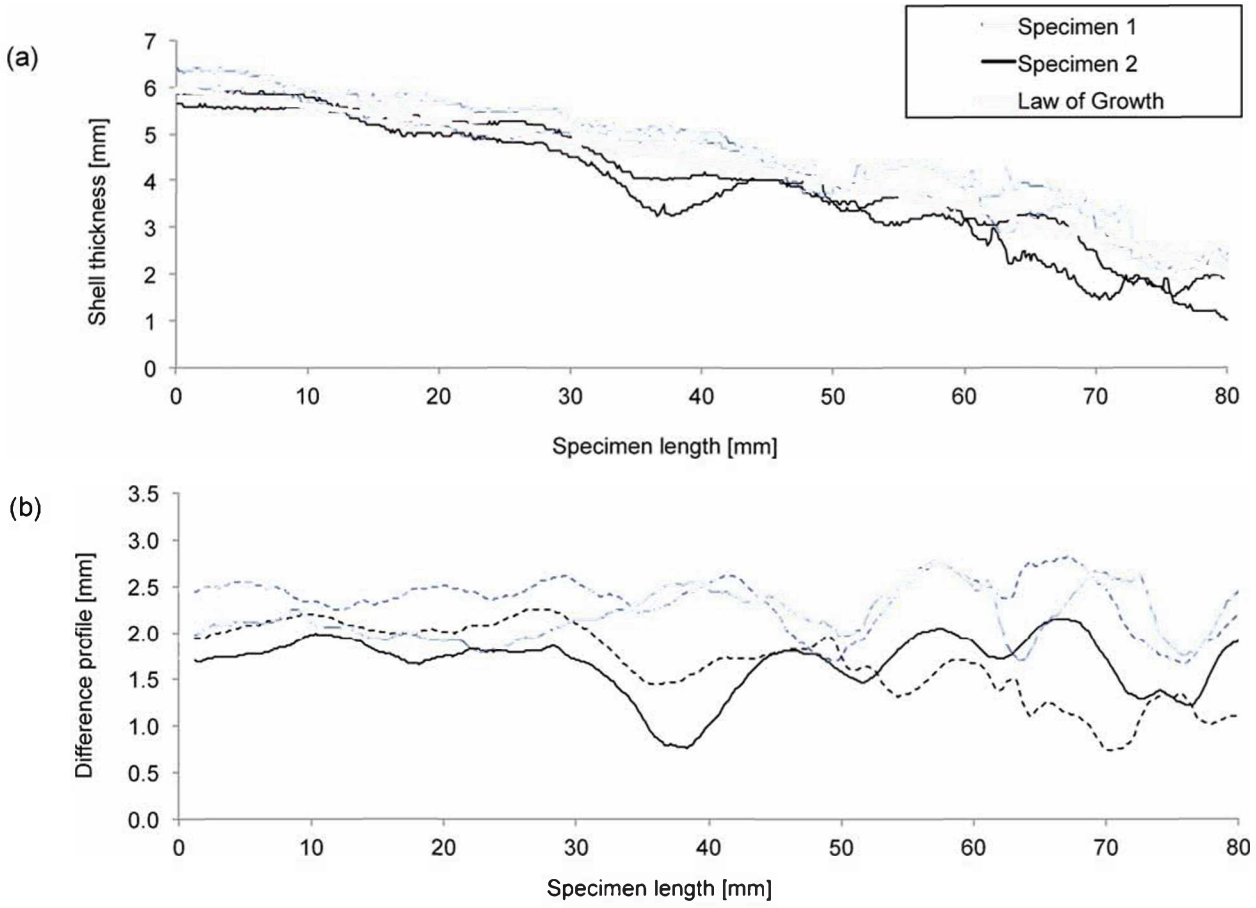

Figure 4–10: Measured shell thickness over the analysed dipping length and fitted law of growth (a) and difference profile of the surface roughness along the specimen (b) for the alloy A1-0.04%C 1%Mn.

Generally, the numeric data showed random fluctuations that had to be smoothed out before further data processing. Figure 4–11 shows an enlarged profile section of the alloy E1-0.05%C 1%Si. Due to scanning and conversion into numeric values the profile exhibits random fluctuation, which is represented by the black line. For the above-presented calculation of the mean slope this fluctuation would lead to increased values and reduce the parameters expressiveness. Thus, the simple moving average (n=10 corresponds to 1.2 mm) was applied to smooth out fluctuations, represented by the red line.

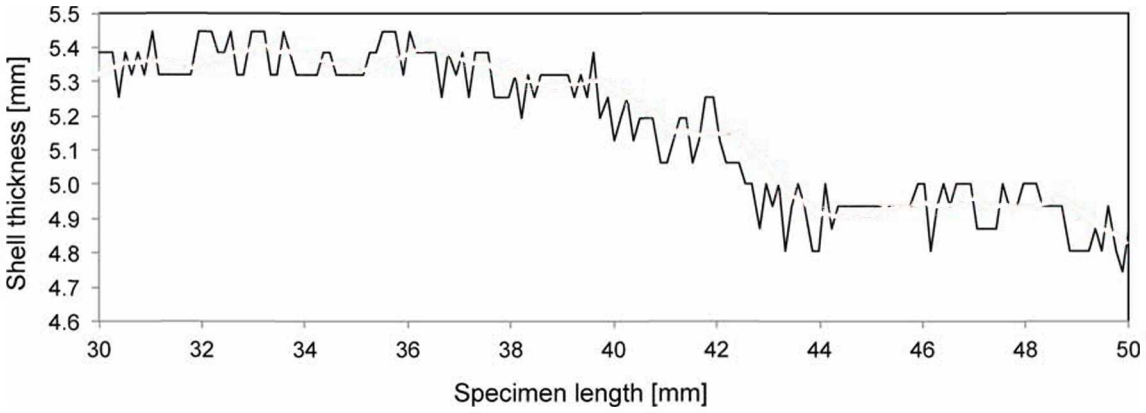

Figure 4–11: Moving average for profile smoothing to reduce random fluctuation of the alloy A1-0.04%C 1%Mn.

Finally, Figure 4–12 compares the unevenness parameter calculated for alloy A1-0.04%C 1%Mn according to the two discussed methods, namely *mean slope* and *variation coefficient*. In (a) the absolute values and the particular standard deviations show the difference of the unevenness parameters. It can be noted that the standard deviations exhibit nearly consistent values in case of the variation coefficient represented by the red graph. In contrast the calculated mean slope values show an increasing standard deviation for high unevenness values. Therefore the standard deviation of the mean slope profile can also be considered as an "unevenness factor". Figure 4–12 (b) illustrates the unevenness parameter values in relation to the smallest value of the respective method (scaled parameter). This diagram shows the slightly greater relative difference between the mean slope values.

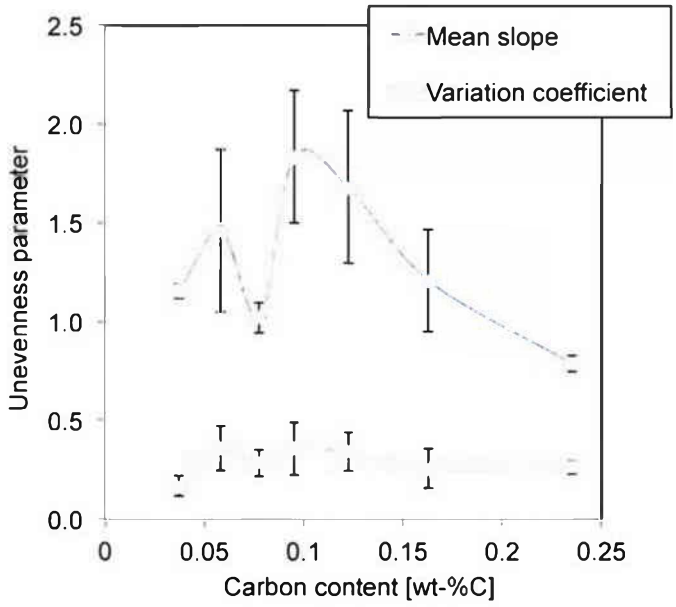

Figure 4–12: Comparison of unevenness parameters based on the mean slope and variation coefficient for the alloy A1-0.04%C 1%Mn quantified in absolute (a) and scaled (b) values.

The verification of the two presented methods to calculate the unevenness parameter showed that the mean slope has several advantages. The graph of the mean slope parameter presents more distinguishable results. Additionally, the standard deviation of each data point allows to draw conclusions on the shell unevenness. In case of the mean slope it is not necessary to fit a law of growth reducing a possible error source. In conclusion, the mean slope of profile was selected to calculate the unevenness parameter for the experiments. In summary, Figure 4–13 depicts the process flow for the data analysis of one investigated alloy composition. Note that the mean slope calculation takes into account each measured data point after the data smoothing.

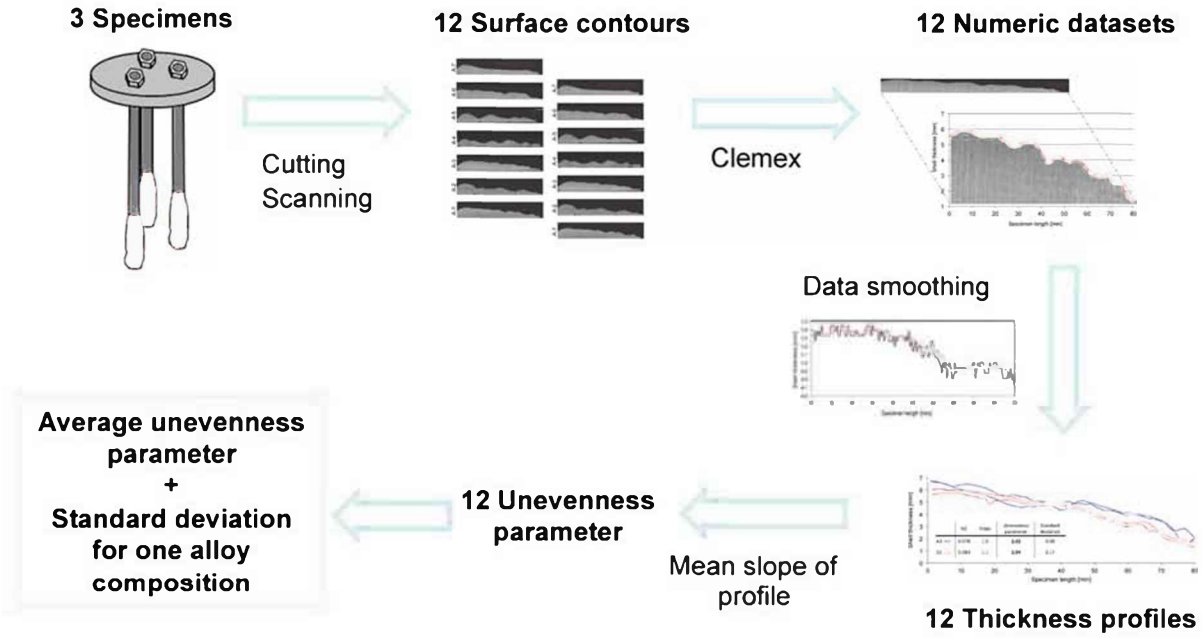

Figure 4–13: Process flow of the dipping test data analysis for one alloy compositions

4.3.2 Reproducibility

Results that tell a great story but cannot be reproduced when the experiments are run a second time will not provide any research benefit. Therefore it is most important to ensure reproducibility of experimental observations to obtain conclusive investigational results. In order to validate the dipping test some experimental compositions were replicated. This chapter presents the findings of the reproducibility measurements.

At different days and as a part of two experimental series, namely manganese and carbon variation, the alloy composition 0.08 wt.-% carbon and 1 wt.-% manganese were replicated. The measured compositions and calculated unevenness parameters are shown in Figure 4–14. Additionally, the diagram compares the two alloys by means of two exemplary specimen contours each. Both alloys show curve progressions without pronounced oscillations. Note

that the axes in Figure 4–14 are not proportional and that the y-axis is enlarged. It can be seen that both alloys have nearly the same unevenness parameter, with alloy B2 exhibiting an increased standard deviation. Overall the two investigated alloys are in good accordance with each other and the dipping tests provide comparable results.

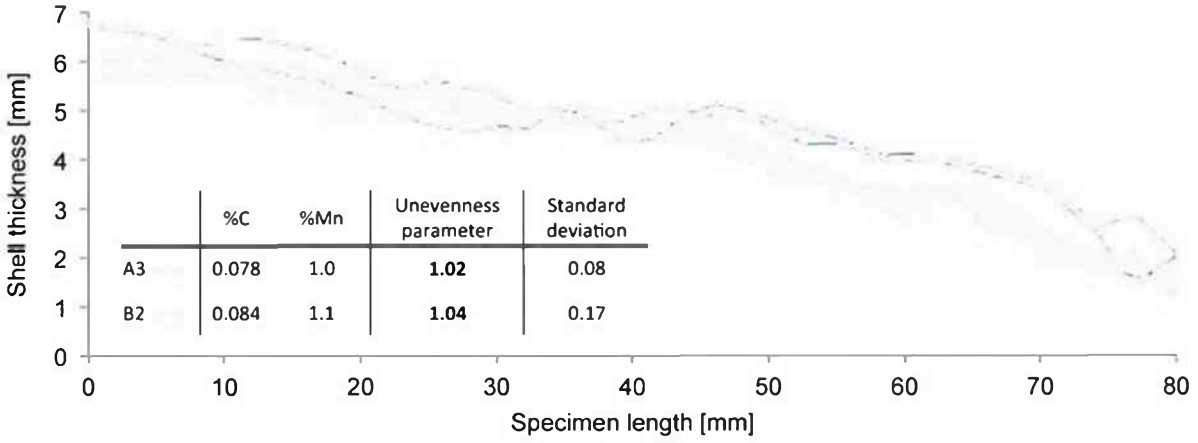

	%C	%Mn	Unevenness parameter	Standard deviation
A3	0.078	1.0	**1.02**	0.08
B2	0.084	1.1	**1.04**	0.17

Figure 4–14: Comparison of two exemplary specimen contours per alloy composition A3-0.078%C 1%Mn and B2-0.084%C 1.1%Mn.

Maintaining constant experimental and data evaluation conditions for the dipping test has proven to be difficult in terms of super-heating, exact alloy composition and slag contamination on the specimen surface. However, the dipping test is a macroscopic melting experiment at temperatures of about 1550°C, in which some range of variation is acceptable. For instance, the above-mentioned alloys show slightly varying alloy composition. The deviations are within the measuring accuracy of the spectrometer. Hence, the presented dipping test results are valid in consideration of the achievable measurement accuracy.

4.3.3 Slag Contaminations

In particular for alloys with higher manganese and no silicon content the presence of a crumbly slag caused slag deposits on the specimen surface. Figure 4–15 exemplary displays the slag contamination of alloy B5-0.08%C 3.5%Mn and the obtained numeric thickness values as a function of the specimen length. The pronounced peak of the slag deposit or other severe skips, such as shrinkage cracks, would increase the mean slope respectively the unevenness parameter significantly. Therefore the data of the contaminated contour section had to be removed. The blue section in Figure 4–15 was not considered for the unevenness parameter determination.

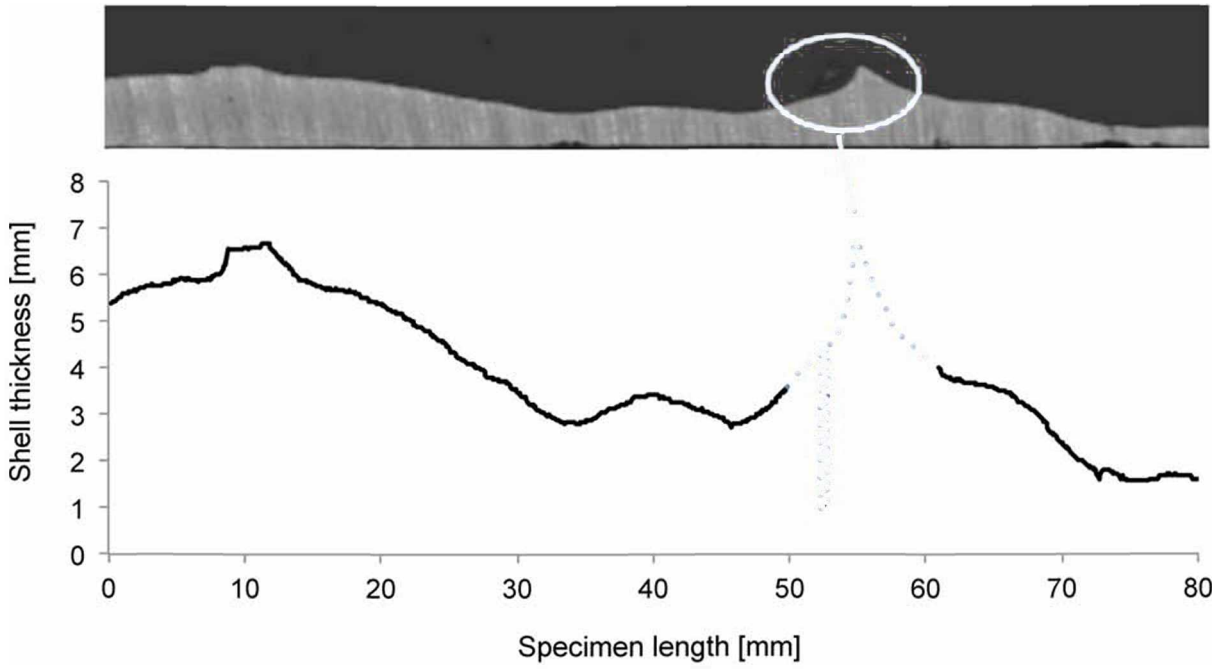

Figure 4–15: Procedure to remove slag contaminations, exemplary for alloy B5-0.08%C 3.5%Mn.

4.4 Dipping Test – Experiments

As explained in the previous sections, dipping tests are a feasible option to study the initial shell formation on a macroscopic scale. Hence the test is an observation method with a closer relation to industrial scale than HTLSCM investigations. Studying the unevenness of the solidified shell allows to make deductions for the initial shell growth within the continuous casting mould and consequential product quality. The presented investigations aim to answer the initial question of how manganese influences the solidification behaviour of steels within the peritectic range with respect to C_A and C_B. Therefore five experimental series were performed, where the fourth and fifth additionally investigate the effect of silicon as well as manganese and silicon together.

Prior to every performed experiment the specimens were prepared as described in Chapter 4.2.1. Aluminum granule was used to deoxidize the molten steel. With respect to the changing liquidus temperature for different alloy compositions, the superheating was adjusted accordingly. Following chapters present the results of each experimental series. Additionally, interconnections are created between individual alloys and compared according to the hypo- or hyper-peritectic alloys. Subsequently, in Chapter 4.5 the results are discussed more comprehensively.

4.4.1 Carbon Variation at 1 wt.-% Mn

In order to investigate the shell formation as a function of the carbon content seven dipping tests of the alloy compositions shown in Table 4–1 were performed. The manganese content of the melt was held constant at 1 ± 0.1 wt.-%. Moreover the Table 4–1 illustrates the unevenness parameter in a red-yellow-green colour scale. Superheating of the melt was kept 30 K above the equilibrium liquidus temperature with a tolerance of ± 10 K. The objective of this experimental series was to examine the feasibility of the described technique.

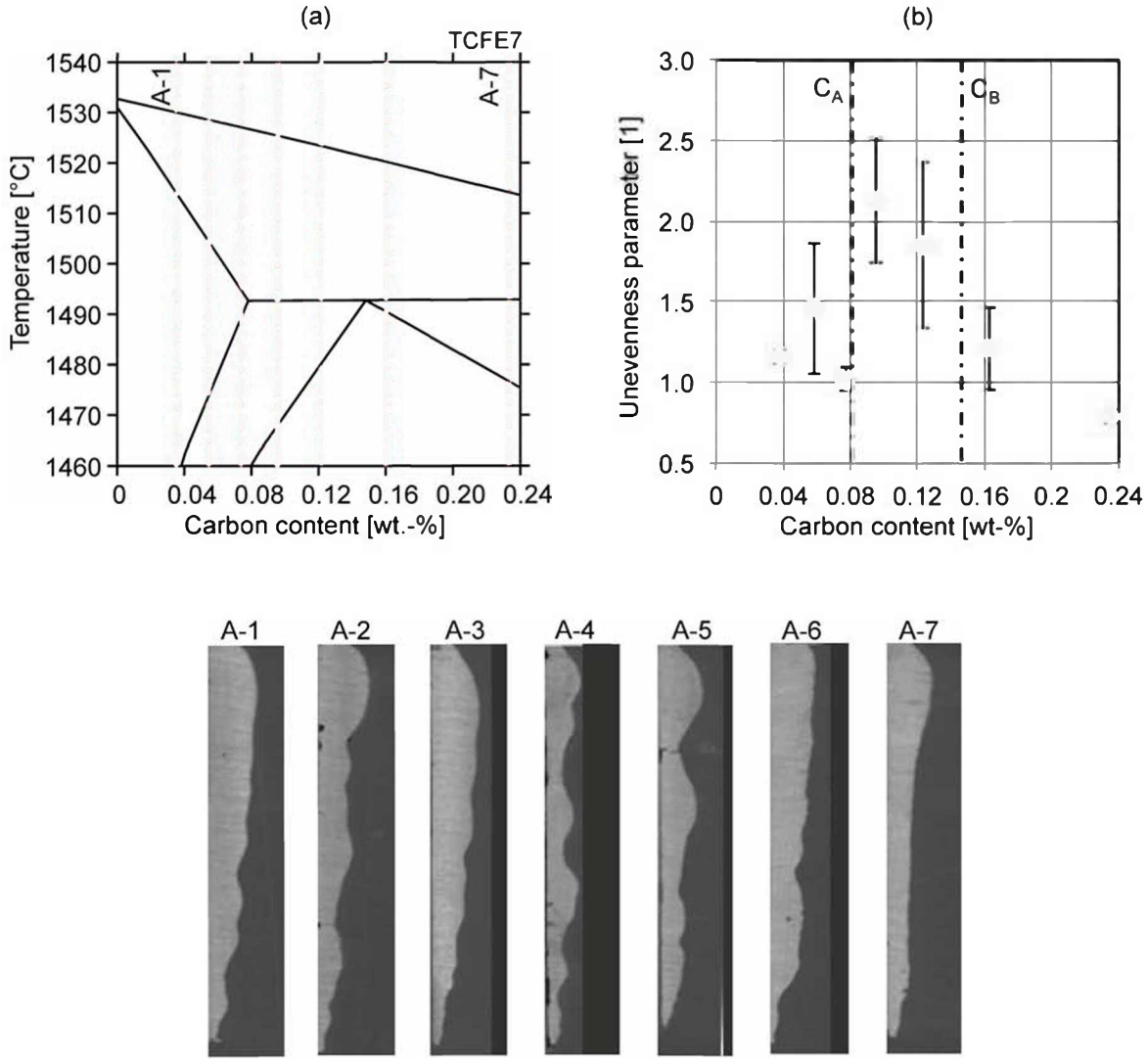

Figure 4–16: Carbon variation alloy compositions marked in the peritectic area of the iron-carbon phase diagram for a manganese content of 1 wt.-% (a), calculated unevenness parameter as a function of carbon content (b) and exemplary specimen contours for each dipping cycle.

Figure 4–16 comprises the results of experimental series A. In Figure 4–16 (a) the target carbon compositions are marked in the peritectic area of the iron-carbon phase diagram for a constant manganese content of 1 wt.-%. The calculated unevenness parameter as a function

of carbon content is depicted in (b). Additionally, Figure 4–16 shows an exemplary specimen contour for each dipping. It can be argued that some of the scanned contours seem more or less uneven. It is hence important to consider the standard deviation of the simultaneously dipped specimens. The course of the course for the unevenness parameter exhibits a recognizable transition in the solidification behaviour when passing through the hypo-peritectic section of the phase diagram. The low-carbon alloy A2 displays an increased unevenness and associated standard deviation. A7 shows the smoothest solidification.

Table 4–1: Alloy composition and the unevenness parameter including standard deviation (normally distributed) - carbon variation at constant 1 wt.-% Mn.

	%C	%Mn	Unevenness parameter	Standard deviation
A1	0.04	0.9	1.16	0.04
A2	0.06	0.9	1.46	0.41
A3	0.08	1.0	1.02	0.08
A4	0.10	0.9	1.83	0.33
A5	0.12	1.0	1.68	0.38
A6	0.16	1.0	1.21	0.26
A7	0.24	1.1	0.79	0.04

4.4.2 Manganese Variation at 0.08 wt.-% C

This series was particularly aimed to investigate if increasing manganese contents lead to an apparent transition between C_A and C_B. The experiments where performed at a constant carbon content of 0.08 wt.-%. Table 4–2 lists the investigated alloy compositions and the observed unevenness. The colour scale indicates the relative unevenness. It clearly shows an increasing unevenness with increasing manganese content. In Figure 4–17 the alloy compositions are plotted in an iron-manganese phase diagram for a constant carbon content of 0.08 wt.-%. Additionally, the unevenness in correlation to the manganese content is delineated. A more detailed discussion of the results is given in Chapter 4.5.

Table 4–2: Alloy composition and the unevenness parameter including standard deviation (normally distributed) - manganese variation at constant 0.08 wt.-% C.

	%C	%Mn	Unevenness parameter	Standard deviation
B1	**0.077**	0.4	0.81	0.20
B2	0.084	1.1	1.04	0.17
B3	**0.077**	1.3	0.98	0.19
B4	0.084	2.9	1.22	0.34
B5	0.084	3.5	1.18	0.15
B6	0.082	5.8	1.47	0.13

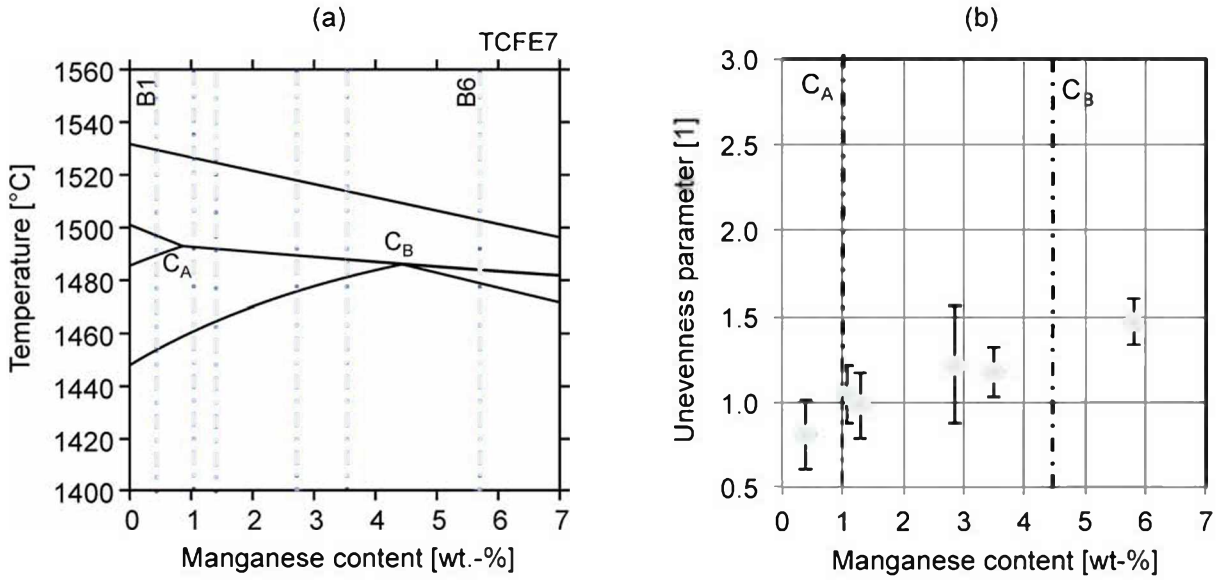

Figure 4–17: Alloy compositions marked in the peritectic area of the iron-manganese phase diagram for a constant carbon content of 0.08 wt.-% (a), calculated unevenness parameter as a function of manganese content (b).

4.4.3 Carbon Variation at 3.5 wt.-% Manganese

The results of two alloys that were dipped to examine the behaviour of a low carbon, hypo-peritectic and hyper-peritectic steel with increased manganese content are presented in the following. Therefore alloy C1 and C2 supplemented alloy B5. Table 4–3 presents the compositions and unevenness parameter of the three alloys with manganese contents of 3.5 wt.-%. The respective phase diagram and unevenness plot is shown in Figure 4–18.

Table 4–3: Alloy composition and the unevenness parameter including standard deviation - supplementary alloys with 3.5 wt.-% Mn.

	%C	%Mn	Unevenness parameter	Standard deviation
C1	0.04	3.4	1.07	0.37
B5	0.08	3.5	1.18	0.15
C2	0.14	3.4	1.06	0.10

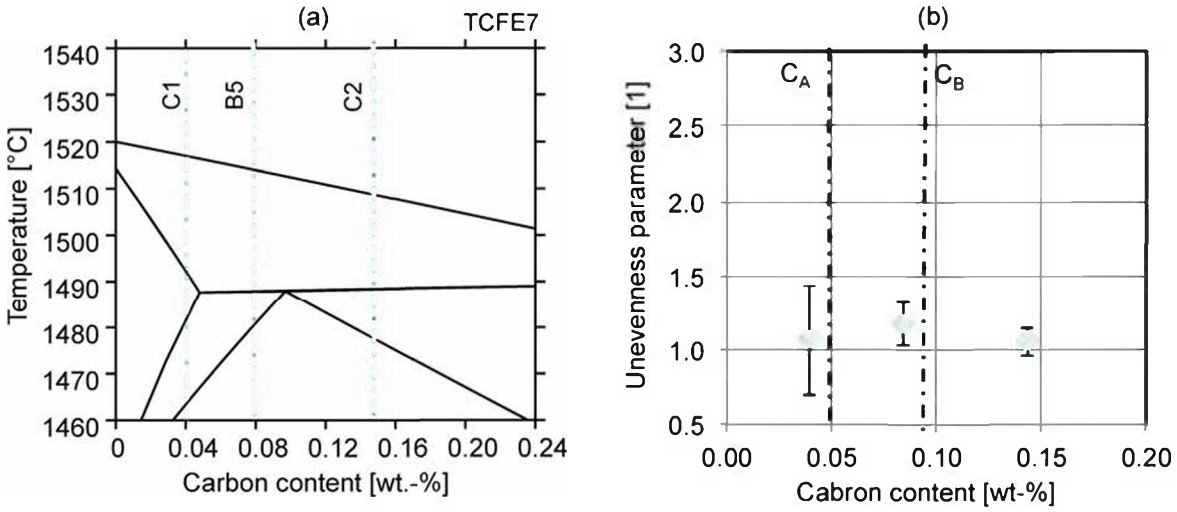

Figure 4–18: Alloy compositions marked in the peritectic area of the iron-manganese phase diagram for a constant manganese content of 3.5 wt.-% (a), calculated unevenness parameter as a function of carbon content (b).

4.4.4 Carbon Variation at 1 wt.-% Si and 1 wt.-% Si & 2 wt.-% Mn

The investigated alloy compositions were chosen because their respective phase diagrams had been studied by means of differential-scanning-calorimetry (DSC) measurements at the Chair of Ferrous Metallurgy at the University of Leoben by Presoly [43]. The DSC measurements aim to validate the thermodynamic data used by commercial software packages. The phase diagrams (a) and (c) shown in Figure 4–19 are plotted using DSC measurements. Note that the data points represent DSC-results whereas the full lines

are plotted using the commercial thermodynamic database TCFe7 [29]. In Figure 4–19 (c) it can be clearly seen that the DSC measurements are deviating from the calculated data for an alloy with 1 wt.-% Si and 2 wt.-% Mn. In order to gain further insight on such alloy systems, it is interesting to examine the studied phase diagram utilising the dipping test.

For the alloys D1-D3 a comparison of the qualitative visual assessment prior to cutting and the measured unevenness parameters showed very good agreement. As shown in Table 4–4 D2 has the highest unevenness parameter of all dipped specimens. This stands in stark contrast to D1 and D3 and it was hence possible to make a qualitative statement before the actual analysis. On the other hand the carbon variation at a constant content of 1 wt.-% Si and 2 wt.-% Mn showed consistent unevenness values with relatively large standard deviations.

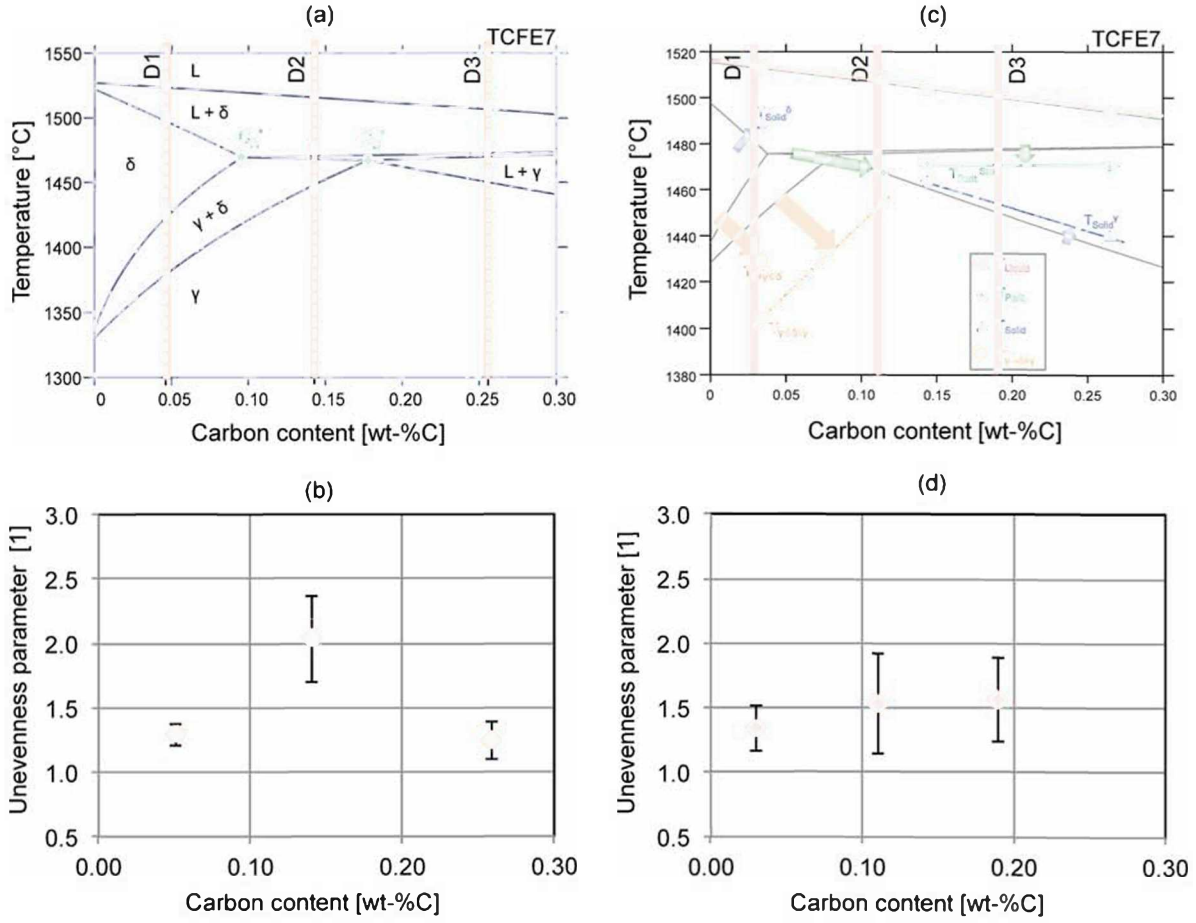

Figure 4–19: Alloy compositions plotted in the peritectic area of the iron-carbon phase diagram for a constant content of 1 wt.-% Si (a) and 1 wt.-% Si, 2 wt.-% Mn (c) [43] , calculated unevenness parameter for the respective compositions as a function of carbon content (b) (d).

Table 4–4: Alloy composition and the unevenness parameter including standard deviation (normally distributed) - carbon variation at constant 1 wt.-% Si and 1 wt.-% Si, 2 wt.-% Mn.

	%C	%Mn	%Si	Unevenness parameter	Standard deviation
D1	0.05	-	1.1	1.29	0.08
D2	0.14	-	1.0	2.03	0.34
D3	0.26	-	1.0	1.24	0.14
E1	0.03	2.10	1.04	1.34	0.18
E2	0.11	1.89	0.93	1.53	0.39
E3	0.19	1.95	1.00	1.56	0.32

4.5 Discussion

The dipping test demonstrates a newly developed methodology that guarantees a systematic analysis to assess the unevenness of the solidified shell. In order to increase the statistical significance and experimental reproducibility three specimens were simultaneously dipped and subsequently the unevenness parameter of 12 surface contours averaged. This chapter aims to summarise the presented results and look at them from a wider perspective. The dipping experiments comprised alloy compositions up to 5.8 wt.-% manganese and 0.24 wt.-% carbon. The experiments aimed to clarify the influence of the position in the alloy specific pseudo binary phase diagram with particular focus on manganese.

The results of the carbon variation (0.04-0.24 wt. %) with a constant manganese content of 1 wt. % presented in Chapter 4.4.1 clearly show that hypo-peritectic alloys (between C_A and C_B) exhibited doubled unevenness values. In this case the results of the practical solidification experiments are in good agreement with the prediction made by equilibrium considerations and coincide with the findings of other researchers. The maximum unevenness is found slightly to the right of C_A and the values are decreasing towards higher carbon contents. Outliers of individual contours might explain an increased unevenness and concomitant standard deviation of alloy A2-0.06%C 1%Mn. However, for higher manganese contents and overall alloying contents the results seem to behalf differently, which is discussed in the following.

In contrast the manganese variation (0.4-5.8 wt. %) of Chapter 4.4.2 appears to gradually increase towards higher manganese contents. When comparing the absolute values of both experimental series between C_A and C_B, it can be seen that e.g. alloy B4-0.08%C 2.9%Mn and B5-0.08%C 3.5%Mn exhibit relatively low unevenness values compared to

A4-0.10%C 1%Mn and A5-0.12%C 1%Mn. The findings indicate that for higher manganese contents the approach that the solidification is exclusively influenced by the position in the phase diagram might not be applicable. This view is reinforced by alloy C1-0.04%C 3.4%Mn and C2-0.14%C 3.4%Mn presented in Chapter 4.4.3. The absolute unevenness parameters of the three investigated 3.5 wt.-% Mn alloys are almost the same, although the alloys belong to three different solidification types (see Chapter 2).

Table 4–5: Comparison of hypo- and hyper-peritectic alloys

Hypo-pertiectic alloys (between C_A & C_B)

	%C	%Mn	Unevenness parameter	Standard deviation
A4	0.10	0.9	1.83	0.33
A5	0.12	1.0	1.68	0.38
B2	0.08	1.1	1.04	0.17
B4	0.08	2.9	1.22	0.34
B5	0.08	3.5	1.18	0.15

Hyper-pertiectic alloys (right of C_B)

	%C	%Mn	Unevenness parameter	Standard deviation
A6	0.16	1.0	1.21	0.26
A7	0.24	1.1	0.79	0.04
C2	0.14	3.4	1.06	0.10
B6	0.08	5.8	1.47	0.13

Table 4–5 groups the investigated alloys according to their solidification type into hypo- and hyper-peritectic alloys. Note that each alloy is categorised in the associated equilibrium phase diagram. It can be clearly seen that both groups contain even and uneven specimens. This consideration appears to negate the question raised in the beginning that the relative position with respect to C_A / C_B is exclusive influence of the solidification behaviour. Looking at the hyper-peritectic results more closely, it can be argued that B6-0.08%C 5.8%Mn is the only outlier in this group and that the other values have low unevenness values. Future experiments should therefore investigate alloys with manganese contents beyond 5 wt.-% and various carbon contents. On the other hand the hypo-peritectic results display inconsistent unevenness parameters over all experiments. A more precise consideration within the hypo-peritectic range was not feasible as will be explained in the following paragraph.

The measuring accuracy of the spark spectrometer is ± 0.01 wt.-% carbon for the applied testing standard. Changing the carbon content by 0.01 wt.-% significantly shifts the equilibrium position of C_A and C_B, as can be seen in Figure 4–20. The measuring error is higher for most of the other alloying elements. All considerations should take this into account. Therefore the results should be considered as a trend rather than an exact point measurement. For instance, according to the unevenness parameter values alloy B3-0.08%C 1.3%Mn (see Chapter 4.4.2) is slightly more uneven than alloy B2-0.08%C 1.1%Mn, which is supposedly further right of C_A. However, if alloy

B3-0.08%C 1.3%Mn had a lower carbon content within the measuring tolerance, its position would shift to the right of C_A. Supposing that the relative position to C_A determines the solidification, this could explain the slightly increased unevenness of C_B.

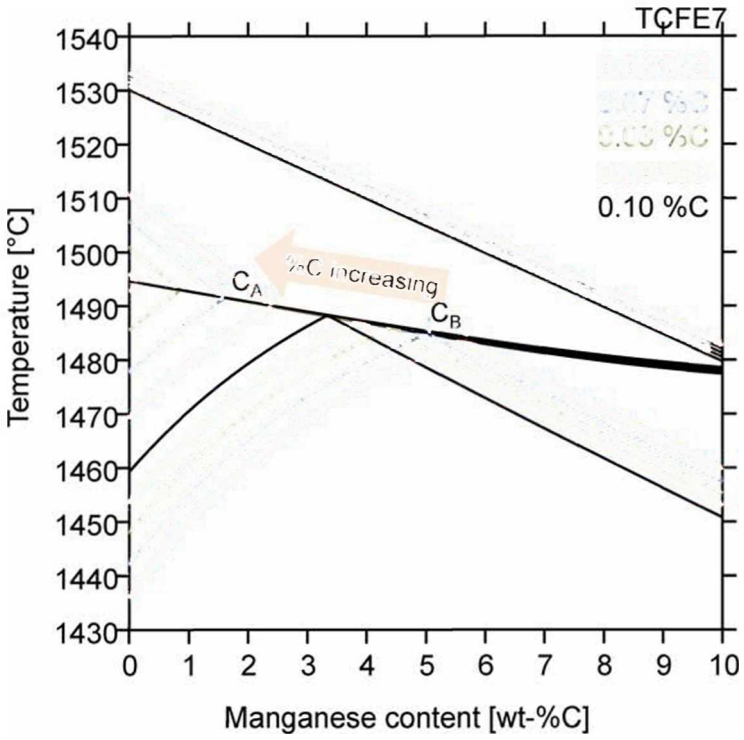

Figure 4–20: Pseudo-binary system superimposed for different carbon contents.

The investigations of silicon containing alloys presented in Chapter 4.4.4 also showed the above-described distinction between low and higher alloyed steels. The series containing 1 wt.-% Si shows a pronounced position dependency in the equilibrium phase diagram. The unevenness parameter difference between the hypo-peritectic D2-0.14%C 1%Si and the other alloys can be clearly seen. On the other hand the addition of 2 wt.-% manganese displayed almost similar unevenness parameters for all carbon contents. These results indicate that low-alloyed steels follow the solidification behaviour predicted by the equilibrium phase diagram, whereas for increased alloy contents the solidification seems to be determined by other effects.

In order to avoid incrustation of the crucible and improve the oxidation prevention a synthetic slag was used to cover the melt for alloys with more than 3 wt.-% Mn. This might be the reason for the fact that high-alloyed steels were more prone to slag contamination. Even though the formed slag was removed just before the dipping, it was not possible to prevent individual slag particles from affixing to the solidifying shell. Chapter 4.3.3 explains how the larger contaminations were removed form the analysed contours. Although great care was taken when removing sections, the manual removal interferes with the standardised analysis

method. Furthermore, it is not clear in what way the slag influences the solidification behaviour overall.

In Chapter 2.3 the question was raised if the solidification behaviour of steels within the peritectic range is exclusively influenced by the position along the peritectic line regardless of the manganese content. The results of the presented dipping setup suggest that the solidification of steels with higher alloying contents is not strictly determined by the relative position to C_A and C_B. However, this might be a result of the limited number of investigated alloys, which could have missed to observe the solidification of decisive alloy compositions and perhaps change the interpretation of the results. On the contrary all the investigated alloys with 1 wt.-% Mn or Si and below perfectly follow the approach that hypo-peritectic alloys (between C_A and C_B) solidify more uneven. However, the presented dipping experiments show first results of a feasible method to investigate the complex processes of the initial solidification of peritectic steels.

5 Summary and Conclusion

The presented thesis is about the influence of manganese on the solidification behaviour of peritectic steels. In continuous casting, steels that undergo the peritectic transition are particularly prone to casting defects. At the beginning of this thesis the literature review comprises the relevant fundamentals of the peritectic transition, a comprehensive summary of the massive transformation and previous research about manganese and the peritectic transition. The peritectic transition consists of the peritectic reaction, which is the nucleation and growth of γ-austenite along the liquid/δ-ferrite interface, and the subsequent thickening and growth of γ-austenite into liquid and δ-ferrite. The phase transformation and accompanied volume contraction of about 6 % is agreed to be a root cause of a variety of problems in continuous casting of peritectic alloys. Another potential reason for many quality defects is a rapid phase transformation, known as massive transformation. The occurrence of massive transformation is linked to significant undercooling of the transition below the equilibrium peritectic temperature. In previous research the undercooling has been connected to the diffusion field across the liquid/solid interface, which is mostly affected by the alloys carbon content. However results of SSCC and HTLSCM experiments about the influence of manganese on the peritectic transition remain controversial.

Therefore a combination of HTLSCM experiments and dipping tests was used in an attempt to gain further insight on the root cause of these defects and the specific effect of manganese. The application of the so-called "concentric solidification technique" for HTLSCM made it possible to model the early stages of solidification in the mould of a continuous caster on a microscopic scale. On the other hand the dipping test resembled the actual thin shell of the initial solidification on a macroscopic scale. The shell unevenness is quantified in a so-called "unevenness parameter" that allowed the comparison of differently

solidified steel shells. The experimental investigations aimed to answer two questions, which will be discussed successively in this section.

1. *Do higher manganese contents increase the undercooling below the equilibrium peritectic temperature and does this intensify the massive transformation of the peritectic transition?*

The in-situ observation of the solidification using a HTLSCM was the method of choice to study the massive transformation. The HTLSCM results reveal that alloys with increased manganese contents, namely alloy PB 1% Mn and PC 2% Mn, seem to show that manganese has no significant effect on the kinetics and morphology of the massive transformation, but display the development of a distorted solid/liquid interface due to segregation. Even at a low cooling rate of 2 K/min pronounced segregation occurred. The results seem to confirm the observations made by Griesser [3] that the transformation mode and morphology are controlled by fraction of primary solidified δ-ferrite, the consequential steep carbon concentration gradient and the resulting undercooling. In addition lower cooling rates lead to a planar like transformation morphology.

2. *Is the solidification behaviour of steels within the peritectic range exclusively influenced by the relative position with respect to C_A / C_B regardless of the manganese content?*

In order to answer this question, the investigated alloys have to be divided into two groups, namely with only 1 wt. % Mn and with higher contents up to 5.8 wt. % Mn. The statement that hypo-peritectic alloys (between C_A and C_B) solidify more uneven, i.e. doubled unevenness values, is clearly valid for alloys with 1 wt. % Mn. This is underpinned on the one hand by the dipping experiments and, on the other hand, by the HTLSCM results, where the relative position regarding the point C_B determines the velocity of the interface progression and the total migration distance. However, the performed dipping results suggest that steels with higher manganese contents are not strictly determined by the relative position to C_A and C_B. Similar results were found for alloys containing silicon, where 1 wt. % Si alloys behaved like 1 wt. % Mn alloys. On the other hand alloys containing 1 wt. % Si and 2 wt. % Mn seem to exhibit no significant position dependency. The results demonstrate no apparent trend of the unevenness parameter regardless of the supposed solidification type. Instead, the unevenness values remain low even for compositions within the hypo-peritectic region in the equilibrium phase diagram. However, the number of investigated alloys was limited and it can be argued that the presented experiments missed to observe the solidification of decisive alloy compositions, which would lead to a different view of the results.

In addition to the results described, a major part of the work was the modification of the HTLSCM setup to alloys containing more than 1 wt. % manganese and the development of a standardised dipping test. In case of the HTLSCM technique, the application of the "crucible with suspension points" was necessary to establish a stable liquid pool of high-alloyed steels within an appropriate time. Secondly, the newly developed methodology of the dipping test presented a systematic analysis to assess the unevenness of the solidified shell. The statistical significance and the experimental reproducibility were increased due to simultaneous dipping of three specimens. Following an assessment of the different unevenness parameter used in literature, the most meaningful and comparable analysis was applied in a standardised manner to all dipped specimens. The presented dipping experiments show first results of a feasible method to investigate the complex processes of the initial solidification.

Finally, the following improvements of the experimental setup are proposed:

It is questionable whether an investigation of high-alloyed steels is feasible in the current furnace setup of the HTLSCM. The evaporation of alloying elements leads to the contamination of the infrared furnace and might hence change the thermal conditions within the crucible in the course of an experiment. Additionally, the evaporation and oxidation of carbon and other alloying elements causes a permanent variation of the specimen composition, which does not only affect the respective phase diagram and temperature calibration but also on the bottom line the actual composition of the investigated alloy is unknown. Therefore the furnace atmosphere and general setup should be reconsidered prior to future experiments. Further modifications to the HTLSCM-setup are given in [4] and [8]. In multi-component systems special attention should be given to the effect of liquidus and solidus temperature difference.

In order to improve the dipping test a more accurate measurement of the chemical composition is desirable. The analytical distinction of two investigated alloys is limited to the measurement accuracy of the spark spectrometer. Furthermore, new methods should be considered to improve the oxidation protection and reduce the concomitant slag contamination of specimens for high-alloyed steels. The statistical significance could be further enhanced by the application of a non-destructive, optical measurement method of the specimen surface contour.

The bottom line: The experimental findings presented in this thesis provide some useful information about the initial solidification behaviour of peritectic steels with special regard to the influence of manganese. In order to attain a holistic picture, a larger number and variety of alloys needs to be investigated.

6 Bibliography

[1] Wirtschaftskammer Österreich, Weltstahlproduktion; Available from: https://www.wko.at/Content.Node/branchen/sbg/Bergwerke-und-Stahl/Anteil-an-der-Weltstahlproduktion-2015.pdf, Access date: 19.05.2016.

[2] Wirtschaftsvereinigung Stahl; Available from: http://www.stahl-online.de/index.php/themen/stahltechnologie/stahlerzeugung/3/, Access date: 19.05.2016.

[3] Xia, G., Vergießen peritektischer Stähle, Montanuniversität, lecture, 30.01.2012.

[4] Griesser, S., In-Situ Study of the Influence of Alloying Elements on the Kinetics and Mechanism of the Peritectic Phase Transition in Steel, Ph.D. Thesis, University of Wollongong, 2013.

[5] Kerr, W.H., J. Cisse and G.F. Bolling, On equilibrium and non-equilibrium peritectic transformations, Acta Metallurgica 22 (6) (1974), p. 677-686.

[6] Stefanescu, D.M., Microstructure evolution during the solidification of steel, ISIJ international 46 (6) (2006), p. 786-794.

[7] Shibata, H., et al., Kinetics of peritectic reaction and transformation in Fe-C alloys, Metallurgical and Materials Transactions B 31 (5) (2000), p. 981-991.

[8] Alves, C.L.M., et al., Quantitative isothermal phase-field simulations of peritectic phase transformation in FeMn system, Journal of Materials Research and Technology (2016).

[9] Moon, S., The Peritectic Phase Transition and Continuous Casting Practice, Ph.D. Thesis, University of Wollongong, 2012.

[10] Arai, Y., et al., In-Situ Observed Dynamics of Peritectic Solidification and [delta]/[gamma] Transformation of Fe-3 to 5 At. Pct Ni Alloys, Metallurgical and Materials Transactions 36A (11) (2005), p. 3065-3074.

[11] Hillert, M., Solidification and Casting of Metals, London, The Metals Society, 1979.

[12] Phelan, D., M. Reid and R. Dippenaar, Kinetics of the peritectic reaction in an Fe–C alloy, Materials Science and Engineering: A 477 (1–2) (2008), p. 226-232.

[13] Nassar, H. and H. Fredriksson, On Peritectic Reactions and Transformations in Low-Alloy Steels, Metallurgical and Materials Transactions A 41 (11) (2010), p. 2776-2783.

[14] Ohno, M. and K. Matsuura, Diffusion-controlled peritectic reaction process in carbon steel analyzed by quantitative phase-field simulation, Acta Materialia 58 (18) (2010), p. 6134-6141.

[15] Ohno, M. and K. Matsuura, Motion and Morphology of Triple Junction in Peritectic Reaction Analyzed by Quantitative Phase-field Model, ISIJ International 50 (12) (2010), p. 1879-1885.

[16] Matsuura, K., Y. Itoh and T. Narita, A Solid--Liquid Diffusion Couple Study of a Peritectic Reaction in Iron--Carbon System, ISIJ International (Japan) 33 (5) (1993), p. 583-587.

[17] Phelan, D., M. Reid and R. Dippenaar, Kinetics of the Peritectic Phase Transformation: In-Situ Measurements and Phase Field Modeling, Metallurgical and Materials Transactions 37A (3A) (2006), p. 985-994.

[18] Hillert, M., Nature of massive transformation, Metallurgical and Materials Transactions A 35 (1) (2004), p. 351-352.

[19] Hillert, M., Phase Equilibria, Phase Diagrams and Phase Transformations, Their Thermodynamic Basis, 2007.

[20] Svensson, L., Control of microstructures and properties in steel arc welds, CRC Press, 1994.

[21] Mittemeijer, E.J., Fundamentals of materials science: The microstructure-property relationship using metals as model systems, Springer Science & Business Media, 399-417, 2010.

[22] Porter, D.A., K.E. Easterling and M. Sherif, Phase Transformations in Metals and Alloys, Third Edition (Revised Reprint), CRC Press, 2009.

[23] Dippenaar, R., et al., Austenite Grain Growth and the Surface Quality of Continuously Cast Steel, Metallurgical and Materials Transactions B 45 (2) (2013), p. 409-418.

[24] Yasuda, H., et al., Massive transformation from δ phase to γ phase in Fe–C alloys and strain induced in solidifying shell, IOP Conference Series: Materials Science and Engineering 33 (1) (2012), p. 012036.

[25] Griesser, S., et al., Diffusional constrained crystal nucleation during peritectic phase transitions, Acta Materialia 67 (2014), p. 335-341.

[26] Griesser, S., C. Bernhard and R. Dippenaar, Effect of nucleation undercooling on the kinetics and mechanism of the peritectic phase transition in steel, Acta Materialia 81 (2014), p. 111-120.

[27] Moon, S., R. Dippenaar and S. Kim, The peritectic phase transition of steel during the initial stages of solidification in the mold, AISITech 2015, The Iron & Steel Technology Conference and Exposition (2015), Cleveland, At Cleveland, Ohio, USA.

[28] Xia, G., Kokillenmetallurgie des konventionellen Brammenstranggießens von Stahl Habilitation, Montanuniversität Leoben (2011).

[29] Thermo-Calc Software, TCFe7 - TCS steels/felloys database version 7.0, http://www.thermocalc.com.

[30] Bernhard, C. and G. Xia, Influence of alloying elements on the thermal contraction of peritectic steels during initial solidification, Ironmaking and Steelmaking (2005).

[31] Minsky, M., Microscopy apparatus, Patent: US3013467 A, 1961.

[32] Chikama, H., et al., "In-situ" real time observation of planar to cellular and cellular to dendritic transition of crystals growing in Fe-C alloy melts, Materials transactions. JIM 37 (4) (1996), p. 620-626.

[33] Yin, H.B., T. Emi and H. Shibata, Determination of free energy of delta-ferrite/gamma-austenite interphase boundary of low carbon steels by in-situ observation, ISIJ international 38 (8) (1998), p. 794-801.

[34] Yin, H.B., et al., "In-situ" observation of collision, agglomeration and cluster formation of alumina inclusion particles on steel melts, ISIJ international 37 (10) (1997), p. 936-945.

[35] Yin, H.B., et al., Characteristics of agglomeration of various inclusion particles on molten steel surface, ISIJ international 37 (10) (1997), p. 946-955.

[36] Shibata, H., et al., In-situ observation of engulfment and pushing of nonmetallic in steel melt by advancing melt/solid interface, ISIJ international 38 (2) (1998), p. 149-156.

[37] Lee, S.H., et al., Separation and dissolution of Al2O3 inclusions at slag/metal interfaces, Journal of Non-Crystalline Solids 282 (1) (2001), p. 41-48.

[38] McDonald, N.J. and S. Sridhar, Peritectic reaction and solidification in iron-nickel alloys, Metallurgical and Materials Transactions A 34 (9) (2003), p. 1931-1940.

[39] Reid, M., D. Phelan and R. Dippenaar, Concentric solidification for high temperature laser scanning confocal microscopy, ISIJ international 44 (3) (2004), p. 565-572.

[40] Cantor, B. and K. O'Reilly, Solidification and casting IOP Publising Ltd, CRC Press Taylor and Francis Group, 2002.

[41] Phelan, D., In-situ Studies of Phase Transformation in Iron Alloys, Ph.D. Thesis, University of Wollongong, 2002.

[42] Griesser, S., et al., SolTrack: an automatic video processing software for in situ interface tracking, Journal of Microscopy 248 (1) (2012), p. 42-48.

[43] Presoly, P. and C. Bernhard, Influence of silicon and manganese on the peritectic range for steel alloys, Proceedings of the AISTech 2016, 16 May 2016.

[44] Murakami, H., M. Suzuki and S. Miyahara, Control of uneven solidified shell formation in hypo-peritectic carbon steel, Proceedings of The Sixth International Iron and Steel Congress (1990), Nagoya, ISIJ.

[45] Suzuki, M. and Y. Yamaoka, Influence of Carbon Content on Solidifying Shell Growth of Carbon Steels at the Initial Stage of Solidifiaction Materials transactions. JIM 44 (5) (2003), p. 836 - 844.

[46] Yamaguchi, R., M. Suzuki and M. K., Control of uneven shell formation of stainless in early stage of solidifaction Materials & Processing Research Center NKK Corporation 13 (1) (1995), p. 3-11.

[47] Fuchs, N., Beeinflussung der Anfangserstarrung peritektischer Stähle durch strukturierte Kokillenflächen Bachelor Thesis, Montanuniverstiät Leoben, 2014.

[48] Murakami, H., et al., Control of uneven solidified shell formation in hypo-peritectic carbon steels in continuous casting mold, The Iron and Steel Institute of Japan (ISIJ) (1992), p. 105-112.

[49] Gadelmawla, E.S., et al., Roughness parameters, Journal of Materials Processing Technology 123 (1) (2002), p. 133-145.

[50] Milkowska-Piszcek K., et al., The methods of calculating the solidifying strand shell thickness in a continuous casting machine, Archives of Material Science and Engineering 57 (2) (2012), p. 75-79.

7 Appendix

All experimental data presented in this thesis can be found in the attached DVD. The files are structured as shown in the list below. Additionally Table 7–1 provides an overview of the dipped alloy compositions.

1) HTLSCM
    i) Videos
    ii) Data Analysis

2) Dipping Test
    i) Experimental Series
        (a) Series A
            1. Scanned Pictures
            2. Clemex-Excel-Data
        (b) Series B & C
        (c) Series D
        (d) Series E
    ii) Miscellaneous Data

Table 7–1: Overview – Dipping Test

Series A

Alloy	A-1	A-2	A-3	A-4	A-5	A-6	A-7
set %C	0.036	0.06	0.08	0.1	0.13	0.17	0.24
set %Mn	1.0						
measured %C	0.038	0.058	0.078	0.095	0.123	0.163	0.235
measured %Mn	0.85	0.90	1.00	0.90	1.04	1.00	1.08

Series B

Alloy	B-1	B-2/A3	B-3	B-4	B-5	B-6
set %C	0.08					
set %Mn	0.5	1.0	1.5	2.5	3.5	5.5
measured %C	0.077	0.084	0.077	0.084	0.084	0.082
measured %Mn	0.40	1.06	1.28	2.86	3.49	5.80

Series C

Alloy	C-1	C-2
set %C	0.04	0.15
set %Mn	3.5	
measured %C	0.039	0.143
measured %Mn	3.38	3.40

Series D

Alloy	D-1	D-2	D-3
set %C	0.05	0.14	0.26
set %Si	1.0		
measured %C	0.051	0.145	0.259
measured %Si	1.07	1.04	1.00

Series E

Alloy	E-1	E-2	E-3
set %C	0.03	0.11	0.19
set %Si	1.0		
set %Mn	2.0		
measured %C	0.029	0.107	0.193
measured %Si	1.040	0.927	1.000
measured %Mn	2.10	1.89	1.95